

Automatic Breast Lesion Examination of DCE-MRI Data Based on Fourier Analysis

DIPLOMARBEIT

zur Erlangung des akademischen Grades

Diplom-Ingenieur

im Rahmen des Studiums

Visual Computing

eingereicht von

Christian Hirsch

Matrikelnummer 0825187

an der Fakultät für Informatik
der Technischen Universität Wien

Betreuung: Ao.Univ.-Prof. Dipl.-Ing. Dr.techn. Eduard Gröller
Mitwirkung: Univ.Ass. Dipl.-Ing. Dr.techn. Gabriel Mistelbauer

Wien, 3. September 2015

Christian Hirsch

Eduard Gröller

Automatic Breast Lesion Examination of DCE-MRI Data Based on Fourier Analysis

DIPLOMA THESIS

submitted in partial fulfillment of the requirements for the degree of

Diplom-Ingenieur

in

Visual Computing

by

Christian Hirsch

Registration Number 0825187

to the Faculty of Informatics
at the TU Wien

Advisor: Ao.Univ.-Prof. Dipl.-Ing. Dr.techn. Eduard Gröller

Assistance: Univ.Ass. Dipl.-Ing. Dr.techn. Gabriel Mistelbauer

Vienna, 3rd September, 2015

Christian Hirsch

Eduard Gröller

Erklärung zur Verfassung der Arbeit

Christian Hirsch
Theresiengasse 34/18, 1180 Wien, Austria

Hiermit erkläre ich, dass ich diese Arbeit selbständig verfasst habe, dass ich die verwendeten Quellen und Hilfsmittel vollständig angegeben habe und dass ich die Stellen der Arbeit – einschließlich Tabellen, Karten und Abbildungen –, die anderen Werken oder dem Internet im Wortlaut oder dem Sinn nach entnommen sind, auf jeden Fall unter Angabe der Quelle als Entlehnung kenntlich gemacht habe.

Wien, 3. September 2015

Christian Hirsch

Acknowledgements

First of all, I would like to thank Gabriel Mistelbauer for his superior support during my thesis. He took on the job of supervising me, when I came back from my stay abroad having some code, a weak idea but no plan of how to continue or even finish this thesis. Thank you for all the discussions, ideas, inputs, motivation and proof reading which finally led me to this finished diploma thesis!

A big thank you to Katja Pinker-Domenig and Pascal Baltzer from the Medical University of Vienna for their professional assistance, providing data sets and literature and answering all sorts of medical and breast cancer related questions.

Special thanks to the Visualization group at the Vienna University of Technology for providing a temporary workspace at their institute and letting me be a part of the group. It was an interesting and fun time and I learned a lot during that time. Best of all I would like to thank Meister Eduard Gröller for his input and support during this thesis and proof reading it.

Furthermore, I would like to thank the Marshallplan Foundation, Kwan-Liu Ma and Meister Eduard Gröller who made it possible for me to stay abroad at the Visualization and Interface Design Innovation Lab at the University of California, Davis, USA, where this thesis started. I learned a lot during my stay in California which I really appreciate. Although the goal of this thesis changed when I came back to Austria, the direction stayed the same.

Last but not least, I would like to thank my family, and best of all my parents, for their (financial) support during my study. A special thank you to all my friends, especially to my girlfriend, Kerstin, for your support and keeping me motivated throughout my study.

Kurzfassung

Brustkrebs ist in modernen Ländern die zweithäufigste Krebs-Todesursache. In weniger entwickelten Ländern ist es mit einer Sterblichkeitsrate von 25% sogar die Häufigste. Statistiken zeigen, dass der Schlüssel zur Bekämpfung der Brustkrebs Sterblichkeitsrate eine frühzeitige Erkennung ist. Neben Röntgen-Mammographie und dem Brustultraschall hat sich die dynamische Kontrastmittel-verstärkte Magnetresonanztomographie (KM-MRT) als zusätzliche bildgebende Methode zur Brustkrebsdiagnostik etabliert. Die MRT der Brust weist die höchste Sensitivität im Vergleich zu allen anderen bildgebenden Modalitäten in der Brustkrebsdetektion auf. Bisher wird die MRT der Brust von dem befunden Radiologen ausgewertet, Systeme für eine automatisierte Analyse der KM-MRT sind jedoch selten. Diese Arbeit präsentiert eine Methode zur automatischen Analyse von Brustkrebstumoren, wobei eine manuelle Segmentation der Läsion nicht notwendig ist. Es ist jedoch notwendig, die Läsion durch das Setzen einer Region-of-Interest (ROI) zu definieren. Nach der Definition der ROI wird diese in den Fourierbereich transformiert. Basierend auf dem Betrag des entstandenen Fouriervolumens werden Trägheitstensoren berechnet. Basierend auf diesen Informationen wird das Göttinger Punkteschema, ein punktebasierendes Schema zur Beschreibung von Brustlesionen ist, berechnet und in neuen visuellen Plots dargestellt, welche anschließend durch Radiologen evaluiert wurden. Das Göttinger Punkteschema basiert auf den folgenden Merkmalen: Form, Begrenzung, Kontrastmittelverteilung, initialer Kontrastmittelanstieg sowie der Kontrastmittelverlauf nach dem initialen Anstieg. Basierend auf einer Datenbank von 22 Läsionen bestehend aus histologisch verifizierten 14 malignen und 8 benignen Brusttumoren, wurde die vorgestellte Methode getestet. Die Ergebnisse wurden mit der Beurteilung einer erfahrenen Brustradiologin als Referenzklassifizierung verglichen. Die automatische Berechnung der Form lieferte eine Genauigkeit von 0.773, die Begrenzung 0.818 und die Kontrastmittelverteilung 0.886 verglichen mit den Werten der Radiologin. Eine Klassifizierung liefert eine Genauigkeit von 0.682 mit allen Werten des Göttinger Punkteschema, wenn hingegen nur die Form, Begrenzung und Kontrastmittelverteilung verwendet werden, wird eine Genauigkeit von 0.772 erzielt. Die Evaluierung der Plots zur Darstellung des Göttinger Punkteschemas durch Radiologen zeigt eine allgemeine Annahme der Darstellung einzelner Läsionen, jedoch eine Ablehnung der Plots in denen mehrere Läsionen dargestellt werden.

Abstract

Breast cancer is the second most common cancer death among women in developed countries. In less developed countries it has a mortality rate of about 25% rendering it the most common cancer death. It has been demonstrated that an early breast cancer diagnosis significantly reduces the mortality. In addition to mammography and breast ultrasound, Dynamic Contrast-Enhanced Magnetic Resonance Imaging (DCE-MRI) is the modality with the highest sensitivity for breast cancer detection. However, systems for automatic lesion analysis are scarce. This thesis proposes a method for lesion evaluation without the necessity of tumor segmentation. The observer has to define a Region Of Interest (ROI) covering the lesion in question and the proposed system performs an automated lesion inspection by computing its Fourier transform. Using the Fourier transformed volume we compute the inertia tensor of its magnitude. Based on the gathered information, the Göttinger score, which is a common breast cancer analysis scheme, is computed and the features are presented in newly create plots. These plots are evaluated with a survey where radiologists participated. The Göttinger score assigns a numeric value for the following features: shape, boundary, Internal Enhancement Characteristics (IEC), Initial Signal Increase (ISI) and Post Initial Signal (PIS). We tested our method on 22 breast tumors (14 malignant and 8 benign ones). Subsequently, we compared our results to the classification of an experienced radiologist. The automatic boundary classification has an accuracy of 0.818, the shape 0.773 and the IEC 0.886 compared to the radiologist's results. An evaluation of the accuracy of the benign vs. malignant classification shows that the method has an accuracy of 0.682 for all the Göttinger score features and 0.772 using only the shape, boundary and IEC. The evaluation of the plot shows that radiologist like the visual representation of the Göttinger score for single lesions, they, however, refuse the plots where multiple lesions are presented in one visual representation.

Contents

Kurzfassung	ix
Abstract	xi
Contents	xiii
List of Figures	xv
List of Tables	xix
1 Introduction	1
1.1 Medical Background on Breast Cancer	1
1.2 Problem Definition	9
1.3 Contribution	9
2 Related Work	11
2.1 Visualization	11
2.2 Information Visualization	23
2.3 Medical Background	26
2.4 Libraries	38
3 Methodology	41
3.1 Feature Computation	43
3.2 Feature Visualization	56
3.3 Software Prototype	61
4 Results and Discussion	65
4.1 Feature Computation Evaluation	67
4.2 Visualization Evaluation	70
5 Conclusion and Future Work	75
5.1 Conclusion	75
5.2 Future Work	76
A Results	77

xiii

B Malignancy Area Plot Survey	101
B.1 Linear and Cubic Malignancy Area Plots	102
B.2 Sunburst Malignancy Area Plot	103
B.3 Speed Test	103
B.4 Style Test	109
B.5 Questions	118
Bibliography	121

List of Figures

1.1	Full-field digital mammography example.	3
1.2	MRI scanner with breast coil.	5
2.1	Visualization pipeline overview.	12
2.2	Fourier transformed slice.	16
2.3	Line, plane and sphere volumes with their Fourier transforms.	18
2.4	Example of a TF to specify color in volume rendering.	20
2.5	Overview how raycasting works.	21
2.6	Steps for based GPU raycasting.	24
2.7	Information visualization examples.	25
2.8	3TP method by Degani et al.	28
2.9	Benign lesion example by Renz et al. [54].	36
2.10	Malignant lesion example by Renz et al. [54].	37
3.1	Workflow of our automatic breast lesion investigation.	44
3.2	DCE-MRI scan of a breast with a defined ROI.	46
3.3	Shape classification of a circle.	50
3.4	Shape classification of a star-shaped object.	51
3.5	Shape classification of an irregular-shaped object.	52
3.6	Phantom data sets showing the different IECs.	55
3.7	Example of linear and cubic Malignancy Area Plot (MAP).	57
3.8	Example sunburst MAP.	59
3.9	Sunburst Malignancy Area Plot (MAP) containing multiple data sets.	60
3.10	Screenshot of the Breast DCE-MRI Analyzer.	62
4.1	Performance of the feature computation.	70
4.2	Pie chart of the results of the style test.	72
A.1	Location, MIP, slice and resulting MAPs of the lesion 01.1.	78
A.2	Location, MIP, slice and resulting MAPs of the lesion 02.1.	79
A.3	Location, MIP, slice and resulting MAPs of the lesion 03.1.	80
A.4	Location, MIP, slice and resulting MAPs of the lesion 03.2.	81
A.5	Location, MIP, slice and resulting MAPs of the lesion 03.3.	82
A.6	Location, MIP, slice and resulting MAPs of the lesion 04.1.	83

A.7	Location, MIP, slice and resulting MAPs of the lesion 05.1.	84
A.8	Location, MIP, slice and resulting MAPs of the lesion 05.2.	85
A.9	Location, MIP, slice and resulting MAPs of the lesion 05.3.	86
A.10	Location, MIP, slice and resulting MAPs of the lesion 05.4.	87
A.11	Location, MIP, slice and resulting MAPs of the lesion 06.1.	88
A.12	Location, MIP, slice and resulting MAPs of the lesion 07.1.	89
A.13	Location, MIP, slice and resulting MAPs of the lesion 08.1.	90
A.14	Location, MIP, slice and resulting MAPs of the lesion 09.1.	91
A.15	Location, MIP, slice and resulting MAPs of the lesion 10.1.	92
A.16	Location, MIP, slice and resulting MAPs of the lesion 10.2.	93
A.17	Location, MIP, slice and resulting MAPs of the lesion 10.3.	94
A.18	Location, MIP, slice and resulting MAPs of the lesion 10.4.	95
A.19	Location, MIP, slice and resulting MAPs of the lesion 11.1.	96
A.20	Location, MIP, slice and resulting MAPs of the lesion 11.2.	97
A.21	Location, MIP, slice and resulting MAPs of the lesion 12.1.	98
A.22	Location, MIP, slice and resulting MAPs of the lesion 12.2.	99
B.1	Speed Test 01.	104
B.2	Speed Test 02.	104
B.3	Speed Test 03.	104
B.4	Speed Test 04.	104
B.5	Speed Test 05.	105
B.6	Speed Test 06.	105
B.7	Speed Test 07.	105
B.8	Speed Test 08.	105
B.9	Speed Test 09.	106
B.10	Speed Test 10.	106
B.11	Speed Test 11.	106
B.12	Speed Test 12.	106
B.13	Speed Test 13.	107
B.14	Speed Test 14.	107
B.15	Speed Test 15.	107
B.16	Speed Test 16.	107
B.17	Speed Test 17.	108
B.18	Speed Test 18.	108
B.19	Speed Test 19.	108
B.20	Speed Test 20.	108
B.21	Style Test 01.	110
B.22	Style Test 02.	111
B.23	Style Test 03.	112
B.24	Style Test 04.	113
B.25	Style Test 05.	114
B.26	Style Test 06.	115

B.27 Style Test 07. 116
B.28 Style Test 08. 117

List of Tables

1.1	The Göttinger score.	7
1.2	BI-RADS [®] categories.	8
4.1	Results of the manual and the automatic classifications.	66
4.2	Computed values for the morphologic feature classification.	68
4.3	Results of the speed test of our various Göttinger score representations.	71

List of Abbreviations

1D one-dimensional

2D two-dimensional

3D three-dimensional

3TP Three Time Points

ACR American College of Radiology

ANN Artificial Neural Network

AUC Area Under the Curve

BI-RADS® Breast Imaging Reporting and Data System

CAD Computer-Assisted Diagnosis

CT Computed Tomography

DCE-MRI Dynamic Contrast-Enhanced Magnetic Resonance Imaging

DFT Discrete Fourier Transform

IDFT Inverse Discrete Fourier Transform (DFT)

DICOM Digital Imaging and Communications in Medicine

DVR Direct Volume Rendering

FCM False Color Map

FFT Fast Fourier Transform

GLCM Gray Level Co-occurrence Matrix

GPGPU General Purpose Graphics Processing Unit (GPU)

GPL GNU General Public License

GPU Graphics Processing Unit

IARC International Agency for Research on Cancer

IDC Invasive Ductal Carcinoma

IEC Internal Enhancement Characteristics

ILC Invasive Lobular Carcinoma

ISI Initial Signal Increase
ITK Insight Segmentation and Registration Toolkit [1]
IT Information Technology
LSMD Least Squares Minimum Distance
MAP Malignancy Area Plot
MDI Morpho-Dynamic-Index
MIDA Maximum Intensity Difference Accumulation
MIP Maximum Intensity Projection
MITK Medical Imaging Toolkit [2]
MR Magnetic Resonance
MRI Magnetic Resonance Imaging
NCCN National Comprehensive Cancer Network
NEMA National Electrical Manufacturers Association
NRL Normalized Radial Length
OCR Optical Character Recognition
PBT Probabilistic Boosting Tree
PIS Post Initial Signal
REC Relative Enhancement Curve
ROC Receiver Operating Characteristics
ROI Region Of Interest
SER Signal Enhancement Ratio
MAP Malignancy Area Plot
SVM Support Vector Machine
TF Transfer Function
UI User Interface
VTK Visualization Toolkit [4]

Introduction

According to the International Agency for Research on Cancer (IARC) the number of newly diagnosed breast cancers worldwide in 2012 was 1.671 million among females, whereas the overall number of all cancers diagnosed among women in the same year was 6.658 million. Breast cancer accounts for about 25% of the cancers in women rendering it the most common one. With 522,000 deaths in 2012, breast cancer is the fifth most frequent cause of overall cancer death (including men). Among women it is the most frequent cause of cancer death in less developed countries. In developed regions it is the second most frequent cancer death besides lung cancer [21].

Randomized trials published in the IARC Handbooks of Cancer Prevention showed that inviting women aged 50–69 to screening using mammography decreases the mortality by 25%. It has been demonstrated in numerous studies that early diagnosis of breast cancer reduces mortality rate of breast cancer. To date, diagnosis of clinically asymptomatic breast cancer is achieved by imaging, which comprises digital mammography, breast ultrasound and magnetic resonance imaging. Digital image data enables the use of computers for automatic or semi-automatic diagnosis.

1.1 Medical Background on Breast Cancer

Tumors are atypical changes in an organ, which can be either benign or malignant. Malignant tumors, which are also called cancer or carcinoma, consist of (malignant) cells which have lost the ability of contact inhibition. Contact inhibition causes cells to lay paralyzed side-by-side to other cells of different organs when they contact each other. When cells lose this ability they are able to spread into organs without taking care of other structures. Malignant cells are caused by mutations during cell divisions. About eight to ten mutations are necessary until cells can become malignant [22]. Benign changes in the breast can be benign tumors which still have the ability of contact inhibition. They are not growing infiltratively, they displace other structures. Benign changes in the breast

which are not tumors can be caused by external forces, while benign tumors are never caused by external forces.

1.1.1 Types of Breast Cancer

Examples of benign lesions found in breasts:

- **Cysts:** Basically dilated milk ducts filled with fluid.
- **Fibroadenomas:** Benign breast tumor degeneration.
- **Mastitis:** An inflammation of the breast which might mimic malignancy. Standard of care is antibiotic treatment and follow-up to rule out malignancy such as inflammatory breast cancer.
- **Hematomas:** Benign findings in the breast caused by trauma.
- **Necrosis:** Reaction of fatty tissue caused by traumas. This often occurs after an operation.

Malignant tumors are classified into *Intraductal-* and *Invasive Carcinomas*. The intraductal carcinomas are local diseases, which have not infiltrated the basal membrane and are therefore still confined to the milk duct. Invasive carcinomas have penetrated the basal membrane and spread into the surrounding tissue, i.e., stroma, vasculature and lymph vessels and thus have a high risk of spreading to regional lymph nodes or to distant organs, e.g., the liver, lung or bones. Invasive carcinomas comprise [22]:

- **Invasive Ductal Carcinoma (IDC):** About 80% of invasive carcinomas are IDC.
- **Invasive Lobular Carcinoma (ILC):** With an occurrence of 10–15 % the ILC is the second most common invasive carcinoma.
- Other less common invasive carcinomas are: **Medullary Carcinoma, Mucinous Carcinoma, Pappillary Carcinoma, Tubular Carcinoma** and **Inflammatory Carcinoma**.

In addition to benign and malignant tumors, there are also *borderline* tumors. Such tumors are not malignant yet, but have the potential for transformation. Examples of borderline tumors are *Papillomas, Radial Scars, Atypical Ductal Hyperplasia* and *Lobular Neoplasia*.

1.1.2 Diagnosis

Breast cancer can be diagnosed in several ways. Clinically apparent breast cancers can be diagnosed by visual inspection as well as palpation. Their advantages are that women can do it on their own. The visual inspection is done as following: A woman needs to raise one arm in the air while the other one is placed on the hip. Then the breast is inspected with focus on the following [22]:

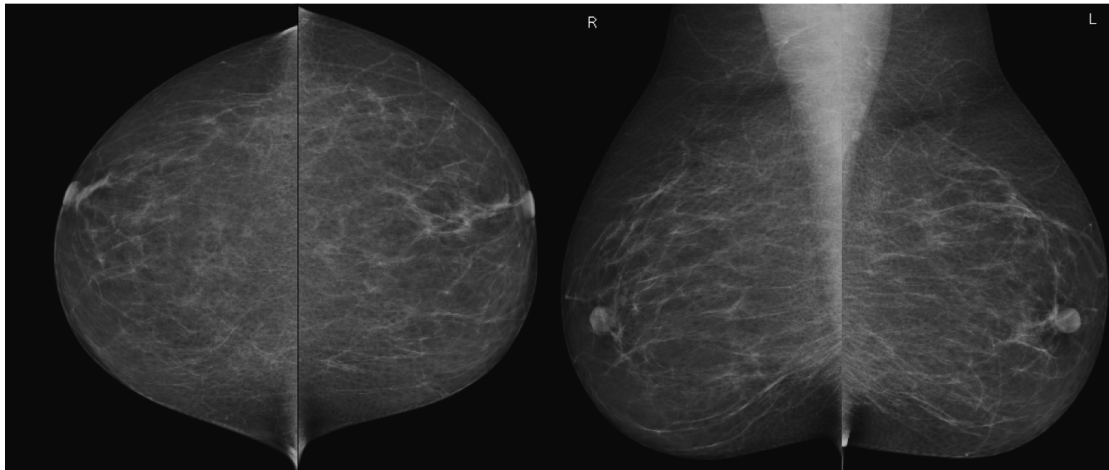


Figure 1.1: Example of a full-field digital mammography (cranio-caudal and medio-lateral projections). Courtesy of Katja Pinker-Domenig.

- Breast size and symmetry
- Contour
- Skin changes
- Nipples

In the next step the visual inspection is done with the other hand raised in the air and placing the second hand on the hip. If women realize changes or abnormalities in the mentioned factors it is recommended to consult a physician for assessment.

Palpation allows a woman to detect breast cancer, because neoplastic changes are different to the touch than normal or benign changes [22]. Beside palpation and visual inspection there are also image-based diagnosis methods, which comprise mammography, breast ultrasound and Magnetic Resonance Imaging (MRI).

Mammography

Mammography is an imaging method that uses X-rays. The basics of X-ray imaging are X-ray beams which pass through an object, i.e. the breast. Depending on the molecules in the object the X-rays are scattered, absorbed, or they just pass through them. The amount of X-ray radiation that passes through an object is measured and provides information about the object's composition [52]. For mammography special low-energy radiation is needed to achieve the required high tissue contrast [35]. The breast is placed onto a detector and compressed with a compression paddle. X-Rays are emitted by an X-ray tube to pass through the breast onto an analogue film or a digital detector. Figure 1.1 gives an example of a mammography unit.

Due to its cost efficiency, mammography is the most important imaging method for early breast cancer diagnosis. However, due to the varying nature of human breasts,

which depends on their content of fatty tissue, the use of mammography is limited in dense breasts. In breasts with a lot of fatty structures, it is easy to find lesions, while it is harder to find them in breasts with less fatty tissue.

Breast Ultrasound

In contrast to mammography, ultrasound of the breast uses an acoustic signal to produce images of the breast. Sound waves at very high frequencies are produced and transmitted into the patient's breast. The sound waves penetrate human tissue and are partially reflected if they hit an interface between two tissue types. The reflecting waves (echoes) are collected by a receiver, which produces a signal that is used to create an image [52]. A hand held device contains the ultrasound transmitter as well as the receiver. As a matter of user interaction and usability, there is no standardized method of how to use it. Therefore, the quality of the mammosonography examination heavily depends on the experience of a physician. Nevertheless, it is the second-most important imaging technique for breast cancer imaging [22]. A very important aspect is the absence of any radiation. Hence, this acquisition technique is completely harmless and can also be done in a short period of time [32].

Magnetic Resonance Imaging (MRI)

The physical basics of MRI is the signal emitted from the nuclei of hydrogen atoms. A hydrogen atom consists of a negatively charged electron and a positively charged proton. The proton is of interest as it is spinning, which means that it is rotating about its axis like a spinning top. As a rotating mass with an electrical charge, the proton also has a magnetic momentum (B). This means that it behaves like a magnet and has the following properties: It is affected by external magnetic forces, and it induces a voltage when it is moved. If an external magnetic field is applied to a spinning proton, the proton aligns with this magnetic field (like, e.g. a compass). But it does not only align, it also undergoes precession. Compared to a spinning top, the precession of a spinning proton is the wobbling of a spinning top if it is exposed to an external force. The frequency of the precession is proportional to the applied external magnetic field and it is called Larmor- or precession frequency. Spinning protons, that are exposed to an external magnetic field, get excited by applying an electro magnetic wave with the precession frequency using a radio transmitter. Excited spinning protons have a state with more energy compared to protons in an non excited state. In such an excited state, the protons move from the alignment with the magnetic field, lets call it M_z direction, 90 degrees into the M_{xy} direction and rotate about the z axis. This rotation induces an alternating voltage, with the precession frequency, which can be measured in receiver coils. This is the MR signal. When the radio transmitters are switched off, the protons align with the external magnetic field. This process is called relaxation. While the protons are relaxing the received MR signal is getting weaker. The time is measured how long it takes until the protons are in their initial state. Because various tissues in the body consist of different numbers of hydrogen atoms, the relaxation time is used to differentiate those tissues [63].



Figure 1.2: A MRI scanner and the coil used for breast imaging. Courtesy of Katja Pinker-Domenig.

Different electro magnetic pulses can be used to create images that reflect different tissue properties. Examples are T1, T2 or T2* relaxation times. More information about MRIs and relaxation is provided by Weishaupt et al. [63].

Using a contrast agent in combination with a special pulse can result in a behavior that extracts tissue properties of special interest. Intravenously injected gadolinium chelate contrast agent is used to shorten the T1 relaxation time. This leads to a high signal in T1-weighted images and improved tissue differentiation [15]. In breast cancer diagnosis, contrast enhanced MRI is the most sensitive imaging modality for supplementing mammography [35]. It is also insensitive to breast density or composition [36].

Taking several images over time with MRI using a contrast agent is called Dynamic Contrast-Enhanced Magnetic Resonance Imaging (DCE-MRI). Doing this, the flow of the contrast agent through the blood vessels of the breast can be recorded. This flow over time is also known as the kinetic information. It is acquired using the T1 relaxation time and it is the most important information in breast MRI analysis. Detailed information about using MRI in breast cancer diagnosis can be found in the literature [15, 22, 35, 36].

Figure 1.2 shows a MRI scanner and a dedicated breast coil. The patient lies on the coil in the prone position and is then moved with the coil into the isocenter of the magnet for image acquisition.

1.1.3 Reporting

Depending on different features of breast lesions acquired by MRI, Fischer et al. [22, 23] presented a point-based method to describe detected lesions. The lower the sum of the points is, the higher is the chance that the lesion is benign. Thus, a higher sum corresponds to a higher chance of a malignant lesion being present. The different features (criteria) are: The shape of the lesion, the boundary, the internal enhancement characteristics. Furthermore the kinetic information of the Initial Signal Increase (ISI) and the Post Initial Signal (PIS) are used. The possible classifications of the features and the corresponding points are shown in Table 1.1. This point scheme is known as the Göttinger or Fischer score.

Another internationally well known and accepted scheme for breast cancer reporting is the Breast Imaging Reporting and Data System (BI-RADS[®]) of the American College of Radiology (ACR) [18]. It categorizes findings depending on the type and likelihood of cancer. The BI-RADS[®] scheme defines six categories of breast findings:

1. **Negative:** No abnormality.
2. **Benign:** A benign tumor or change was found.
3. **Probably benign:** A mass or non.mass enhancement (NME) was found which has a high likelihood of being benign (rate of malignancy < 3%).
4. **Suspicious:** A mass or NME was found which can either be benign or malignant and requires histopathological verification .
5. **Highly suggestive of malignancy:** A mass or NME was found which has a high likelihood of being malignant.

Table 1.1: The Göttinger score [22, 23]. Features, used for breast cancer diagnosis, can be categorized by the lesion’s analysis. Based on these findings points are assigned to the features. All numeric values are added to calculate the overall score which represent a lesion’s likelihood of malignancy. A high overall score corresponds with a high likelihood of malignancy.

Feature	Finding	Points
Shape	round, oval	0
	dendritic, irregular	1
Boundary	smooth	0
	blurred	1
Computer-Assisted Diagnosis (CAD)	homogeneous	0
	non-homogeneous	1
	rim-enhanced	2
Initial Signal Increase (ISI)	low (< 50%)	0
	medium (50 – 100%)	1
	high (> 100%)	2
Post Initial Signal (PIS)	continuous increase	0
	plateau	1
	washout	2
Overall score		0 – 8

6. **Known biopsy - proven malignancy:** A biopsy confirmed a malignant tumor.

The according management, as well as the likelihood of being malignant are shown in Table 1.2 which shows also an additional category for incomplete diagnosis. The ACR defines a BI-RADS[®] scheme for each type of imaging method, also one for MRI based breast imaging [59]. However, the BI-RADS[®] scheme does not define features found in a scan that are used for categorization. Fischer and Baum presented a way to link the Göttinger score to the BI-RADS[®] scheme [22], shown in the last column of Table 1.2.

1.1.4 Therapy

Depending on the type of the diagnosed lesion, the appropriate therapy varies. Benign lesions typically are not treated in anyway. However, it is suggested that patients diagnosed with a benign lesion should continue to go to routine examinations. Breast examinations are recommended for all women. Especially if women are older than 50 years and younger than 70 years, they should consult routine mammography examinations biennially.

Table 1.2: The BI-RADS[®] categories with the corresponding management and the likelihood of the cancer [18]. The last column shows the overall Göttinger score that corresponds to the various categories [22, 23].

Category	Management	Likelihood of Cancer	Göttinger Score
0: Incomplete - Need Additional Imaging Evaluation	Recall for additional imaging	N/A	N/A
1: Negative	Routine screening	Essentially 0% likelihood of malignancy	0, 1
2: Benign	Routine screening	Essentially 0% likelihood of malignancy	2
3: Probably Benign	Short-interval (6-month) follow-up or continued surveillance	$> 0\%$ but $\leq 2\%$ likelihood of malignancy	3
4: Suspicious	Tissue diagnosis	$> 2\%$ but $< 95\%$ likelihood of malignancy	4, 5
5: Highly Suggestive of Malignancy	Tissue diagnosis	$\geq 95\%$ likelihood of malignancy	6, 7, 8
6: Known Biopsy-Proven Malignancy	Surgical excision when clinically appropriate	N/A	N/A

If borderline lesions are found, it is recommended to remove them surgically as the possibility of the cells getting malignant is high. Afterwards regular examinations are recommended [22].

In the past years if a breast cancer was diagnosed usually a (radical) mastectomy was performed. With improvements in breast cancer therapy, nowadays if tumor stage permits breast-conserving, breast radiation and systematic therapy achieve the same patient outcomes than mastectomy. Systemic therapy can be either adjuvant or neoadjuvant and comprise endocrine therapy, cytotoxic chemotherapy, and the targeted therapy. The recommendation of a specific therapy depends on defined guidelines. The National Comprehensive Cancer Network (NCCN) [3] defines the guidelines used in the United States. These are based on the tumor size, the node status (positive/negative), ER/PR (progesterone receptor), HER2/neu, which is a gene that is often overexpressed at certain types of breast cancer, menopausal status (for hormonal therapy). The European guidelines are defined by the International Experts Consensus Panel (St. Gallen). These are based on the cancer risk category (low/medium/high), tumor size, histological grade, lymphatic vascular invasion, HER2/neu status, age and the nodal status. More information about breast cancer therapy is provided in the work of Chen [12].

1.2 Problem Definition

An important step towards analyzing a breast lesion, is its segmentation. Segmentations can be done manually, where the user does the segmentation, semi-automatically, where a user gives some initial information and the rest of the segmentation process is done by a computer program, or automatically, where no user input/interaction is needed. No matter which type of segmentation is used, there is always the problem of wrong segmentations. Such wrong segmentations may lead to wrongly computed features and furthermore to a misclassification. Methods that work on a data set where no segmentation is necessary can help to avoid this problem.

Another problem is the visualization of the computed features of a lesion. Most works and applications do provide textual information about a lesion's features. But they do not combine the information into a single visualization, even though this could give a quick estimate about the lesion at a glance. There is a lack of normalized visualizations across multiple patients, or multiple follow-up studies of a single patient which support a comparative visual analysis of breast cancer lesions.

1.3 Contribution

This work analyzes the use of Fourier transforms on DCE-MRI data to compute features used for a benign vs. malignant classification of breast lesions. Even though a correct segmentation should not be necessary, the user still needs to define the Region Of Interest (ROI) which includes the lesion of the breast.

Another aim of this work is to present and evaluate visualization methods which combine different resulting features into a single chart. This chart should enable a user to quickly identify the result of the classification. Furthermore, it should provide information why a certain classification was computed in a compact and expressive manner to allow the user a fast overview of specific features of a lesion.

Related Work

This chapter presents the reader the basics that are necessary to understand the method described in the following chapter. It is divided into three bigger parts: The first part contains information about visualization techniques that have been used and the technical background. Based on the volume rendering pipeline this technical information and the visualization methods are explained. The necessary medical background information is described in the following section. At first it presents features that are commonly used in breast cancer research. Further presented publications show visualization techniques used in breast cancer research. The medical background is rounded up by publications that evaluate features, the combination of different features and reporting schemes. The last section of this chapter lists libraries we used and their application. This chapter provides the foundations for our methodology and summarizes topics in computerized breast cancer research.

2.1 Visualization

According to the Oxford dictionary “to visualize” means “make (something) visible to the eye”. But the main task of visualization is not only to create pictures out of data. The main task is to understand the data. “The purpose of visualization is insight, not pictures”, Ben Shneiderman (1999)¹ [11]. There are three types of goals for visualization:

- **To Explore:** Nothing is known about the data.
- **To Analyze:** A hypothesis is given and visualization is used for its verification or falsification.
- **To Present:** Visualization is used for the communication of information.

¹Based on Hamming (1973): “The purpose of computation is insight, not numbers.”

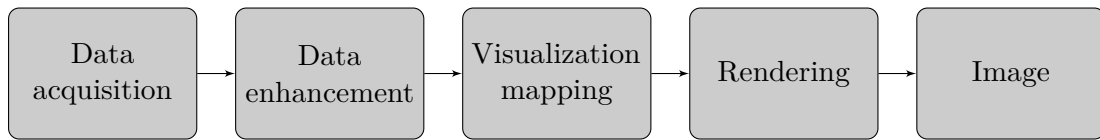


Figure 2.1: Overview of the visualization pipeline. These common steps are necessary to produce an image out of acquired data.

The visualization pipeline (Figure 2.1) represents the steps that are necessary to get an image out of data. We follow this pipeline to present the related work of this thesis. The pipeline consists of the following parts: Starting with the data acquisition, the acquired data is transferred to the data enhancement part for further processing. The processed data is used for the visualization mapping and, finally, it is processed by the rendering step. After the rendering step an image is produced.

2.1.1 Data Acquisition

The first step towards visualizing data is to get the data from a source. In medical visualization this data is often two-dimensional (2D) or three-dimensional (3D) and acquired using Computed Tomographies (CTs), MRIs, X-ray mammography etc. The data sets typically consist of intensity values. In the domain of 3D data sets, the smallest part, containing a single intensity value, is called a voxel (which means a volume element). When the first digital medical imaging modalities were introduced it was necessary to create a standard protocol for communication with and between imaging devices as well as for file formats to avoid that each manufacturer introduced his own communication and file formats. In 1983, the ACR and the National Electrical Manufacturers Association (NEMA) formed a joint committee to develop such a standard [48]: the ACR-NEMA standard. It specifies a hardware interface, a minimum set of software commands and a consistent set of data formats [48].

The Digital Imaging and Communications in Medicine (DICOM) standard is an improved version of the ACR-NEMA standard. It fits to the upcoming network technology and made other major enhancements over the ACR-NEMA standard, such as [48]:

- The applicability to a network environment (the ACR-NEMA standard was only applicable to point-to-point communication).
- The applicability to an off-line environment (the ACR-NEMA standard did not specify a file format or choice of physical media or logical filesystem).
- It specifies how devices, that conform to the standard, react to commands and how data is exchanged.
- It specifies levels of conformance.
- It is structured as a multi-part document.
- It introduces explicit information objects not only for images and graphics, but also for waveforms, reports, printings, etc.

- It specifies an established technique for uniquely identifying any information object.

Today DICOM is a widely used standard in medical imaging and facilities.

2.1.2 Data Enhancement

The acquired data often needs to be preprocessed to fit the needs for the visualization. This could be done by, e.g., segmenting parts of the volume, which are of interest. Another preprocessing step might also be data conversion for other computation tasks. In the following section some segmentation ideas and algorithms are described, as our work also needs a simple data enhancement for breast cancer analysis. Additionally, this section contains information about the Fourier transform, because we use it as a basis for our own classification algorithms.

Segmentation

A first step towards analyzing volume data is the definition of a sub-volume. Sub volumes that consist of the data to inspect are defined as the Region Of Interest (ROI). In the domain of volumes this might also be defined as a Volume Of Interest (VOI). The shape of a ROI is typically defined as a cuboid. The selection of a ROI is a necessary step as some algorithms operate locally and would lead to undesired results if they are applied to the entire volume. Another important fact is that the computation of features in a smaller volume takes less time than for the entire volume. If the ROI selection reduces the extent of the data to inspect in each direction by 10%, the amount of voxels is reduced by about 27% [52].

Segmentation is the task of decomposing image data into meaningful structures. These structures might be used for specific tasks. One aspect of segmentation is the identification of structures that belong to each other. This high-level task, which is part of the field of recognition, is usually well performed by humans. The other aspect of segmentation is delineation. This means to precisely define borders between different regions within the data. As this task is a very precise one, computers with specially designed algorithms can provide exact results. A challenge is to combine both tasks to create good segmentation results [52].

According to Preim and Botha [52], segmentation algorithms need to fulfill four essential requirements, especially in a medical scenario:

- **Robustness:** Algorithms need to work on a wide variety of cases.
- **Reproducibility:** The result should be the same, no matter how many times the algorithm has been applied on the same data.
- **Accuracy:** Algorithms need to produce an accurate result, which is a result that is expected by the user. Accuracy can be determined with validation studies.
- **Speed:** The results of an algorithm should be computed within an acceptable period of time, as methods or users that depend on the result cannot continue their work while they are waiting for the method to finish.

Segmentation methods can be categorized, as already mentioned, as manual, semi-automatic and automatic segmentation methods. Examples of manual segmentation are manual drawing, or the selection of parts of the image that belong together. However, this is a very time-, and therefore resource-consuming method. Semi-automatic segmentation approaches are threshold-based algorithms. These methods produce a binary output by manually defining a global or an upper and lower threshold. Often a connected component analysis is applied to the result of thresholded images. This method groups regions together where voxels (or pixels) are connected with a certain connection property. Region growing is a segmentation method where voxels are connected together that fulfill a certain quality criterion. This criterion might be given by defining thresholds (semi-automatically), or adapting a threshold by analyzing the already segmented data (automatically). Another automatic algorithm is watershed segmentation. This concept treats image data like a topological landscape. When it starts raining, the water is collected in the lowest regions, which are the segmented image parts. The more it rains, the more parts of the landscape become flooded, and watersheds disappear. In case of segmentation, this means that regions are merged. The general scope of this method was introduced by Digable and Lantuejoul in 1978 [17]. Beside these basic segmentation techniques, there are numerous more sophisticated ones like graph-based algorithms or model-based methods, which are not described here. The interested reader is referred to Preim and Botha [52] where all those techniques are described in more detail.

Fourier Transform

In mathematics a Fourier series is a composition of sine and cosine functions at different frequencies, which describes a signal. Most common signals can be specified by such a composition of sine and cosine functions with an infinite number of frequencies. The conversion of a signal from the spatial domain $f(\vec{x})$ into the frequency domain $\hat{f}(\vec{u})$ is called Fourier transform. $f(\vec{x})$ represents the signal's value at the (spatial) position \vec{x} . $\hat{f}(\vec{u})$ represents the signal's energy at frequency \vec{u} as complex numbers, which consist of a real and an imaginary part. This real and imaginary part can also be represented by their magnitude $|\hat{f}(\vec{u})|$ and phase $\arg(\hat{f}(\vec{u}))$, where the magnitude represents the amount of energy of the frequency \vec{u} in the signal and the phase represents the offset to the basic sinusoid at that frequency.

In practice, especially in digital signal processing, signals are finite. Even a Fourier series needs to be stored in a finite way. The Discrete Fourier Transform (DFT) is a discrete version of the Fourier transform in order to handle functions with discrete values. To compute the DFT of a discrete function with N samples, N^2 computations are necessary ($O(N^2)$) [20]. Cooley and Tukey presented a fast DFT algorithm, known as Cooley-Tukey Fast Fourier Transform (FFT), which is capable of computing a discrete Fourier transform in $O(N \log_2 N)$ operations by using a divide-and-conquer approach. The FFT algorithm by Cooley and Tukey was already known around 1805 by Carl Friedrich Gauß. However, Cooley and Tukey reinvented the technique and made it popular [13, 20, 26].

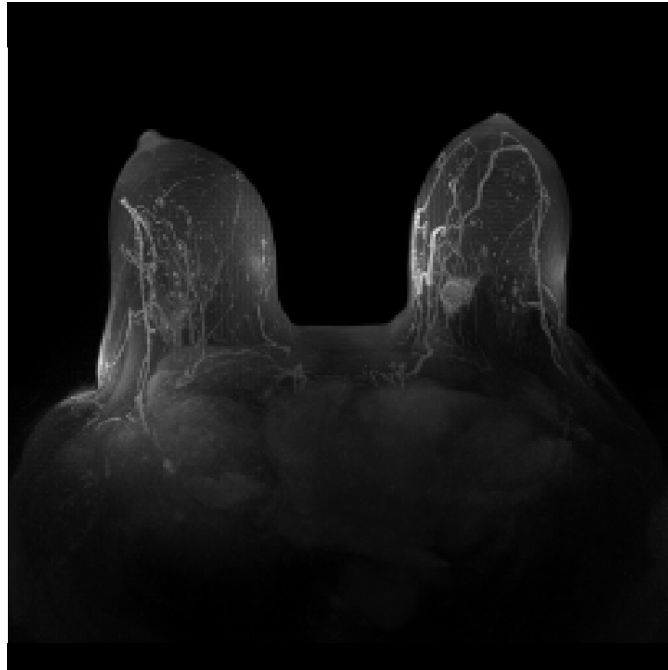
An example of a Fourier transformation is given in Figure 2.2. The Fourier transform of a breast MRI data set, presented in Figure 2.2a using a Maximum Intensity Projection (MIP), was performed and the resulting magnitude image is shown in Figure 2.2b and its phase image in Figure 2.2c. Lower frequencies are represented closer to the center of the Fourier transformed image and higher ones closer to the border.

The Fourier transform is widely used in acoustic signal and image processing, commonly applied on one-dimensional (1D) and 2D signals. It is also possible to use the Fourier transform for 3D (and higher) signals, e.g., for volumes or videos. One application of the Fourier transform is extracting local neighborhood information of spatial images in their frequency space. Jähne [37] denotes a local neighborhood that can be described by an orientation as simple neighborhood. This occurs when constant gray (pixel) values are aligned along a line. Such images are also called symmetric linear images. Analyzing a simple neighborhood is thus computing the orientation of the alignment of the constant pixel values. Bigün [9] shows that a symmetric linear image has a Fourier transform where the spectral energy is concentrated to a line through the origin, where the line represents the orientation of the simple neighborhood. The challenge is now to fit a straight line to the orientation of the spectral energy. As this problem is over-determined, the solution can be determined by fitting the line to the spectral energy points by minimizing the sum of the squared distances to these points as described by Bigün and by Jähne [9, 37]. In order to solve this problem, Bigün introduces the inertia tensor \mathbf{J} of the Fourier transform:

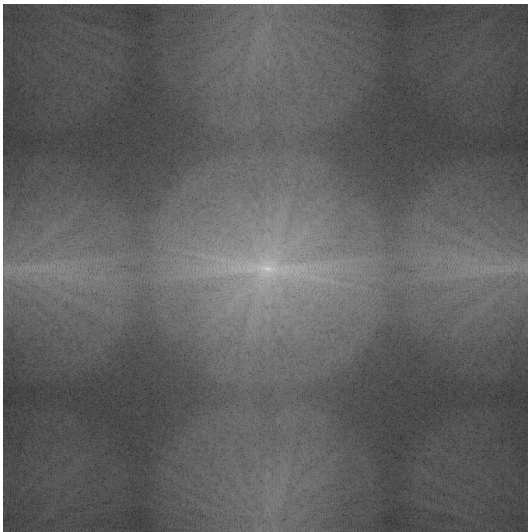
$$\mathbf{J} = \begin{pmatrix} J_{1,1} & J_{1,2} & \cdots & J_{1,n} \\ J_{2,1} & J_{2,2} & \cdots & J_{2,n} \\ \vdots & \vdots & \ddots & \vdots \\ J_{n,1} & J_{n,2} & \cdots & J_{n,n} \end{pmatrix} \quad (2.1)$$

This tensor is a diagonal matrix where n denotes the dimension of the data (e.g., 2 for images and 3 for volumes). The Eigenvalues $\lambda_1, \lambda_2, \dots, \lambda_n$ of \mathbf{J} are used to solve the minimization problem in order to determine the orientation. The Eigenvector belonging to the smallest Eigenvalue represents the orientation of the spatial image [9, 37].

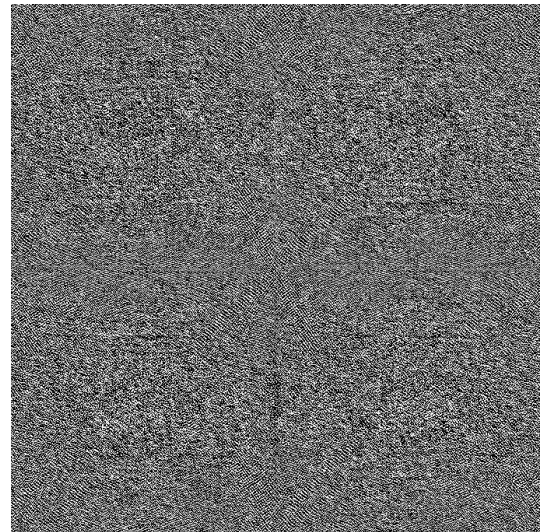
Wilson et al. [67] presented a multi resolution approach for the Fourier transform. The basics of this work is to divide an image or (acoustic) signal into smaller parts (e.g., sub-images). These smaller parts are then transformed into the Fourier (or frequency) space for computing local features for boundary curve segmentation. Bhalerao and Wilson [8] extended the approach of Wilson et al. [67] to three dimensions space in order to compute local features of vascular structures in volume data. The spectral energy of a Fourier transformed and Gaussian distributed spatial volume image is also Gaussian distributed [8]. Additionally, to the orientation of the spatial intensity distribution, it is also possible to estimate the spatial intensity distribution by using the spectral energy of the Fourier transform. Both of this features can be computed using the Eigenvalues and



(a) Spatial image



(b) Magnitude image



(c) Phase image

Figure 2.2: A Fourier transformation of the MIP of a breast MRI data set.

Eigenvectors of the inertia tensor \mathbf{J} [8]. Bhalerao and Wilson compute the 3D inertia tensor in the following way [8]:

$$J = \frac{1}{B^3} \sum_{\vec{u}} \vec{u} \vec{u}^T |\hat{f}(\vec{u})|^2, \quad (2.2)$$

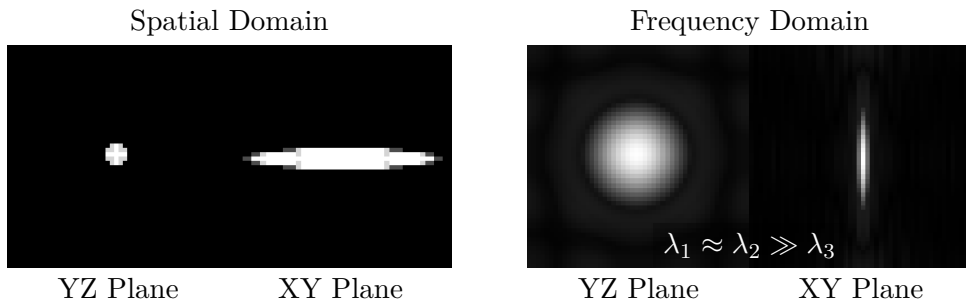
where B denotes the size of the volume and $\hat{f}(\vec{u})$ is the spectral energy at frequency \vec{u} . The Eigenvalues $\lambda_1 \geq \lambda_2 \geq \lambda_3$ can then be used to classify the local structure and the corresponding Eigenvectors $\vec{e}_1, \vec{e}_2, \vec{e}_3$ for estimating the local orientation. The basic local structures are shown in Figure 2.3 and are defined as:

- **Line:** The spatial volume intensities are distributed linear if $\lambda_1 \approx \lambda_2 \gg \lambda_3$ [8]. The orientation of the line is given by the Eigenvector \vec{e}_3 [9, 8, 37]. Figure 2.3a shows the spatial volume intensities of a line on the left side and the corresponding Fourier magnitude volume on the right side.
- **Plane:** The spatial volume intensities are distributed planar if $\lambda_1 \gg \lambda_2 \approx \lambda_3$ [8]. The orientation, the normal vector of the plane, is given by the Eigenvector \vec{e}_1 . Figure 2.3b shows the spatial volume intensities of a line on the left side and the corresponding Fourier magnitude volume on the right side.
- **Sphere:** The spatial volume intensities are distributed spherical, or isotropic, if $\lambda_1 \approx \lambda_2 \approx \lambda_3$. All three Eigenvectors can be used to describe the spatial extend [8]. Figure 2.3c shows the spatial volume intensities of a sphere on the left side and the corresponding Fourier magnitude volume on the right side.

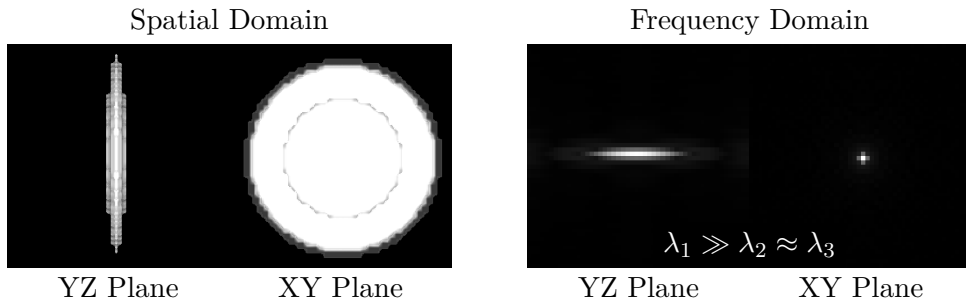
Using these approaches, Bhalerao and Wilson [8] analyzed a volumetric data set containing blood vessels at different scales. At each scale, the linearity, planar and spherical features are computed to estimate the spatial structure of the volume.

2.1.3 Visualization Mapping

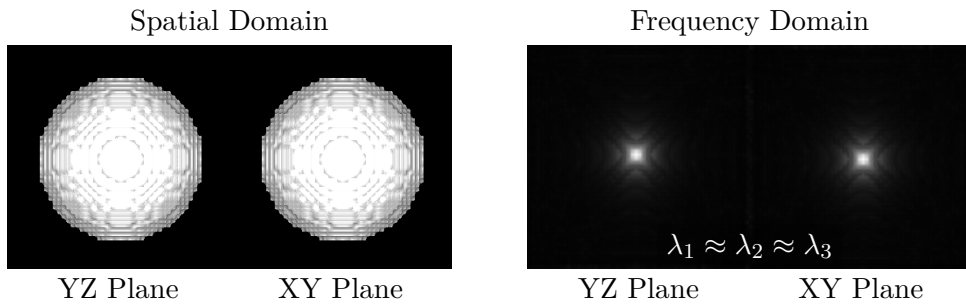
The visualization-mapping stage is the part in the visualization pipeline that transforms data into a renderable state. Depending on the rendering technique there are several methods how this can be achieved. One example is iso-surface rendering. This method uses an iso-surface value (which is typically a manually provided threshold value) and creates geometric data by analyzing the volume and creating a surface everywhere where the transition in intensity value from one voxel to its neighbor crosses the threshold. The most important method to create geometric data from an iso-surface value is the Marching Cubes algorithm by Lorensen and Cline [43]. The algorithm works locally and needs eight corners of a cube (eight voxels that span a cell) as input for the creation of a surface. Each corner specifies in a binary way if it is inside or outside of the surface. One of the major advantages of this algorithm is that the triangulation is based on a lookup table. For each possible configuration of the corners of the cube, a resulting surface is predefined which only needs to be looked up. The disadvantage of this locally operating algorithm is that the created surface may contain holes because of inconsistencies [43, 52].



(a) A 3D line data set rendered with MIP on the left side in the spatial domain and on the right side in the frequency domain with $\lambda_1 \approx \lambda_2 \gg \lambda_3$.



(b) A 3D plane data set rendered with MIP on the left side in the spatial domain and on the right side in the frequency domain with $\lambda_1 \gg \lambda_2 \approx \lambda_3$.



(c) A 3D sphere data set rendered with MIP on the left side in the spatial domain and on the right side in the frequency domain with $\lambda_1 \approx \lambda_2 \approx \lambda_3$.

Figure 2.3: The three basic types of volumes that are classified by Bhalerao and Wilson [8]: A line (a), a plane (b) and a sphere (c). For each of the volumes the Fourier transform was applied yielding the Fourier magnitude volume images to the right of the spatial image. The λ_i values are the Eigenvalues of the Fourier magnitude volume's inertia tensor \mathbf{J} .

The created geometric data can then be rendered with state-of-the-art geometry rendering techniques. Another way of visualization mapping is to apply additional information (like visual properties) to the values in the data sets. This is typically done using a Transfer Function (TF). A TF is a function which allows the user to assign a color and an opacity value to a single intensity value (e.g., white to bones, skin-color to skin, etc.). An example of a TF with the resulting rendering is shown in Figure 2.4. On the horizontal axis of the TF the intensity values are given and colors are specified. The vertical axis is used to specify an opacity for a certain intensity value. In this example a transparent reddish color is used for the lower intensity values (skin). A medium transparent yellow is used for medium-high intensity values (bones). An opaque white is used for the highest intensity values (teeth).

2.1.4 Rendering

Rendering is the part in the visualization pipeline which deals with methods used to create 2D images out of the acquired data. In case of 3D data this is called volume rendering or visualization. Basically, there are two types of algorithms to render volumetric data: Indirect Volume Rendering and Direct Volume Rendering (DVR) [28]. Indirect Volume Rendering techniques create surfaces (geometric data) out of volumetric data in the data enhancement part of the visualization pipeline. These surfaces are then used to render the images with state-of-the-art surface rendering techniques. DVR, however, does not need to create another data representation as it directly uses the volumetric data to produce images. Fuchs et al. [28] describe a binary voxel technique as third basic volume rendering method. This technique assigns a binary value to each voxel of a volume, depending on whether it needs to be drawn or not. Very simple drawing techniques were used because only single cubes needed to be drawn. Because of the improved and much faster hardware nowadays, this technique became obsolete.

Direct Volume Rendering (DVR)

As opposed to Indirect Volume Rendering, where render-able (geometric) data has to be created in a preprocessing step, DVR uses the volumetric data directly to produce pictures. Rendering algorithms for DVR can be classified as either object-order or image-order. Object-order algorithms compute how an object, which is typically a voxel in volume rendering, contributes to the pixels of the image. One method of how this can be done is drawing one slice after another, beginning with the slice that is farthest away from the user (back-to-front) [25]. Depending on the rotation of the volume, it is necessary to evaluate the correct slicing direction. The slices that face the viewing direction are chosen for the rendering of the volume. Another well known example of an object-order algorithm is splatting, which was first described by Westover [64]. This algorithm traverses all voxels of the volume, computes their screen space contribution (depending of the view of the user), shades the voxels and finally combines them in the image buffer.

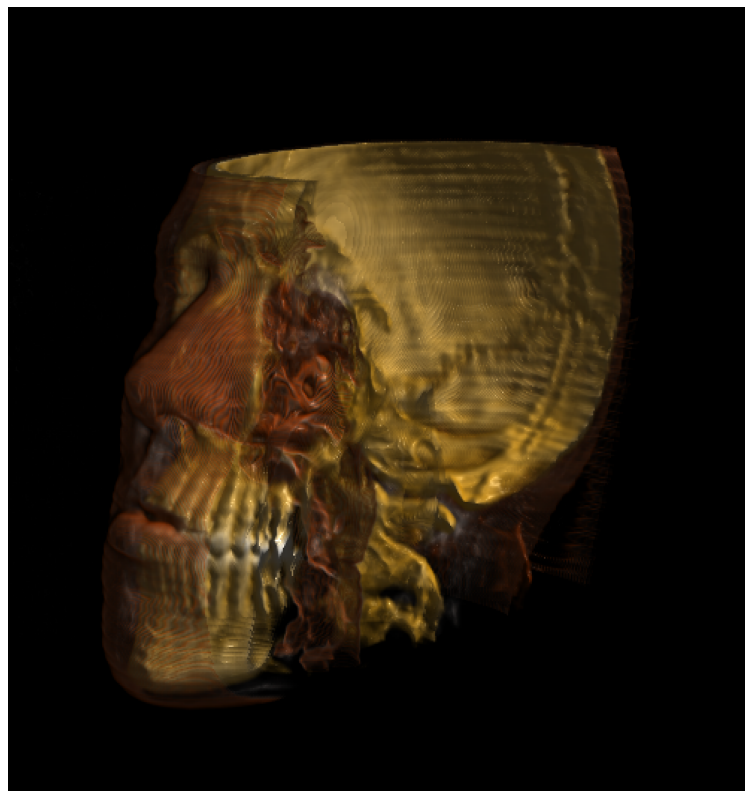
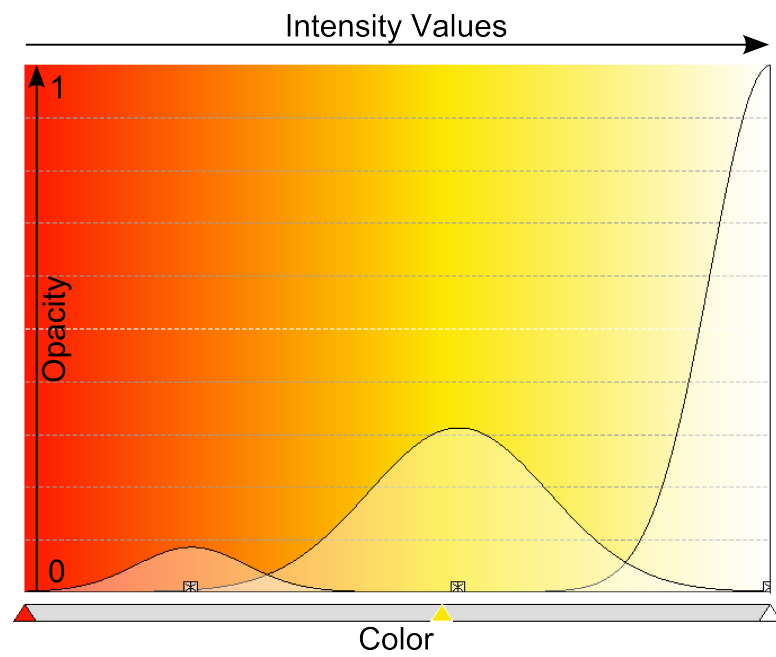


Figure 2.4: An example TF with the resulting rendering of a volumetric data set of a human head. The skin is rendered transparent reddish. Medium transparent yellow is assigned to the bones. For the teeth an opaque white was used.

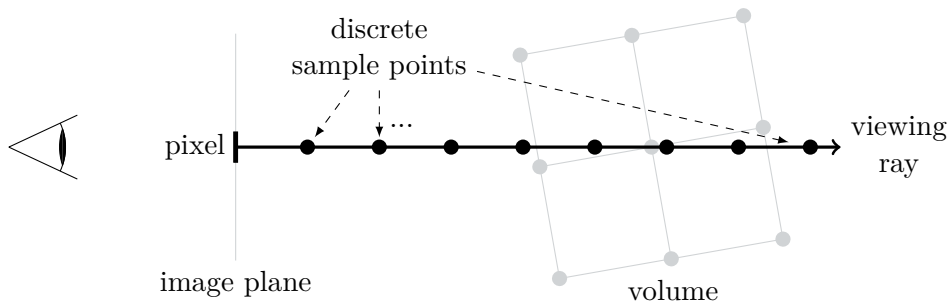


Figure 2.5: Ray casting. A viewing ray is shot from a pixel through the volume. The intensity values of the volume at the discrete sample points are evaluated and combined.

Image-order algorithms start their computation at an image location, a pixel. These types of algorithms compute how a pixel is influenced by the voxels. Ray casting is one important example of image-order algorithms. Beginning from an image pixel, a ray is cast through the volume (object). At discrete sample points along the ray, the volume has to be evaluated. Figure 2.5 shows the idea of ray casting. All the intensity values evaluated at the discrete sample points are combined and form the pixel. Because it is now possible that a sampled location is not directly on a voxel, it is necessary to interpolate the values of the surrounding voxels. The easiest way of interpolation is called nearest neighbor, where the value of the closest voxel is chosen. Tri-linear interpolation computes the influence of each of the surrounding voxels of the sample point according to their distance and combines them. Throughout this thesis, we use ray casting for DVR to visualize data sets.

Volume-Rendering Pipeline

The volume-rendering pipeline specifies in which steps individual operations (sampling, classification/illumination, compositing) are performed. Sampling is the part where an intensity value of a discrete location of the volume data set (a voxel) is accessed.

The classification or illumination part maps the intensity value of the volume to a color. The color represents a meaning or a special class which can be defined by a TF. Additionally, lighting can be applied by using an illumination model like the one presented by Phong [51]. Such models require information about surfaces. Volumes, however, do not contain surface information. To overcome this problem, Levoy [41] as well as Drebin et al. [19] presented methods that use gradient vectors for surface shading. A gradient vector is calculated using the intensity values of a voxel and its local neighborhood resulting in a vector that points towards the biggest change of the local intensity values. This gradient vector can be used to approximate a local surface and, thus, for shading a voxel with an illumination model.

The last step in the volume rendering pipeline is the compositing where the classified and illuminated color values along the ray are combined. This final step is the discrete and numerical approximation of the volume-rendering pipeline [52].

The order of the sampling and classification/illumination stage may change. In case of first sampling and then classifying/illuminating, the rendering pipeline is called post-classified. Whereas when the classification/illumination is done before the sampling, it is called a pre-classified volume-rendering pipeline [52].

Compositing

The volume rendering equation is the standard physical model for DVR. It is based on emissions and absorptions [44, 52]. Equation 2.3 shows the combination of the absorption and emission model, where I refers to the intensity value, s is a position along the ray S . s_0 is the position where the ray S enters the volume. Q models the light emission at a certain point, and $T(p)$ the transparency between the s_0 and p .

$$I(s) = I(s_0) \cdot T(s_0) + \int_{s_0}^s Q(p) \cdot T(p) dp \quad (2.3)$$

This equation is, however, analytically not solvable. Hence, the equation needs to be solved numerically. Equation 2.4 shows the numerical solution of the direct volume rendering equation [44, 52]. Δs is a fixed step size which scales the current sampling position k along ray S .

$$I(s) = I_0 \prod_{k=0}^{n-1} t_k + \sum_{k=0}^{n-1} Q(k \cdot \Delta s) \cdot \Delta s \prod_{j=k+1}^{n-1} t_j \quad (2.4)$$

This equation describes how the ray S is traversed with the initial intensity value of the first summand through the volume data set and accumulates at discrete locations k the contribution to the final intensity value I [52].

It is possible to adjust the compositing part of the rendering pipeline to get different visualization results. The method above describes the implementation of the direct volume rendering pipeline based on the absorption and emission model. An X-ray like image can be created by averaging the intensity values along the ray. The Maximum Intensity Projection (MIP) is a method where only the highest intensity value of a data set along the ray S is used for the image. This is useful for visualizing, e.g., enhanced parts in DCE-MRI. The problem of this compositing method is that the spatial relation is lost. To overcome this, Bruckner and Gröller [10] defined a method called Maximum Intensity Difference Accumulation (MIDA). Compositing is achieved by keeping track of each sample that defines a new maximum. The magnitude of the difference between a new maximum and the previous one is used to emphasize the contribution of the corresponding sample [10, 52].

DVR Implementation

Today a Graphics Processing Unit (GPU) is designed to do massive parallel computation. This property allows the user a fast generation of DVR images. As each ray, which is

traversed through the volume, is independent from all the others it is a perfect example of parallel computation. Another property of GPUs is that they can handle 3D textures. In case of volume rendering, they can store a whole volume in the memory and all the filtering and interpolation is already provided by the hardware. Krüger and Westermann [40] presented the well known method for GPU based volume rendering. This graphics-shader based method first renders to a texture a cuboid twice with coordinates (which are represented by colors) assigned to each corner depending on their position in space. In the first rendering pass it renders the front faces of this cuboid into a texture (see Figure 2.6a). The front faces of a cuboid are the faces which are seen by an observer. In the second rendering pass, the back faces, which are the faces that are hidden by the front faces and thus not visible to an observer, are drawn into another texture (see Figure 2.6b). These two textures are used in the fragment shader to calculate the position and direction of the ray to be traversed through the volume. Figure 2.6c shows the result of the ray directions (mapped to colors) computed using Figure 2.6a and Figure 2.6b. Within the fragment shader one of the mentioned compositing methods is applied to create a color value for each pixel for the final image. An example is shown in Figure 2.6d where a MIP of a breast lesion is rendered. Levoy already presented a method where he used the Pixel-Planes 5, which is a raster graphics engine incorporating custom memory (similar to today's GPUs), for boosting volume rendering by exploiting its parallelism in 1989 [42].

Beside this shader-based method, General Purpose GPU (GPGPU) programming, which uses the massive parallelism of GPUs for general (not necessarily graphics related) parallel programming, can also be employed to implement a volume ray caster.

2.2 Information Visualization

Information visualization is another field in visualization. Jock Mackinlay described it by “Information visualization is the use of computer-supported interactive visual representations of abstract data to amplify cognition” [11]. The aim is knowledge crystallization. Abstract information with different types of variables (ordinal, nominal, quantitative) needs to be graphically represented. The structure of the data that needs to be visualized can be classified by the use of space. Besides 1D, 2D and 3D data, information visualization also needs to be able to handle high-dimensional, n -dimensional (nD), data. But not only the graphical representation is vital. Information visualization systems need to provide excellent User Interface (UI) components [58]. The visual information seeking mantra by Shneiderman “overview first, zoom and filter, then details on demand” [58] is a useful starting point for designing advanced graphical UIs. Examples of (simple) information visualization techniques are graphs that plot data. Scatter plots are representations where data is visualized by a set of points in space (see Figure 2.7a). Scatter plots are often used to draw 2D as well as 3D data. Another information visualization method is the star plot (Figure 2.7b), where the coordinates are arranged like a star around a center. This plot is not limited by the number of dimensions of the data. A similar approach to the star plot are parallel coordinates. This method is also not

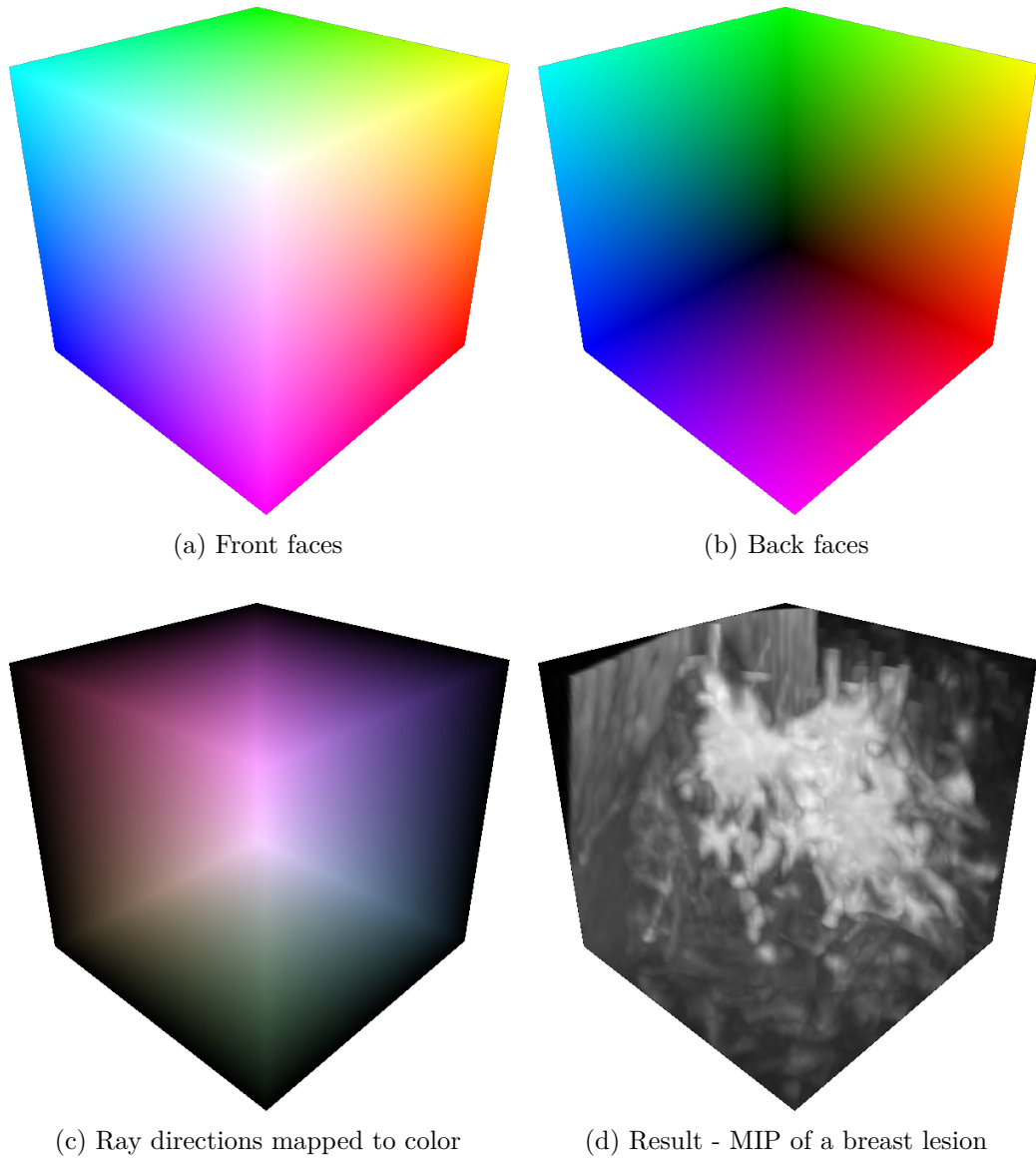


Figure 2.6: GPU-based approach to determine ray directions for DVR. First, the front (a) and back faces (b) are rendered into two separate textures. Then, the ray is computed using those two textures (c) which is then traversed through the volume to render the image (d).

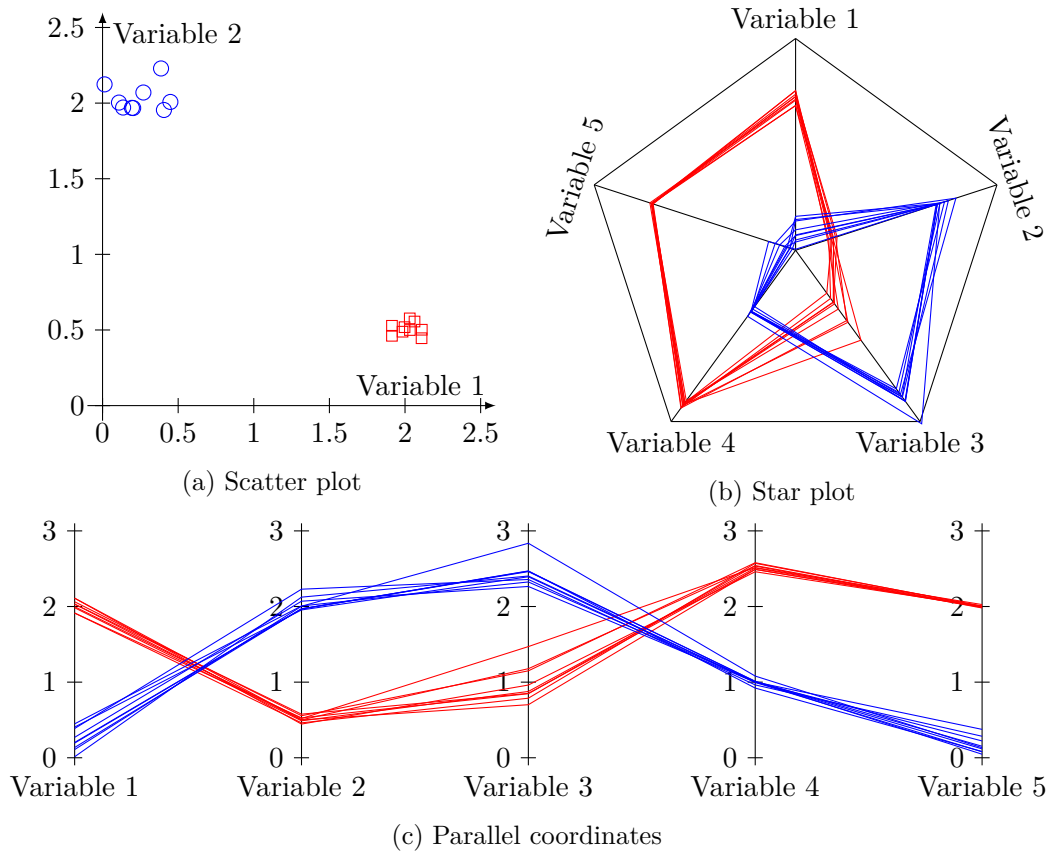


Figure 2.7: Examples of views which are often used in information visualization systems.

limited by the dimension of the data. As the name already says, the different coordinates are arranged parallel to each other like shown in Figure 2.7c. All the examples in Figure 2.7 show the same data (however in the scatter plot only two dimensions, Variable 1 and 2, are presented). 18 data sets, nine for each of two classes, with five numerical values each, were generated randomly. Typically more than one view is provided by an information visualization system. The different views are linked together. This means that a user can select (interesting) information in one view, and the other views are updated accordingly. An example would be that a user selects some points in a scatter plot (Figure 2.7a), and the parallel coordinate view and/or the star plot is updated reflecting the selected information. This reflection can either be achieved by showing only the selected data, or highlighting the selected data, while the remaining data is drawn with less visual importance in order to keep contextual information.

An evaluation to assess reproducibility and validity of graphs in the field of meta analysis was performed by Bax et al. [7]. In order to identify or rule out heterogeneity or publication bias, one major factor is the assessment of graphs. Heterogeneity is the variation among effect parameters across studies. Publication bias refers to a

systematic error in the meta analysis that occurs because not all of the evidence is properly represented. In order to do the evaluation the authors created simulated data and presented the data in different plots. Random simulated data was presented over a period of three weeks to experienced researchers in the field of meta analysis. These researches had to rate the heterogeneity and the publication bias from 0 (*none*) to 100 (*extensive*). The results of the study showed that different plots are not equally useful for the same application or data set. The author extends the expression “A picture is worth a thousand words” to “A picture may be worth more than a million numbers” for the meta analysis [7]. They also mention that the reproducibility and validity heavily depends on the type of graph and the construct it is meant to visualize. Thus, meta analysts should be selective in the graphs they choose for the exploration of their data [7].

2.3 Medical Background

In breast cancer research a lot of work has been conducted in analyzing the kinetic features, which represent the dynamic behavior of the contrast agent. Beside the kinetic features, morphologic features represent, e.g., the shape, margin or Internal Enhancement Characteristics (IEC) of a breast lesion. Some work has also been done in extracting and analyzing textural features. Textural features are used to represent a volume by its intensity values, especially the change in intensity values from one voxel to another one. Features used for breast cancer analysis are typically extracted from the T1-weighted MRI volumes which are acquired in combination with contrast agents.

Classification techniques are typically evaluated using the Receiver Operating Characteristics (ROC). The ROC plots the results of a (binary) classification based on its sensitivity and its specificity. The sensitivity, which is the true positive rate, represents the correctly classified malignant lesions, whereas the specificity, the true negative rate, represents the correctly classified benign lesions. Sensitivity and specificity are represented in the range 0.0 – 1.0. A sensitivity value of 1.0 represents a method that classifies all malignant lesions as malignant, while a sensitivity value of 0.0 represents a method that classifies all benign lesions as malignant. A specificity value of 1.0 represents a method that classifies all benign lesions as benign, while a specificity value of 0.0 represents a method that classifies all malignant lesions as benign. The Area Under the Curve (AUC) of the ROC is an overall statistical parameter to measure the classification rate based on the area of the ROC, where $0.0 \leq AUC \leq 1.0$. An AUC value of 1.0 represents methods that correctly classify all malignant lesions as malignant as well as all benign lesions as benign, while an AUC of 0.0 represents a method that classifies all malignant lesions as benign and vice versa.

Fourge et al. analyzed kinetic features of DCE-MRI and the correlation between contrast enhancement and tumor angiogenesis [27]. First, a ROI is defined and a threshold is used to define parts which belong to the lesion. Then “dixels” (dynamic pixels), which contain the enhancement intensity values of pixels over time, are analyzed by finding factors for a mathematical formula constituted by linear combinations. These factors (formulas) are then compared to the result of the histopathological biopsy. The

results show that an early enhancement in the images correlate with the number of vessels determined histologically [27].

Kelcz et al. [39] investigated enhancement patterns of DCE-MRI over time. They present a quantitative approach for fitting the dynamic intensity values to discriminate benign from malignant tumors. The general saturation equation [39, 47]

$$I(t) = I_0 + I_\alpha \cdot \frac{1}{(T_{1/2}/t)^M + 1} \quad (2.5)$$

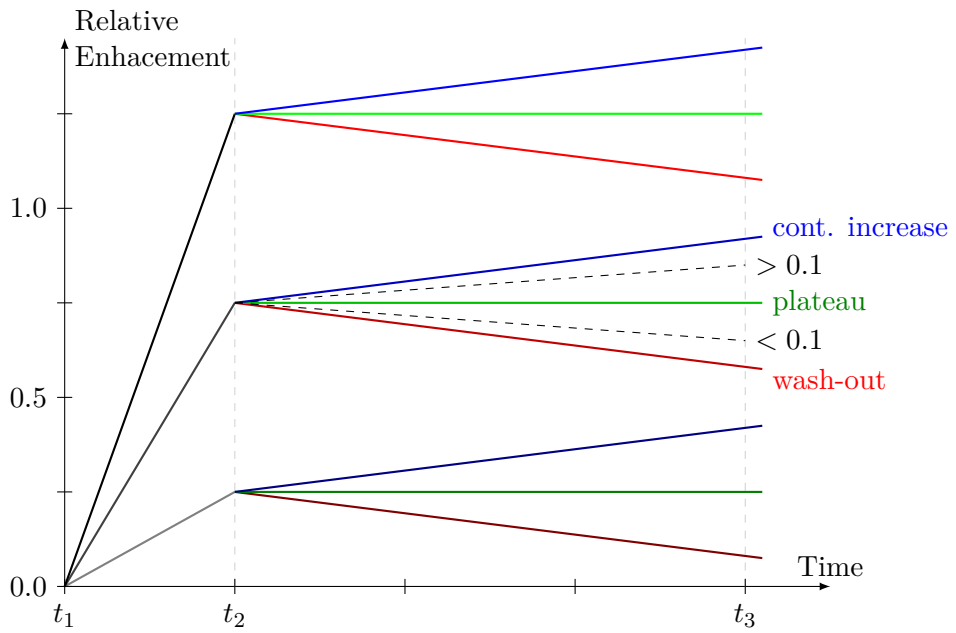
builds the basis for the study. $I(t)$ is the intensity value at time t . I_0 is the intensity value before contrast agent injection. I_α is the asymptotic increase of I after contrast agent injection. $T_{1/2}$ is the time at which I is midway between I_0 and I_α . M is the kinetic order. Their aim was to evaluate the quantitative parameter M and use it for the classification. In each data set least-squares estimations were used to obtain the four parameters of the equation. The analysis of 78 lesions showed that the parameter M highly correlates with malignancy and improved discrimination of benign versus malignant lesions [39].

Degani et al. [16] presented a way to map pathophysiological features of lesions by using intensity values of only three time points of a DCE-MRI scan. This method is commonly known as the Three Time Points (3TP) method. The corresponding three intensity values are the one of the pre-contrast agent injection phase $I(t_1)$ and two after the contrast agent was injected, i.e., $I(t_2)$ and $I(t_3)$. The Initial Signal Increase (ISI) defines how the contrast agent behaves right after it is injected and is calculated by

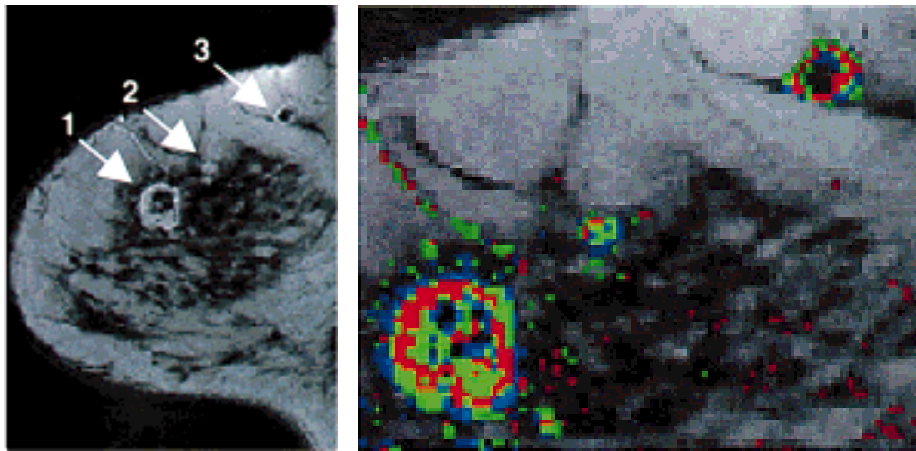
$$ISI = \frac{I(t_2) - I(t_1)}{(t_1 - t_2)}. \quad (2.6)$$

The Post Initial Signal (PIS) defines the behavior after the ISI. It can be classified into three patterns: The *wash-out* pattern is defined as $I(t_2) > I(t_3)$. It shows that intensity values decrease over time. The second one is the *plateau* pattern, defined as $I(t_2) \approx I(t_3)$, which shows intensity values remaining at the same level over time. Finally, the *continuous increase* pattern is defined as $I(t_2) < I(t_3)$. It shows a continuous increase in intensity values over time. Degani et al. used these three patterns to color pixels in the volume. The corresponding colors are red for the wash-out, green for the plateau and blue for the continuous increase pattern. The calculated ISI is used to assign a color intensity [16]. This leads to color-coded images, which can be used to characterize tumor heterogeneity. This 3TP method builds the basis for a lot of other approaches within this thesis. Figure 2.8 shows the principle and a result of the 3TP method. The signals in Figure 2.8a are color-coded according to the described method by Degani et al. [16]. Figure 2.8b shows a result of the 3TP method applied. The left image in Figure 2.8b is an overview slice where three lesions are marked. The right image in Figure 2.8b shows a closeup where the voxels are colored according to the 3TP method.

Fischer et al. investigated if DCE-MRI could change the therapeutic approach for breast cancer [23]. Clinical examination, mammography and mammosonography was used to examine 463 patients and, if necessary, a therapy was suggested. DCE-MRI was then applied to those patients to check whether the results of DCE-MRI would affect the



(a) Curves with corresponding colors.



(b) Result taken from Furman et al. [29].

Figure 2.8: The 3TP method by Degani et al. [16]. **(a)** shows some curves of the 3TP method with corresponding colors. **(b)** shows the 3TP method applied to a slice. The left image gives an overview slice where three lesions are marked. The right image gives a closeup containing the three lesions where the 3TP method was used to color some voxels [29].

therapy decision based on only mammography and mammosonography. To analyze the recorded DCE-MRI data, the authors created a point based scheme. This scheme is known as Göttinger score [22, 23] It assigns different numbers of points to different features derived from the lesion. The features which were used by Fischer et al. [23] to describe breast lesions are the shape, the boundary and the Internal Enhancement Characteristics, as well as the ISI and the PIS (see Table 1.1). To obtain a final classification the sum of all those points is calculated. The smaller this score is, the higher is the possibility that the lesion is benign. The scores for the 548 lesions are assigned by specialists with experience in DCE-MRI analysis. All these 548 lesions were also histopathologically tested. The results show that the sensitivity, specificity, and accuracy were 0.58, 0.76 and 0.62 for clinical examination; 0.86, 0.32 and 0.72 for mammography; 0.75, 0.8 and 0.76 for mammosonography; 0.93, 0.65 and 0.85 for DCE-MRI. Beside these statistical results, MRI helped to adopt the correct therapy for 66 patients (14,3%) [23].

The MammoExplorer, proposed by Coto et al. [14], is an interactive computer-aided diagnosis application to explore breast DCE-MRI data. The aim was to create a novel software application for breast cancer diagnosis and lesion classification. Several approaches have been combined into a single system. One such approach are enhancement scatter plots. Such a (2D) scatter plot depicts voxel intensity values and their ISIs. The enhancement scatter plot can be used for segmentation tasks. If the user selects points on the enhancement scatter plot, the corresponding voxels are selected in the volume image. To visualize the DCE-MRI data sets, False Color Maps (FCMs) are used to highlight the selected voxels (from the enhancement scatter plot) in 2D slices. Two-level volume rendering, a method which combines different rendering methods into a single image (e.g., DVR, MIP, etc.) [33], is used for 3D image generation. This enables the user to define different TFs for different regions of the volume. An example would be to define one TF for the lesions defined with the enhancement scatter plot and another TF for the remaining parts of the volume (e.g., to render it semi-transparently). With this method, an image with a focus and context information can be rendered. Another method implemented in the MammoExplorer is importance driven volume rendering [14, 62]. This method assigns different importance values to specific regions of the volume. The results are parts that are more important and should always be visible while the remaining parts are less important and, depending on the view, do not need to be rendered. This can again be used as focus and context rendering, where parts selected with the enhancement scatter plot are more important and rendered with high priority. The rest of the image is less important and provides the contextual information.

Glaßer et al. [31] presented a visual analytics method with a voxel-wise glyph-based overview in combination with a region-based analysis. The work analyzes the kinetics of single voxels and voxel regions of the lesion. The kinetic features were analyzed using the 3TP method [16]. As opposed to the original work by Degani et al. [16], Glaßer et al. assign a color to a voxel if the relative enhancement of the ISI is higher than 50% and lower than 250%. The voxel is color-coded in red for maximum relative enhancements and blue for minimum relative enhancements. In-between the voxels are interpolated from blue via green to red. Voxels with a relative enhancement $< 50\%$

are rendered in gray. The brightness of the gray voxels correlates with the relative enhancement, whereas the brightness for the color-coded voxels represents their PIS. The saturation for all voxels is set to one. Because this voxel-wise method is sensitive to outliers and might suffer from noise, motion or blurring, voxels with similar perfusion characteristics are grouped together. Perfusion parameters are further kinetic features which are computed based on the Relative Enhancement Curve (REC). A REC is basically the relative change in intensity values over time [31]. Homogeneous lesions, like benign ones, will differ in fewer regions compared to heterogeneous lesions which have more regions. These regions are used to calculate features to analyze a lesion based on the REC. 20 data sets show that the voxel-wise color-coding method allows the user a fast overview of the lesion. In combination with the region merging method, it accelerates the evaluation of suspicious lesions [31].

Quantifying the heterogeneity of breast lesions in DCE-MRI data for the differentiation of benign versus malignant lesions was analyzed by Preim et al. [53]. The first step towards computing and evaluating the heterogeneity was to semi-automatically segment the lesion, which was done by an expert user. Overall perfusion parameters were computed for (connected) regions, which showed similar perfusion characteristics (like it was done by Glaßer et al. [31]). For each region the average REC is computed and the 3TP method was used to classify the REC into one of nine classes [53]. Morphologic features, the individual perfusion parameters, the number of regions and the numbers of 3TP classes were tested on a set of 68 lesions from 50 patients, 31 benign, 37 malignant. The *Mann-Whitney U* test was used for evaluating the ability to classify benign versus malignant lesions. The results show that a high number of regions corresponds to malignant lesions, meaning that these lesions are heterogeneous. Benign lesions had a significantly lower number of regions, hence they are more homogeneous. The number of 3TP classes found in a lesion also showed significant differences between benign and malignant ones. While malignant lesions had more different classes, benign lesions had less. Perfusion parameters did not show significant differences between the groups. However, morphologic features (shape, margin) showed significant differences between benign and malignant lesions [53].

The role of spatial resolution in DCE-MRI was evaluated by Furman et al. [29]. The DCE-MRI data sets were processed using the 3TP method leading to color-coded images. Then, the spatial resolution of the DCE-MRI data was reduced and the 3TP method was applied again. A benign versus malignant classification was performed according to the fraction of colors. If the number of red pixels was above 10% and the number of blue pixels was below 10%, lesions were considered malignant. All other lesions were considered benign. The results of this experiment, tested with 25 malignant and 23 benign lesions, showed that a decreasing spatial resolution correlates with an increase in a false negative diagnosis. The sensitivity of discriminating benign from malignant lesions decreased from 0.76 at the original resolution, to 0.6 at a two fold and to 0.24 at a four fold reduction of the spatial resolution. However, the high specificity was not significantly affected and stayed about 0.96–1.0 [29]. This leads to the conclusion that a high spatial resolution is essential for increasing the sensitivity, but it does not affect the specificity.

Wiener et al. [65] conducted a kinetic and morphologic analysis of 65 suspicious breast cancers in an early stage (BI-RADS[®] category 4 or 5 [18] after mammography and/or mammosonography) acquired by MRI. The objective was to assess the value of DCE-MRI in the diagnosis and treatment of breast cancer in addition to mammography and mammosonography. The following morphologic features were used:

- Maximum lesion size
- Shape
- Contrast agent distribution

They were extracted by expert users. Additionally kinetic features were used, which were acquired through a 3TP approach provided by a specialized software. A minimum area of at least four pixels showing the same characterization was necessary to consider a kinetic feature as representative. If more than one kinetic feature in one cancer were retrieved, the “worst” (which means the most malignant) one was used to represent the entire cancer. The results show that biopsy could have been avoided using DCE-MRI in some cases where tumors had benign characteristics. Moreover, the additional use of DCE-MRI detected more or larger lesions that were not detected by mammography or mammosonography. This means that without DCE-MRI, patients would have received the wrong adjuvant therapy and, thus, the cancer would not have been effectively eliminated.

Another study to evaluate morphologic features was performed by Hauth et al. [34]. First, the 3TP method by Degani et al. [16] was used to color-code a database of 75 suspicious lesions from 62 patients, acquired by DCE-MRI. The PIS was used to color-code voxels (blue for continuous increase, green for plateau and red for the wash-out pattern), and the ISI was used to define the color intensity (slow rates are coded in dark colors, fast rates in bright colors). Then two radiologists extracted the following morphologic features to characterize the breast lesions:

- Maximum diameter
- Shape - round/oval versus spiculated
- Margin - regular versus irregular
- Homogeneity

The evaluation shows that malignant lesions have a higher number of intense and medium red pixels than benign ones. The benign lesions showed more blue pixels than the malignant ones. The authors conclude with: “Quantitative parametric analysis of contrast kinetics in lesions can replace the subjective manual ROI method and makes a step toward standardization of MR mammography.” [34]

Montemurro et al. [46] studied the relationship between morphological and functional features in DCE-MRI data and histopathological characteristics of breast cancer. Their features were classified by the Göttinger score (shown in Table 1.1) [22, 23]. All investigated patients underwent a core biopsy, after DCE-MRI, to acquire histopathological characteristics. The analysis of the DCE-MRI and the histopathological features of the

75 lesions from the 75 patients shows that low Göttinger score points correlate with a high HER2 status and vice versa. The HER2 status is one marker for the aggressiveness of a lesion. This leads to the author’s concerns about using the Göttinger score as representative reporting scheme. But they mentioned that the DCE-MRI feature extraction, was done semi-automatically and might lack reproducibility. They also mentioned that the number of lesions analyzed was small, compared to the number of variables which were acquired. So their results have to be viewed with caution.

The study performed by Williams et al. [66] evaluated the use of kinetic features for benign versus malignant breast cancer classification from DCE-MRI data. First, the Magnetic Resonance (MR) images were analyzed by experts according to the BI-RADS[®] scheme. Additionally, mammosonography was performed as well. After the first classification, the MR images were processed by a CAD system, which applied the 3TP method to color code pixels [16]. Opposed to the original work by Degani et al. [16], the ISI was used to specify whether a pixel was color-coded or not. Similar to the approach by Glaßer et al. [31], this was done by specifying a threshold for the relative enhancement of the ISI and, if this threshold was exceeded, the pixel was color-coded. The coloring was done as described by Degani et al. [16]. Then, a second interpretation of the MR images was done with the additional color-coded information. The results show that the use of kinetic information significantly improved the classification of benign versus malignant tumors [66].

Beside the use of morphologic and kinetic features derived from T1-weighted DCE-MRI, Aalst et al. [61] added T2-weighted volumes, which are usually part of DCE-MRI examinations, for discriminating benign versus malignant breast lesions. After the lesions were semi-automatically segmented using the T1-weighted MR images, morphological and kinetic features from these images were computed. The same segmentation was also used for the T2-weighted images to compute additional features. Using the additional features, the classification performance improved the non-parametric estimates of the AUC of the ROC from 0.94 to 0.99.

The study performed by Nie et al. [49] used textural features of segmented lesions, in addition to morphologic features, to investigate the feasibility for benign versus malignant lesion classification. To derive the features of the 43 malignant and 28 benign lesions, a segmentation of the lesions was necessary, which was done semi-automatically. First, an expert user selects the ROI, and then a software algorithm generates a binary segmentation map. All voxels contained in this segmentation map are used to compute eight morphologic features and ten textural features. Finally, an Artificial Neural Network (ANN) algorithm selected features optimal for classifying benign versus malignant lesions. This algorithm chose the following morphologic features:

- Compactness
- Lesion volume
- Normalized Radial Length (NRL) entropy

Additionally it chose these textural features:

- Gray level entropy
- Gray level sum average
- Homogeneity

Combining these features lead to an AUC of the ROC of 0.86. If the data set is split into half training set and half validation set, the ANN chose five features (compactness, NRL entropy, gray level entropy, gray level difference variance and homogeneity) and achieved an AUC of 0.83. In this study, the morphologic feature *compactness* was among the most important ones. This feature alone would be able to achieve an AUC of the ROC of 0.7. Compactness is defined as the ratio of the surface area to the volume. This can be associated with shape and margin in the BI-RADS[®] lexicon [49]. Among texture features the two most important ones, derived from gray level co-occurrence matrices, were the gray level entropy, which is a measure of randomness, and the gray level sum average. These two features can be associated with the homogeneity and heterogeneity of the BI-RADS[®] lexicon according to the authors [49].

Okafuji et al. [50] evaluated features computed from DCE-MRI data sets for the special case of circumscribed mass lesions in breasts. Circumscribed mass lesions, are lesions that have a well defined area (mass), which means that they can be clearly differentiated from normal tissue. To perform the study, the authors used 90 breast lesions, where 43 were malignant and 47 benign. Two experts recorded the following features based on the BI-RADS[®] scheme [59]: shape, margin, internal enhancement, ISI and PIS. The results were computed using a chi-square or Fisher's exact test with a step-wise logistic regression analysis [50]. The results show that the most important features for discriminating benign versus malignant lesions with circumscribed masses are the internal enhancement and the kinetic features. The combination of the dynamic wash-out pattern with either rim or heterogeneous enhancement resulted in a prediction probability of malignancy with > 0.95 [50].

While most of the MRI data for breast cancer research was acquired with 1.5 T MRI, Schmitz et al. [56] evaluated the use of 3.0 T MRI. The classification of the breast lesions was performed by two experts according to the BI-RADS[®] scheme [59]. Morphologic features such as shape, margin and enhancement pattern, as well as the kinetic features of the PIS (continuous increase versus plateau versus wash-out) were evaluated. Additionally the vascularity score, which counts the number of vessels based on a vessel's length and its transverse diameter, was computed. This score was first described by Sardanelli et al. [55]. The vascularity score was computed using a MIP of the first fat suppressed, high resolution T1-weighted dynamic series. The results were obtained on a total of 56 lesions, 25 were malignant and 31 were benign. Using the morphologic and kinetic features for breast cancer analysis lead to a sensitivity of 1.0 and a specificity of 0.74. If the vascularity score was added to the analysis, the sensitivity remained at 1.0 but the specificity increased to 0.87 [56].

Baltzer et al. [6] made a statistical evaluation of the time curve distribution of an entire lesion and checked whether this time curve is a significant factor for benign versus

malignant lesion classification. They concluded that there is no statistical evidence for this assumption, even though in many cases it can be an indicator for malignancy.

Gal et al. [30] published an evaluation where they used textural features in combination with kinetic information for automatic breast lesion classification. Ten malignant and ten benign lesions acquired with DCE-MRI were used. The lesions were located and manually segmented by an expert user. This was done by defining a ROI and applying a connected component analysis. The connected component analysis starts at an initial voxel (seed point) and groups neighboring voxels together that show similar characteristics (like similar intensity values). Typically, the user defines the seed points and the threshold for binarization. To perform the analysis, morphological features (based on the binary mask), textural features (based on the intensity values masked by the binary mask) and kinetic features (based on individual or mean intensity values selected by the binary mask) were computed. The best features and classifiers were evaluated using an exhaustive search approach. To evaluate the features several different classifiers were used: Logistic regression, Fisher's linear discriminant analysis, linear Bayesian discriminant analysis and Support Vector Machine (SVM) with different kernels. The SVM with the sigmoid kernel performed best in the author's experiments (measured by the AUC) using textural features in combination with the mean of the PIS. The results of the study show that the morphological features only had a small impact on the classification results [30]. However, the results of this evaluation need to be taken with caution as the number of samples is very small.

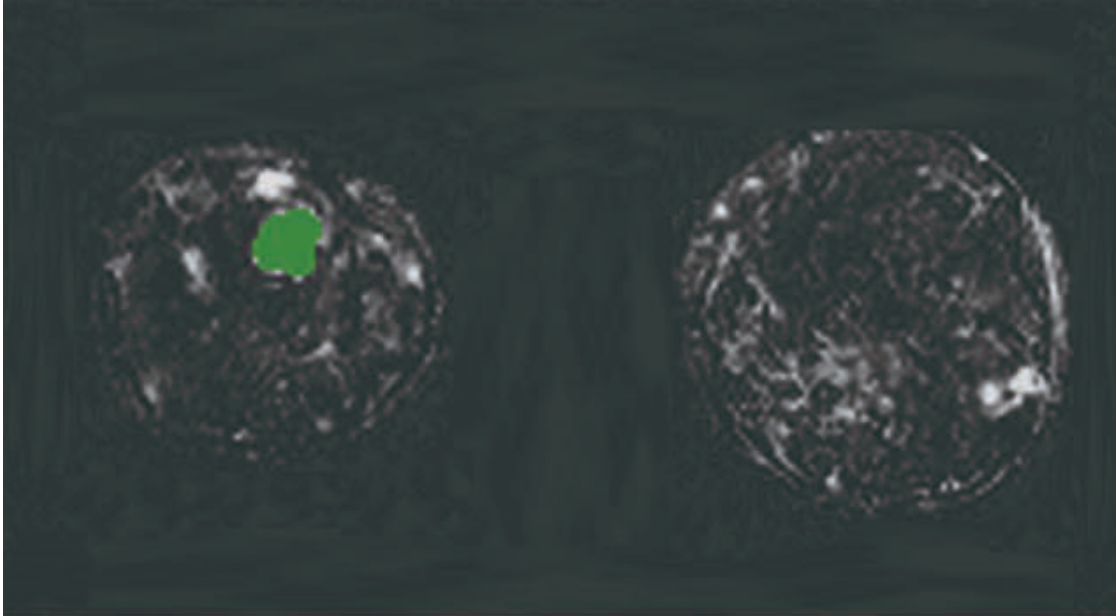
Karahaliou et al. [38] published a method for computing the heterogeneity of breast lesions acquired with DCE-MRI based on textural information. First, two experts select one slice of the volume containing the largest cross-section of the lesion. Then, three parameters based on the 3TP method were calculated for each pixel of the slice, forming three maps containing the ISI, the PIS and the Signal Enhancement Ratio (SER), which is another measure of the PIS in combination with the ISI relative to the pre-contrast intensity value [38]. Using these parametric maps several features are computed based on four Gray Level Co-occurrence Matrices (GLCMs). To classify the lesions a Least Squares Minimum Distance (LSMD) classifier was used. A stepwise feature selection procedure was employed to get a subset of features feasible to classify benign versus malignant lesions. The classification results, based on 82 lesions (51 malignant and 31 benign), of the SER map with the selected texture features reached an AUC of the ROC of about 0.922. The PIS map performed with an AUC of 0.906 whereas the ISI map got 0.767. The authors claim that the heterogeneity of parametric maps could contribute to the computer-aided diagnosis of breast lesions in DCE-MRI [38].

The aim of the work published by Agner et al. [5] is similar to the one from Karahaliou et al. [38]. In order to evaluate textural features for the feasibility to discriminate benign versus malignant lesions, one slice of each lesion was taken to represent the whole lesion. Therefore, an expert user had to extract a single representative slice of each of the 41 lesions (24 malignant, 17 benign). The lesion's slice was used to extract morphologic, texture and, like in the work of Karahaliou et al. [38], textural kinetic features, as well as intensity value kinetic features. Agner et al. show that the textural kinetic features

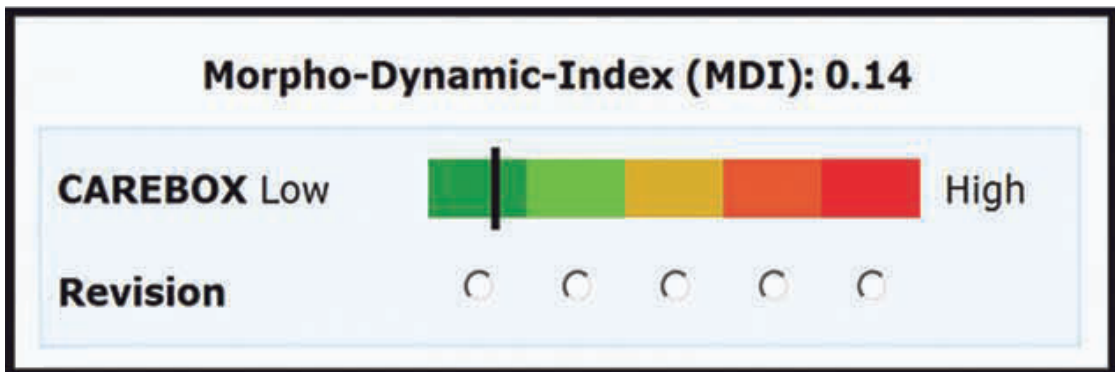
combined with a Probabilistic Boosting Tree (PBT) classifier yielded an AUC of the ROC of 0.92, a sensitivity of 0.95 and a specificity of 0.82. Combining the textural kinetic features with the morphologic features leads to an accuracy of the PBT classifier with an AUC of 0.91, a sensitivity of 0.99, and a specificity of 0.76. More information is given in Agner et al. [5].

Renz et al. [54] evaluated the CAD prototype for fully automatic breast cancer diagnosis in DCE-MRI published by Mayer et al. [45]. The evaluation was done with a total of 141 MR images of histologically proven mass-like lesions (88 malignant, 53 benign). The aim was to assess the CAD system's ability to detect and classify mass-like lesions. In order to detect the lesions, the CAD system used a segmentation technique which is based on a hierarchical 3D Gaussian pyramid in combination with an adaptive threshold. The result was a ROI which contains the lesion. The CAD system computes a Morpho-Dynamic-Index (MDI), which is a quantitative number in the range of 0% – 100%, representing the lesions probability of being malignant. A high number corresponds with a high probability of being malignant. The MDI is visualized as a black bar in a color-coded box ranging from green to red, where green represents a low and red a high probability of being malignant. The MDI is computed by combining morphological and kinetic features. To describe the morphology of a lesion 13 parameters were calculated which are derived from shape-based features as well as texture features. Further eight features are calculated to describe the kinetics of a lesion. Finally an ANN was trained with a set of 600 histologically verified lesions. This ANN was used to calculate a lesion's probability of being malignant which is visualized in the MDI. The set of lesions which were used to evaluate the CAD system, were not part of the lesions used to train the ANN. The CAD system detected 86 of 88 malignant lesions with a mean MDI of 86.1% and 49 of the 53 benign lesions with a mean MDI of 41.8%. Its diagnostic accuracy, based on the ROC analysis, was 93.5% using an appropriate cutoff value of 50.0%. The sensitivity of the CAD system was 96.5% and its specificity 75.5% [54]. Figure 2.9a shows a slice of an MRI data set containing a benign lesion. The lesion has a low MDI value resulting in a green color coding in the slice image. Beside this benign example, Figure 2.10a shows a slice containing a malignant lesion which has a high MDI value resulting in a red color coding in the slice view. Figure 2.9b and Figure 2.10b show the described visualization of the MDI value using a colored box and a black bar.

Sim et al. [60] presented a method for automatic breast cancer detection. One of the features is the automatic ROI selection to reduce the computation time for further analysis. Based on an Optical Character Recognition (OCR) approach, which is used for detecting numbers and letters in (scanned) texts, the ROI is defined. Then the ROI is used for further automatic segmentation of the breasts. A Fourier based method is used to sharpen the images and get rid of motion artifacts. This method first converts the images into the Fourier space. Then the images of the post-contrast time series are reconstructed by computing the Inverse DFT (IDFT) with the pre-contrast phase image and the post-contrast magnitude image. This emphasizes the desired intensity values for the feature extraction and classification. Using those images a voxel based classification based on the 3TP method is done. The voxels of the reconstructed images are categorized

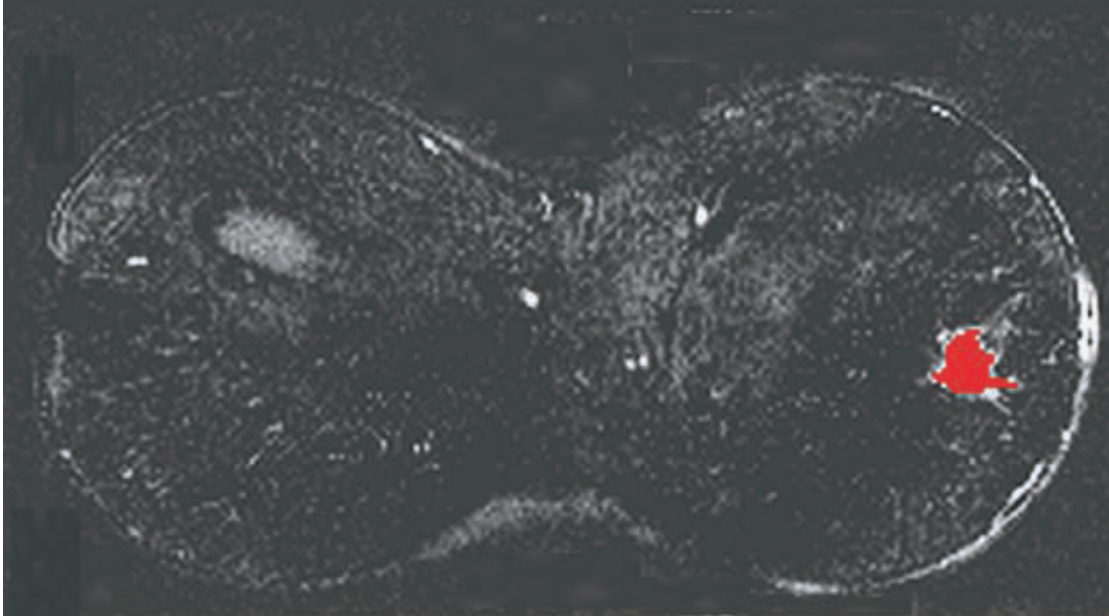


(a) Slice of a breast with a benign lesion.

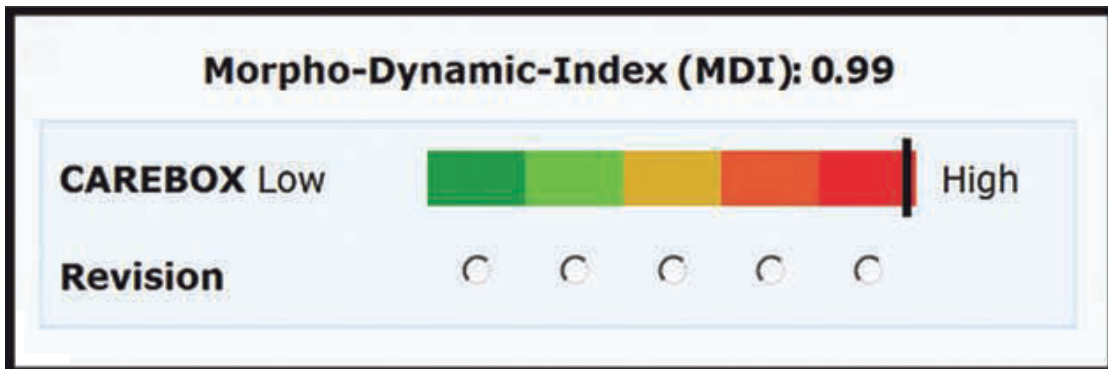


(b) Morpho-Dynamic-Index (MDI) with low value.

Figure 2.9: The result of the CAD system published by Mayer et al. [45] which was evaluated by Renz et al. [54]. (a) shows a slice of an MR image with a detected benign lesion. (b) shows the result and the visualization of the MDI computation. The lesion in (a) is color-coded with the color defined by the MDI, which is marked with a black bar in (b). The images are taken from Renz et al. [54].



(a) Slice of a breast with a malignant lesion.



(b) Morpho-Dynamic-Index (MDI) with high value.

Figure 2.10: The result of the CAD system published by Mayer et al. [45] which was evaluated by Renz et al. [54]. (a) shows a slice of an MR image with a detected malignant lesion. (b) shows the result and the visualization of the MDI computation. The lesion in (a) is color-coded with the color defined by the MDI, which is marked with a black bar in (b). The images are taken from Renz et al. [54].

into benign, suspicious and malignant based on the 3TP method [16]. Benign voxels have a continuous intensity value increase and are colored in green. Voxels with an ISI showing a fast intensity value increase and a plateau PIS pattern are categorized as suspicious and are colored in yellow. Voxels classified as malignant, having an ISI with a fast increase in intensity value and a wash-out PIS pattern, are colored in red. It was not discussed by Sim et al. if all voxels of a breast, or just some segmented voxels belonging to a lesion are classified. The computed voxel-wise classifications are used for a 3D visualization. Beside the 3TP method, inter-slice analysis is done by calculating the center of mass of each lesion. However, how the inter-slice analysis contributes to the classification was not discussed. The benign versus malignant lesion classification is finally done by experts who used the color-coded 3D visualizations to make a diagnosis, which results in a classification sensitivity of 0.9, a specificity of 0.9063 and an accuracy of 0.9024 [60]. Even though this looks like a promising approach, there remain open questions such as how the classification is done, which voxels are used for calculating the features and what influence the center of mass of the inter-slice analysis has.

2.4 Libraries

We made use of well-known libraries to achieve our goals within the given time constraints. A library is a collection of methods and functions that can be used by different programs. Such libraries help to reduce the implementation work by providing solutions to common problems. In the following, the main libraries are described. More information on the employed libraries can be found either in books, publications or on their websites. To load, export and segment data sets within our framework the Medical Imaging Toolkit [2] (MITK) [68], which includes the Insight Segmentation and Registration Toolkit [1] (ITK) [69] and the Visualization Toolkit [4] (VTK) [57], is used. Qt, an open-source graphical UI framework, is taken to create the user interface. OpenGL provides functionality to do the 2D and 3D rendering. FFTW3 [26] is used to compute the DFT of volumes.

2.4.1 ITK

ITK is an open-source C++ toolkit crafted for segmentation and registration of volume data. Segmentation is the process of defining certain entities with similar properties to belong to the same object, like a cancer. The toolkit provides a lot of different methods to achieve this in various applications (like medical brain imaging, vessel visualization, etc.). It can also be used to export the segmented objects as a mesh. Registration is the method of aligning different data sets that are either measured at different timestamps or with different modalities. An example is to align a CT scan of a certain part of the human body, with the corresponding MRI scan. However, we do not utilize such a feature in the current version of our software.

The ITK project was started in 1999 by the US National Library of Medicine of the National Institutes of Health. Since then a lot of different companies as well as software developers and researcher contributed to the development of this framework [69].

2.4.2 VTK

VTK is an open-source toolkit tailored for scientific as well as information visualization, rendering of 3D graphics and image processing. It also provides methods to show 3D widgets in renderings, and 2D and 3D annotations.

VTK was started as part of the textbook *The Visualization Toolkit - An Object-Oriented Approach to 3D Graphics* in 1998 [57]. Many contributions came from big medical imaging companies, like GE Healthcare, researchers around the world, as well as software developers who still develop and improve it.

2.4.3 MITK

MITK is a C++ toolkit that combines ITK and VTK. It provides wrapper objects and functions to easily access the functionality provided by those two toolkits. Furthermore, it extends the functionality for special medical scenarios. MITK can be used as a standalone program which can be extended by plug-ins as well as a framework which offers all the functionality for self-developed software projects [68].

2.4.4 FFTW3

FFTW3 is a library that implements the FFT algorithm for the DFT calculation [26]. The library is written in C and is usable in many applications. It is capable of computing the DFT in one and more dimensions of arbitrary input size and for real and complex data. It is published under the GNU General Public License (GPL).

Methodology

In this chapter we describe our approach for automatically computing features for breast cancer analysis as well as how to visualize them. Before we describe our approach, we want to discuss how a breast cancer diagnosis is performed currently. A patient with already diagnosed abnormalities in her breast is scanned using an MR scanner. Then, the radiologist uses various CAD systems to analyze this acquired volume. First, the radiologist has to identify the lesion unless it is automatically done by a CAD system. Afterwards, the radiologist marks a point or ROI in order to evaluate the kinetic behavior of the contrast agent during the scanning, which has significant impact on the outcome of the diagnosis. Another important aspect is the morphology of the lesion. To inspect the morphology, the radiologist analyzes the axial or transverse slices of the MR data set. Some CAD systems assist the radiologist in assessing the morphology by color coding parts of the volume. These color codings are often based on the kinetics of the acquired MRI data sets. With the color-coded slices, the radiologist then defines the lesion's shape, boundary and IEC. Combined with additional information from CAD systems, like the volume of a lesion, its minimum and maximum diameter, the final diagnosis is done and the results are saved in a textual document.

In the daily clinical routine, a radiologist does not use only a single CAD system. In breast cancer diagnosis a broad spectrum of CAD systems is used. Some CAD systems compute the probability of malignancy automatically. Examples are the system by Mayer et al. [45] or the system by Renz et al. [54] who compute the MDI. Others, however, solely assist the radiologist in decision making by, e.g., color-coding the voxels. This can be done using the 3TP method by Degani et al. [16]. But there are also more improved color coding methods like the one presented by Glaszer et al. [31], or Preim et al. [53]. The results of such systems are used to assess a lesion's malignancy.

Before we create such a CAD system, we need to know how such a system has to be designed so that it optimally assists a radiologist in breast cancer diagnosis. Therefore we talked to experienced radiologists to get an in-depth understanding of their daily needs from such a software system. We derived from discussions that they expect a system

that computes a quantitative representation of a single lesion being malignant or benign. User interaction should be kept as minimal as possible, optimally by just marking a lesion and obtaining its corresponding classification. Despite this, we figured out, that a single quantitative value is not sufficient as our domain experts specifically mentioned that they want to know the reasons for the classification too. Hence, we decided for an overview first, showing the classification number, and details on demand, showing each single component leading to the classification. This follows the information seeking mantra by Shneiderman [58]. The visualizations stored in the well-established DICOM format would seamlessly integrate into the workflow of our domain experts and could be readily used for the following three tasks:

1. **Biopsy:** One task is to check whether a biopsy was done successfully or not. Let us assume, that our system diagnoses a highly malignant lesion, but the biopsy was negative. Then, the chance that a physician did not catch a cancerous cell during the biopsy is high and the biopsy has to be repeated which is quite an invasive intervention. On the other hand, if the biopsy is negative and the system diagnosed a probably malignant lesion, it is more likely that the lesion is definitely benign.
2. **Documentation:** It is necessary to access the data at any given time by all the responsible physicians.
3. **Therapy monitoring:** This is necessary to check whether the patient is responding to a therapy or not.

Having all this information at hand, we derived the following requirements for our software. A radiologist is willing to draw a ROI. An automatic lesion detection is thus not essential. However, ROIs defined by radiologist may not be consistent in size and position. Therefore, a CAD system needs to handle such varieties and deliver robust computations. The results should present a quantitative value which represents the likelihood of malignancy. Contextual information should also be included which describes why a certain quantitative value was computed. The results should be stored in the Information Technology (IT) infrastructure used by the radiologist and the hospital to be accessible for all the responsible physicians.

Our system requires a set of ROIs containing a breast lesion as input. It then computes and presents a quantitative value representing the lesion's probability of being malignant in combination with additional information which shows why this result was computed. As we explicitly decided to avoid segmentation of the highly varying lesions, we employ a Fourier-based approach to compute a lesion's morphologic features. The reasons for this decision are that segmentation algorithms are an extra overload for the software system and are an additional source of errors. On the other hand, doing a segmentation manually is a very time and resource consuming activity. Having the features computed, we present a quantitative value in combination with contextual information in a novel way. Our design of the plot is based on star plots and the sunburst Malignancy Area Plot (MAP) serving as normalized visualizations which are also evaluated by radiologists.

3.1 Feature Computation

As the main idea behind our work is to compute classification-relevant features without cancer segmentation, we employ a Fourier analysis. In general, we use three of the eleven available timestamps of the DCE-MRI volume data to compute features specified by the Göttinger score:

1. One from the pre contrast phase ($t_1 = 58.1s$), where no contrast agent was injected into the patient.
2. Time stamp $t_2 = 181.6s$ is right after the contrast injection.
3. The last time stamp $t_3 = 388.0s$ is from a late stage after the contrast agent injection. At this time, the lesion has already been entirely covered by contrast agent and the contrast agent starts to diminish already.

We compute the following morphologic features, specified by the Göttinger score: the boundary, the shape and the IEC. The kinetic features are analyzed for the entire data set, computed with the 3TP method by Degani et al. [16].

Our workflow is shown in Figure 3.1. The only required user interaction is the specification of a ROI wherever a lesion is located within the data set. Then, the computation and analysis is done fully automatic by our proposed solution. Every step of the workflow is described in more detail in the following subsections.

3.1.1 Region Of Interest (ROI) Definition

Segmentation is not a trivial task. Depending on whether it is done manually, semi-automatically or automatically the user input varies. A manual segmentation may end up in a time-consuming task. Semi-automatic segmentation may not be as time-consuming as manual segmentation, but, for each semi-automatic approach the user has to provide different inputs, which requires special training. However, semi-automatic, as well as automatic, approaches may not be as precise as manual segmentations. To overcome these disadvantages of segmentation, one of the main aspects of our work is to avoid segmentation at all and stick to a well-known and established process in medical imaging, i.e., defining a ROI.

A ROI significantly reduces the number of voxels to analyze, but it requires the user to identify the lesions in the volumetric data set beforehand. Furthermore, the user needs to consider that one ROI should only contain a single lesion. The lesion should be located in the middle of the ROI. The ROI selects sub-volumes from each of the three required timestamps from the DCE-MRI data set. After the user finished selecting the ROI, he can start the computation of the features.

Technically, the selection of the ROI is designed by letting the user choose voxels that specifies the ROI. To do that, he or she needs to interact with the slice rendering. The selection can be done by one of the following three possible ways:

1. **Single voxel selection:** This is used to select single interesting voxels. This method is useful, for example, to specify the borders of the ROI.

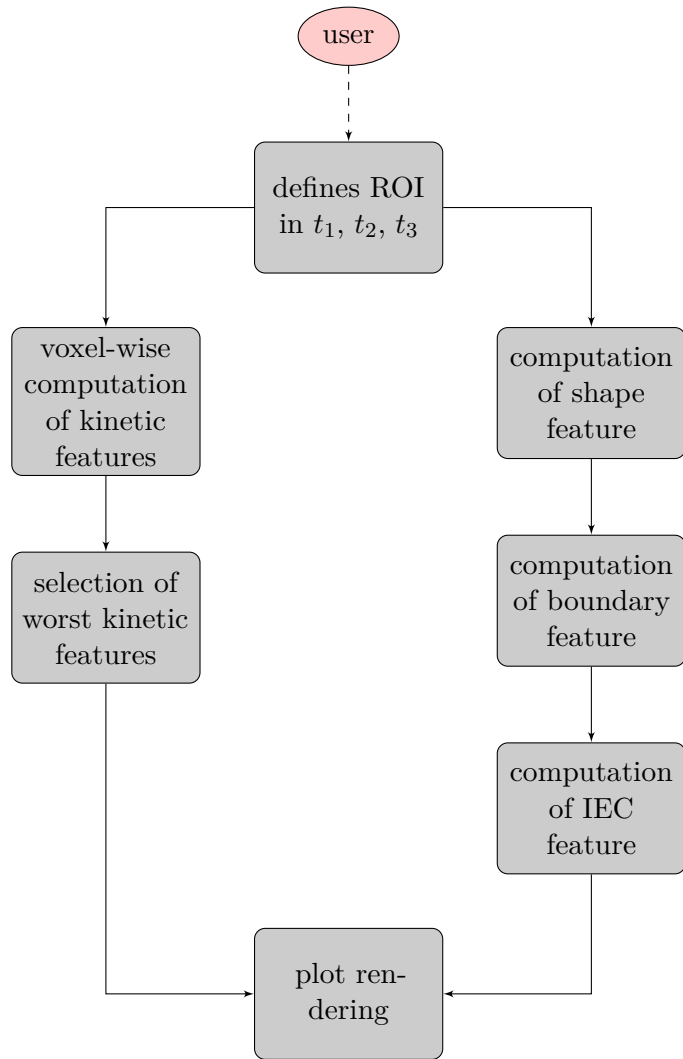


Figure 3.1: Workflow of our automatic breast lesion investigation.

2. **Spherical voxel selection:** This method selects all voxels within a sphere. The user first specifies the center voxel of the sphere and by keeping the mouse button pressed and moving the mouse, the user can adjust the radius. The changes will immediately be reflected in the slice rendering.
3. **Cuboid voxel selection:** All voxels inside a cube are selected. The user selects the middle of the cube and by keeping the mouse button pressed and moving it, the cube's size will be adjusted. The changes will immediately be reflected in the slice rendering.

After defining the mask volume, new sub-volumes can be created. Figure 3.2 shows a whole DCE-MRI data set. The green rectangles define the borders of the ROI, the resulting sub-volume is shown on the right side.

3.1.2 Fourier Transform

In this thesis we apply the Fourier transform in order to compute suitable features for breast cancer diagnosis. As our key requirements is to avoiding segmentation in its entirety, we investigate the feasibility of the frequency domain for computing the morphologic features of the Göttinger score. The work by Bhalerao and Wilson [8] presented a method for estimating local 3D features of a volume data set using a Fourier approach. The authors demonstrate this method on an MRI data set in order to determine the blood vessels. Motivated by this idea we utilize the inertia tensor to compute the morphologic features in the frequency domain. We define $f(\vec{x})$ as the intensity value of a volume data set at the spatial position \vec{x} . Further, we use $\hat{f}(\vec{u})$ as the Fourier transformed volume with its spectral energy at frequency \vec{u} . A single Fourier magnitude value is indicated as $|\hat{f}(\vec{u})|$.

Inertia Tensor

The moment of inertia tensor, or inertia tensor for short, is a tensor which, in physics, is used to describe the moments of inertia. It defines how much torque is needed to accelerate a rigid body about a rotational axis. We denote \mathbf{J} as the inertia tensor with the structure based on Equation 2.1:

$$\mathbf{J} = \begin{pmatrix} J_{xx} & J_{xy} & J_{zx} \\ J_{yx} & J_{yy} & J_{zy} \\ J_{zx} & J_{zy} & J_{zz} \end{pmatrix} \quad (3.1)$$

Inertia tensors for real world objects are thus 3×3 diagonal matrices. J_{xx} is called the moment of inertia about the x -axis, J_{yy} the moment of inertia about the y -axis and J_{zz} the moment of inertia about the z -axis. J_{xy} is the xy product of inertia, J_{xz} the xz product of inertia and J_{yz} the yz product of inertia [24]. The inertia tensor is a real symmetric matrix, i.e., $J_{xy} = J_{yx}$, $J_{xz} = J_{zx}$ and $J_{yz} = J_{zy}$. The diagonal elements J_{xx} , J_{yy} and J_{zz} describe the torque that is required to rotate a body about its x , y and z axis. The product of inertia defines how much torque is needed to rotate a body about an

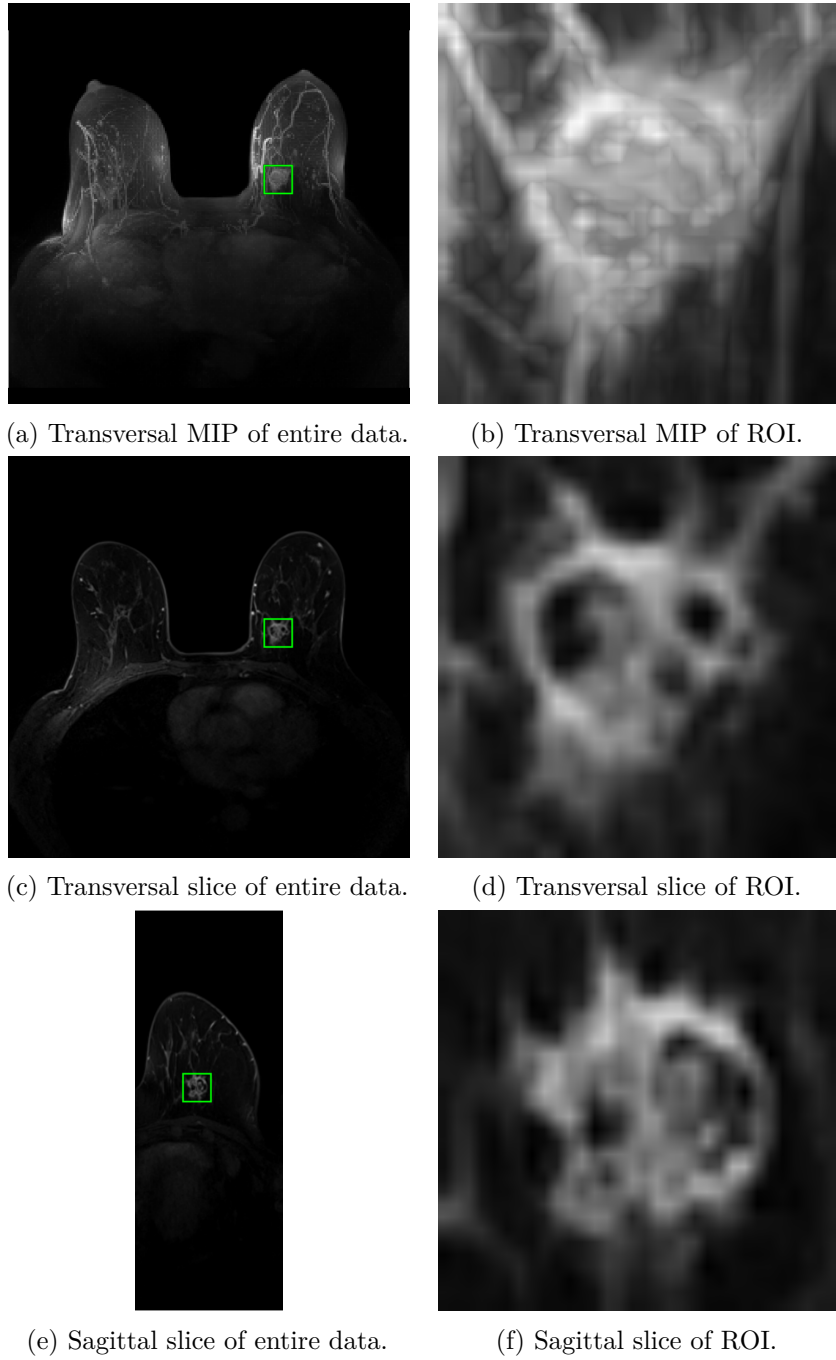


Figure 3.2: A DCE-MRI scan of a breast. The images on the left show the whole data set of the same breast, while the images on the right show the ROI, specified with the green rectangle, containing the same lesion. The first row is rendered using MIP viewed from the same direction (transversal). The last two rows are slice renderings viewed from two different directions (transversal, sagittal).

axis while it is rotating about another axis. J_{xy} , can thus be interpreted as the moment of inertia about the x -axis, while the body is rotating about the y -axis. The same applies for J_{xz} and J_{yx} .

Bigün [9] and Jähne [37] use the inertia tensor of 2D Fourier transformed images to do local image analysis, especially for computing a local orientation. Nevertheless, we are able to derive more information from the inertia tensor: Looking closer at Equation 2.2, we see that J_{xx} increases with the spectral energy that is distributed over the x -axis, the same applies for J_{yy} with the y -axis and for J_{zz} with the z -axis in the 3D space. The further the frequency of a spectral energy is away from the center, the more influence it has on the result. The spectral energy at the center, with frequency position $\vec{u} = [0, 0, 0]$, does not influence the result. Thus, the values in the diagonal provide the information about the amount of high frequencies the spatial image has. Higher diagonal values of \mathbf{J} indicate more high frequencies along its corresponding axis. The elements above (and below) the diagonal of \mathbf{J} give information about the spectral energy distribution in their respective planes. In the 2D example, J_{xy} represents the distribution of spectral energy along the diagonal, while in the 3D case J_{xy} represents the distribution of spectral energy in the xy plane, J_{xz} in the xz plane and J_{yz} in the yz plane. This means that the inertia tensor is a representation of the distribution of the spectral energy of a Fourier transformed image. This information is used by Bigün [9] to describe the orientation of local neighborhoods in images. Wilson et al. [67] use this information for estimating boundaries in images. Bhalerao and Wilson [8] use the inertia tensor to describe local features in volumes for blood vessel detection.

3.1.3 Morphologic Features

In order to compute the morphologic features we are extracting some information regarding the shape of the Fourier magnitude volume, based on the inertia tensors. For every subsequent feature we determined a way to compute values that are capable of classifying the feature. The thresholds used for the classification of a feature were defined based on the observations of synthetic and real world data sets.

Shape

The Göttinger score classifies a shape either as *round/oval* or *irregular*. In order to compute the shape using the Fourier transform, we use the method described by Bhalerao and Wilson [8] to compute local 3D features. First, we compute a volume data set, denoted as f , containing the enhanced lesion with suppressed tissue by subtracting the volume of the pre-contrast phase t_1 from the volume of the late post-contrast phase t_3 . Then, we split the volume into eight equally-sized sub-volumes f_i and compute the inertia tensor \mathbf{J}_i of the Fourier transformed sub-volume $|f_i|$, where i defines the index of the

sub-volume. In the next step, a tensor containing the mean values of the inertia tensors of the sub-volumes is computed:

$$\bar{\mathbf{J}} = \frac{1}{N} \sum_{i=1}^N \mathbf{J}_i, \quad (3.2)$$

where N is the number of sub-volumes, which is eight. Our assumption is, that if an object is symmetric the diagonal elements in the inertia tensor are the same in each sub-volume, i.e., the mean tensor has also the same diagonal elements. Furthermore, the elements in the upper (and lower) triangle of the mean tensor cancel out if the volume has a symmetric structure. In the third step, the mean tensor $\bar{\mathbf{J}}$ is used to compute the spherical feature $F_s(\bar{\mathbf{J}})$ using the Eigenvalues of the tensor with Equation 3.5 [8]. If the object is symmetric, e.g., spherical, this value is ≥ 0.5 . Based on experiments, we define a threshold of $F_s(\bar{\mathbf{J}}) \geq 0.667$ for considering a lesion as being symmetric. The linear, planar and spherical features are computed as follows [8]:

$$F_l = \frac{(\lambda_2 - \lambda_3)}{\lambda_1} \quad (3.3)$$

$$F_p = \frac{(\lambda_1 - \lambda_2)}{\lambda_1} \quad (3.4)$$

$$F_s = \frac{\lambda_3}{\lambda_1} \quad (3.5)$$

In order to consider the spherical components in the classification of a lesion, apart from the symmetry, we subtract the mean tensor $\bar{\mathbf{J}}$ from each of the inertia tensors \mathbf{J}_i of the sub-volumes. The resulting tensors \mathbf{J}'_i describe how the sub-volume differs from the mean tensor. In case of a symmetric and spherical object, the diagonal elements cancel out and the tensors \mathbf{J}'_i contain only elements in the upper (and lower) triangle, which define how the sub-volumes differ. Using this subtracted tensor, we now compute the planar feature $F_p(\mathbf{J}'_i)$ of each sub-volume using the tensor's Eigenvalues with Equation 3.4 [8]. If the sub-volume contains a quarter of a sphere, the planar feature is defined as: $F_p > F_s$ and $F_p > F_l$ where F_l defines the linear feature computed using the Eigenvalues with Equation 3.3 [8]. For the whole volume, we compute the mean of the spherical, planar and linear features as follows:

$$\bar{F}'_l = \frac{1}{N} \sum_{i=1}^N F_l(\mathbf{J}'_i) \quad (3.6)$$

$$\bar{F}'_p = \frac{1}{N} \sum_{i=1}^N F_p(\mathbf{J}'_i) \quad (3.7)$$

$$\bar{F}'_s = \frac{1}{N} \sum_{i=1}^N F_s(\mathbf{J}'_i) \quad (3.8)$$

Thus, a lesion in a volume has a spherical structure if $F_s(\bar{\mathbf{J}}) > 0.667$ and if $\bar{F}'_p > \bar{F}'_s$ and $\bar{F}'_p > \bar{F}'_l$. Otherwise the structure in the volume can be considered as irregular. The Göttinger score assigns 0 points for spherical structure and 1 point for irregular ones.

Figure 3.3 shows a 2D example of the shape classification. For each of the four sub-images the Fourier transform $|\hat{f}_i|$ and the inertia tensors \mathbf{J}_i are computed. All inertia tensors \mathbf{J}_i in Figure 3.3 have the same diagonal elements, and we also see that in the mean tensor $\bar{\mathbf{J}}$ the upper or lower values cancel out. Despite the 3D case, the 2D case can only distinguish between circular structures computed with $F_c = \lambda_2/\lambda_1$ and linear structures which is computed with $F_l = (\lambda_1 - \lambda_2)/\lambda_1$. Computing the circular feature of the mean tensor results in $F_c(\bar{\mathbf{J}}) = 0.99$, which fulfills the first assumption that $F_c(\bar{\mathbf{J}}) > 2/3$. In contrast to the 3D case, an image is considered being circular in the 2D case if $\bar{F}_l' > \bar{F}_c'$. Computing \bar{F}_l' and \bar{F}_c' results in $\bar{F}_l' = 2$ and $\bar{F}_c' = -1$ and since $\bar{F}_l' > \bar{F}_c'$ the object in the image can be considered as being a circle. For comparison reasons the magnitude of the Fourier transform $|\hat{f}|$ of the entire image is also shown in Figure 3.3.

Figure 3.4 shows a similar example of a star-shaped object. For each of the four sub-images the Fourier transform $|\hat{f}_i|$ and the inertia tensors \mathbf{J}_i are computed. All inertia tensors \mathbf{J}_i in Figure 3.4 have the same diagonal elements, and we also see that in the mean tensor $\bar{\mathbf{J}}$ the upper or lower values cancel out. Computing the circular feature of the mean tensor results in $F_c(\bar{\mathbf{J}}) = 0.99$, which fulfills the first assumption that $F_c(\bar{\mathbf{J}}) > 2/3$. Computing \bar{F}_l' and \bar{F}_c' results in $\bar{F}_l' = -0.35$ and $\bar{F}_c' = 1.35$ and since $\bar{F}_l' < \bar{F}_c'$ the object in the image can be considered as being irregular. For comparison reasons the magnitude of the Fourier transform $|\hat{f}|$ of the entire image is also shown in Figure 3.4.

Figure 3.5 shows a similar example of an irregular-shaped object. First, for each of the four sub-images the Fourier transform and the inertia tensors are computed. The inertia tensors in Figure 3.5 differ all from each other. However, computing the circular feature of the mean tensor results in $F_c(\bar{\mathbf{J}}) = 0.98$, which fulfills the first assumption that $F_c(\bar{\mathbf{J}}) > 2/3$. The circular feature is also high if an object is highly irregular, i.e., isotropic. Computing \bar{F}_l' and \bar{F}_c' results in $\bar{F}_l' = -0.4$ and $\bar{F}_c' = 1.40$ and since $\bar{F}_l' < \bar{F}_c'$ the object in the image can be considered as being irregular. For comparison reasons the magnitude of the Fourier transform $|\hat{f}|$ of the entire image is also shown in Figure 3.5.

Boundary

Based on the Göttinger score, a lesion can be classified by its boundary. The boundary can either be smooth (Figure 3.6a), characterized by an abrupt change in intensity values from the lesion to the surrounding tissue, or it can also be classified as blurred (Figure 3.6d), characterized by a continuous change in intensity values from the lesion to the surrounding values.

In order to classify the boundary of a lesion into smooth or blurred, we use a Fourier-based approach for assessing the frequencies of the same sub-volumes used for the shape classification. The diagonal of the mean tensor $\bar{\mathbf{J}}$ describes the amount of high frequencies within the sub-volumes. In order to classify the boundary we compute the mean of the diagonal elements of $\bar{\mathbf{J}}$:

$$\text{Boundary} = \frac{\bar{J}_{xx} + \bar{J}_{yy} + \bar{J}_{zz}}{3} \quad (3.9)$$

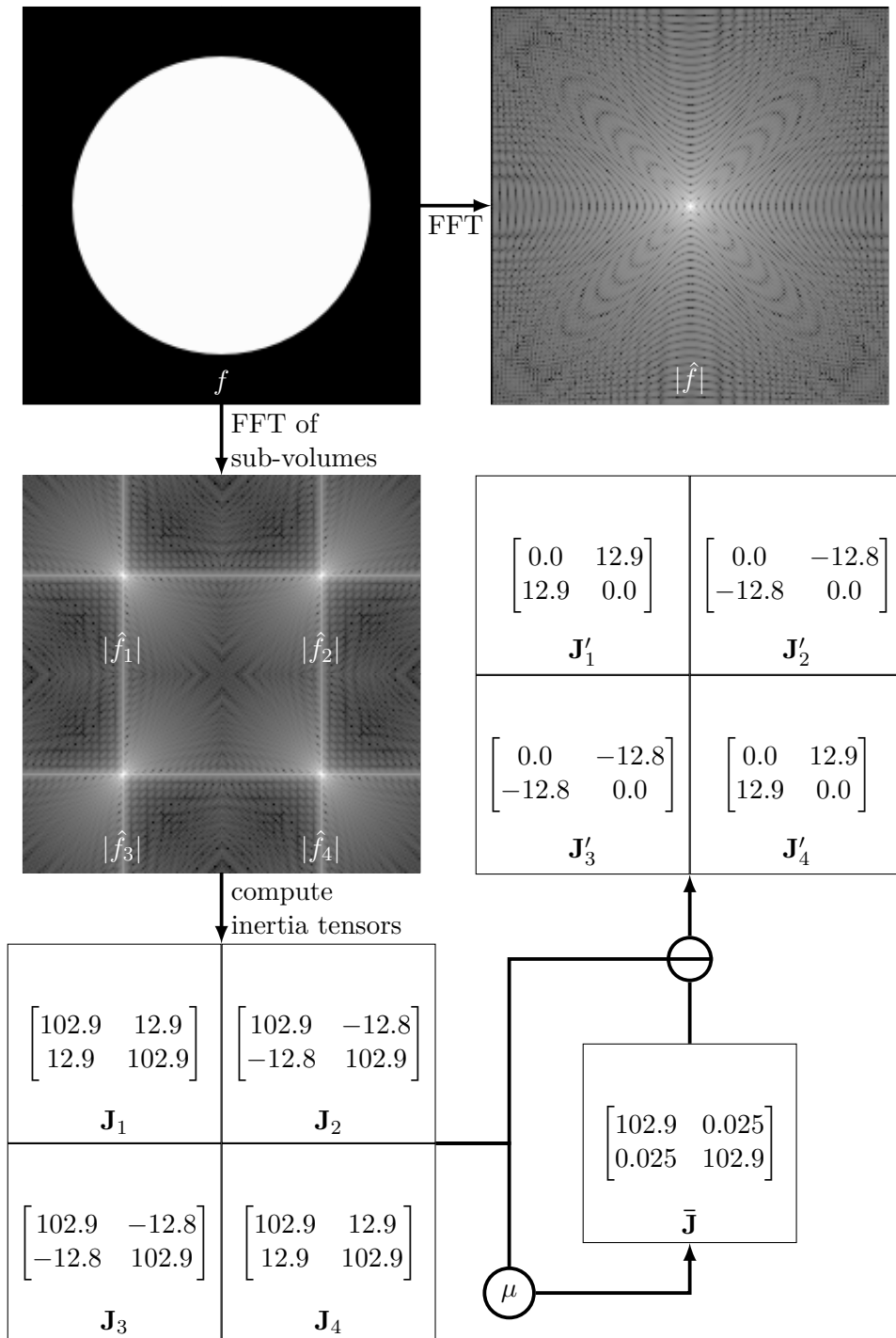


Figure 3.3: Shape classification used of a circle. $\bar{\mathbf{J}}$ and \mathbf{J}'_i are used to compute the shape. The FFT magnitude $|\hat{f}|$ is presented for comparison reasons.

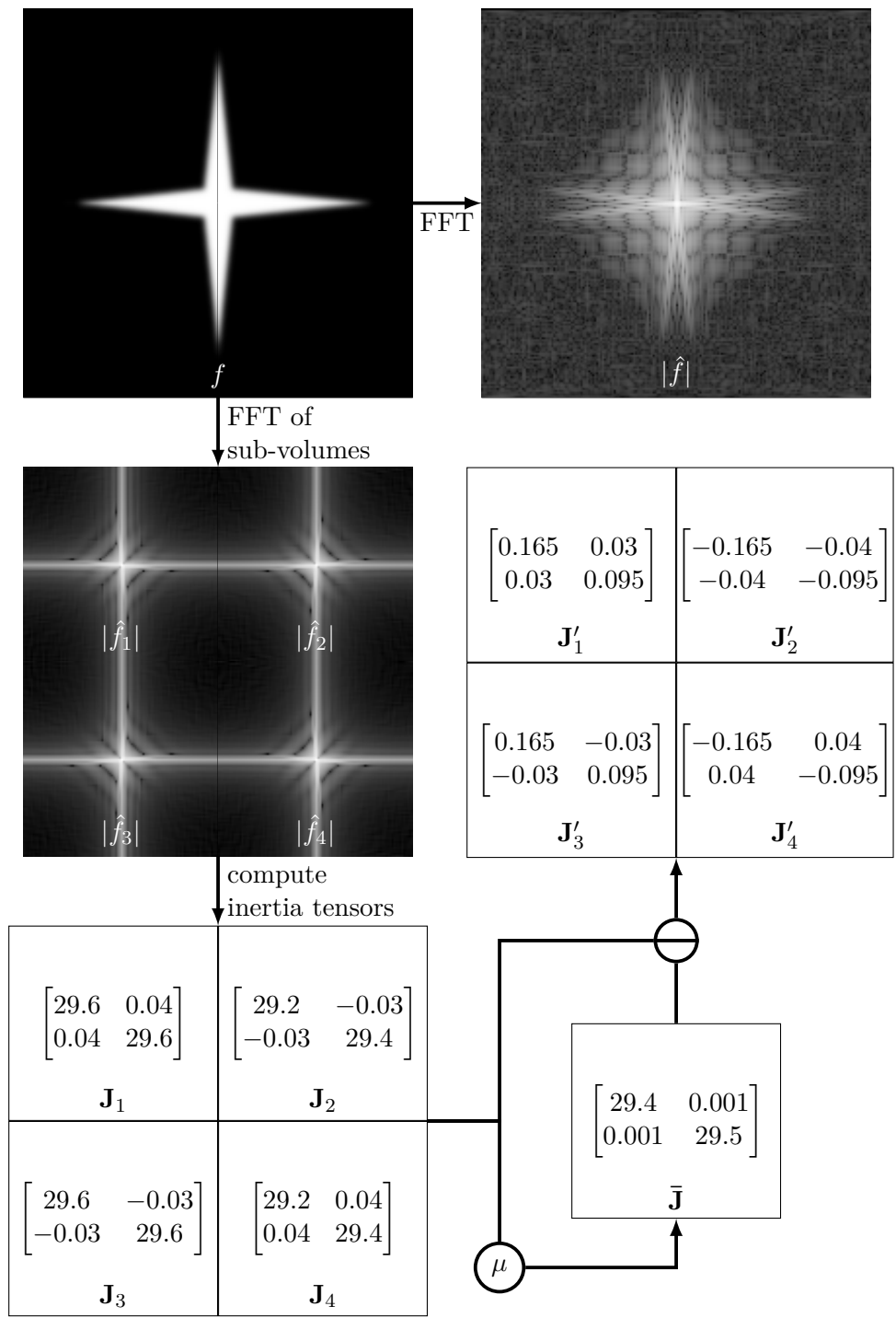
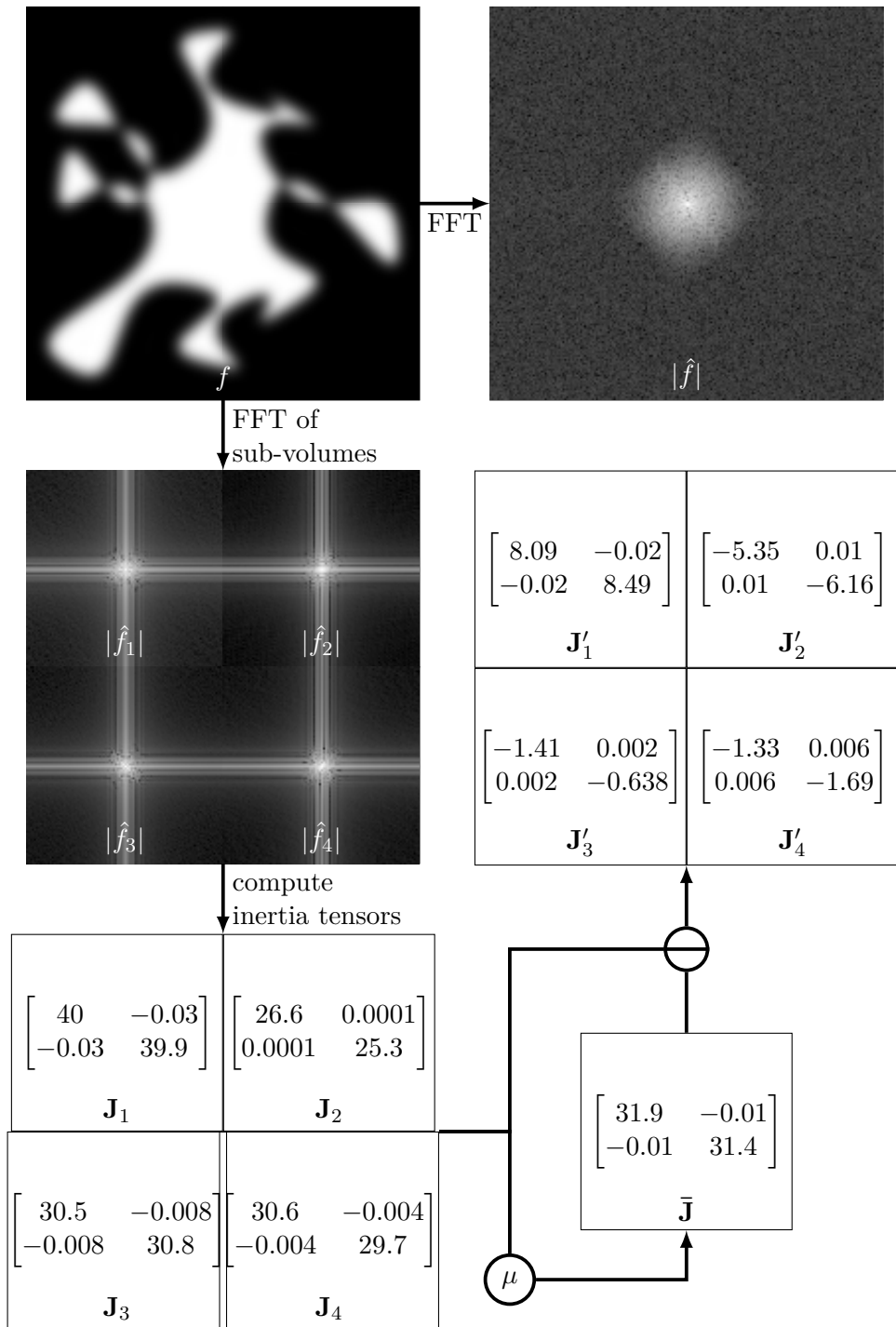


Figure 3.4: Shape classification of a star-shaped object. $\bar{\mathbf{J}}$ and \mathbf{J}'_i are used to compute the shape. The FFT magnitude $|\hat{f}|$ is presented for comparison reasons.



This corresponds with the number of high frequencies in the volume in all three dimensions. Smooth changes in the spatial domain result in a high number of high frequency values compared to blurred changes in the spatial domain. This leads to the assumption that lesions with a smooth boundary have a significant higher amount of high frequencies than lesions with a blurred boundary. Thus, higher *Boundary* values indicate a higher amount of high frequencies within the Fourier magnitude volume, leading to a higher probability of a smooth boundary of a lesion.

Experiments showed that a threshold of 0.16 provides suitable results. The Göttinger score assigns either 0 or 1 point to the boundary. If a lesion shows a smooth boundary ($Boundary > 0.16$), 0 points are assigned. Otherwise, in case of a blurred boundary ($Boundary \leq 0.16$), 1 point is assigned.

Internal Enhancement Characteristics (IEC)

A lesion can be classified according to the IEC. The enhancements of a contrast agent can either be *homogeneous*, *heterogeneous* or *rim-enhanced*. Homogeneous lesions are characterized by having nearly the same contrast agent enhancement throughout the entire lesion. Figure 3.6a shows a synthetically created homogeneous data set. The contrast agent enhancement in heterogeneous lesions is highly irregular. Figure 3.6b shows a heterogeneous lesion, which was created synthetically using Perlin noise. Rim-enhanced lesions are characterized by a contrast agent enhancement at the surface (or hull) of the lesion. This is due to the fact that the cancerous cells already destroyed the interior cells. Since blood is unable to flow there anymore, the contrast agent does not reach these regions. Figure 3.6c shows a synthetically created example of a rim-enhanced lesion. The inner part does not show any enhancement at all. This is the reason why this type of lesions looks similar to rings in the slice view.

In order to determine the type of the IEC, we analyze how the frequencies in the volume data set behave. We subtract the volume of the pre-contrast phase (t_1) from the volume of the late post-contrast (t_3). This results in a volume where the lesion is enhanced and the surrounding tissue is attenuated. Then, the subtracted volume is transformed into the frequency space and, finally, the inertia tensor \mathbf{J} of the transformed volume is computed.

In order to classify the IEC we assume that a more homogeneous distribution of intensity values leads to more spectral energy at high frequencies in the Fourier transformed volume. To evaluate the amount of spectral energy at high frequencies we use the diagonal values of \mathbf{J} , as they increase with the amount of spectral energy at high frequencies, and compute its mean value:

$$IEC = \frac{J_{xx} + J_{yy} + J_{zz}}{3} \quad (3.10)$$

Using the *IEC* value, we need to find a threshold which classifies the IEC into homogeneous, heterogeneous and rim-enhanced. Experiments showed that we can classify lesions as being homogeneous if $IEC \geq 0.1$. Heterogeneous lesions are characterized by $IEC \geq 0.05$ and with $IEC < 0.05$ lesions are classified as rim-enhanced. The Göttinger

score assigns 0 points for the homogeneous, 1 point for the heterogeneous and 2 points for the rim-enhanced IEC.

3.1.4 Kinetic Features

The kinetic features specified by the Göttinger score are the ISI and the PIS. Although a kinetic analysis for the entire lesion is not recommended by various authors [6, 31, 53], we need to provide the ISI and the PIS, because they are required to fulfill the Göttinger score. We compute these features for the entire lesion using the following approximation.

Based on the work of Renz et al. [54], the ISI and PIS is computed for each voxel. The intensity values of the pre-contrast volume, of the volume right after contrast agent injection and of the late post-contrast volume at the same location are evaluated. Given these three intensity values, the kinetic features, based on the 3TP method, are calculated. To compute the ISI, the intensity value of the pre-contrast volume $I(t_1)$ (the first timestamp) and the intensity value of the early post-contrast volume $I(t_2)$ are used. The relative enhancement is computed using these two values with:

$$RE_{ISI} = \frac{I(t_2)}{I(t_1)} - 1.0. \quad (3.11)$$

According to the result of RE_{ISI} , a value for the ISI is chosen based on the Göttinger score [22] (see Table 1.1):

$$ISI = \begin{cases} 0 & \text{if } RE_{ISI} < 0.5 \\ 1 & \text{if } RE_{ISI} < 1.0 \\ 2 & \text{if } RE_{ISI} \geq 1.0 \end{cases}$$

The PIS was evaluated using the intensity values of the volume from the second $I(t_2)$ (the early post-contrast phase) and the third timestamp $I(t_3)$ (the late post-contrast phase). The second relative enhancement RE_{PIS} is computed as:

$$RE_{PIS} = \frac{I(t_3)}{I(t_2)} - 1.0. \quad (3.12)$$

The points assigned to the PIS are again based on the Göttinger score [22] (see Table 1.1):

$$PIS = \begin{cases} 0 & \text{if } RE_{PIS} \geq 0.1(\text{continuous increase}) \\ 1 & \text{if } -0.1 \leq RE_{PIS} < 0.1(\text{plateau}) \\ 2 & \text{if } RE_{PIS} < -0.1(\text{wash-out}) \end{cases}$$

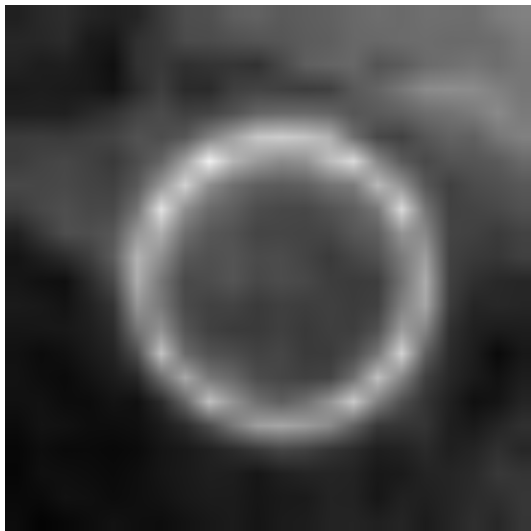
For each voxel, this evaluation is done. Finally, the results are sorted and the kinetic features representing the worst case of the computed voxels is used to represent the whole volume [54].



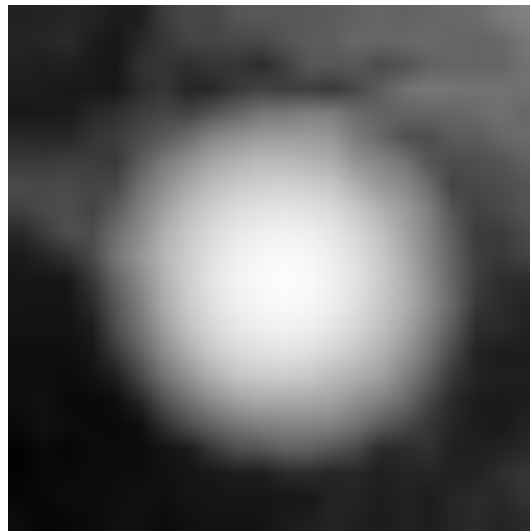
(a) Homogeneous data set



(b) Heterogeneous data set



(c) Rim-enhanced data set



(d) Data set with blurred boundary

Figure 3.6: Phantom data sets with different IEC. **(a)** shows a homogeneous IEC. The contrast agent is the same all over the lesion. **(b)** shows a heterogeneous IEC with the contrast agent being distributed irregularly across the lesion. **(c)** shows a rim-enhanced IEC with its typical ring-like structure. The interior of the lesion is not enhanced at all, while the surface shows strong enhancement. **(d)** shows a synthetic data set containing a sphere with a blurred boundary.

3.2 Feature Visualization

In order to combine the needs of a radiologist, to present a quantitative value that represents a lesion’s probability of being malignant, as well as additional information to see why a certain value was computed, we created several plots. All the features are placed around a center where the quantitative value is presented to make the plot look like a closed system. Another possibility was to create plots, where features are placed side-by-side horizontally or vertically like, e.g., a parallel coordinate system. However, in such a plot it is hard to find something like a central region. As such a place represents the quantitative value, which is the main information, the placement of it is vital. By gathering the features around a center, it is easy to set the focus at the center and the additional (contextual) information around it. This concept provides the radiologist with the quantitative value presenting the probability of the lesion being malignant combined with the features placed around it showing how the overall score is composed of.

3.2.1 Malignancy Area Plot

We employ an adopted star plot, the Malignancy Area Plot (MAP), to visually convey the features of a lesion. The idea behind this graphical representation is to provide the user more than just a single number for lesion classification. With the MAP the user should not only be able to quickly identify whether a lesion is benign or malignant, she or he should also be able to assess the specific features of a lesion.

In order to achieve our goals, we use a radial layout with five axes, each representing a feature of the Göttinger score. Starting from the center of the MAP, we assign the minimum amount of points, zero, to a feature. The outer end of one axis represents the maximum number of points that can be achieved by a certain feature, which is two for the ISI, PIS and IEC and one for the shape and the boundary feature.

Then, the values of the features are connected together. We offer two different types of connections: Linear and cubic ones. In the linear version, where straight lines connect the points, the base shape is a pentagon (Figure 3.7a). A circle builds the base of the cubic connection where the values are connected with cubic interpolation (Figure 3.7b). In order to avoid that a single feature is represented by a single line, if neighboring features are zero, control points are inserted between the features. If all points are connected together, they span an area. The lower the values of the individual features are, the smaller the area becomes. Vice versa, higher values of individual features result in a bigger area. The area spanned by the individual features correlates with the overall Göttinger score and with the lesion’s probability of being malignant. Thus, the area acts as a visual representation in addition to the overall Göttinger score. Because of this we call this area *malignancy area* and thus the plot is named Malignancy Area Plot. Figure 3.7 shows two examples of the MAP. One example is using the linear connection, shown in Figure 3.7a. Figure 3.7b shows the MAP with the cubic connection.

To further improve the visual appearance, we use color filling for the malignancy area: A feature is colored *red*, if its value equals the maximum possible value, it is *white* (the background color) if the feature’s value is the minimum possible one (0) and all the

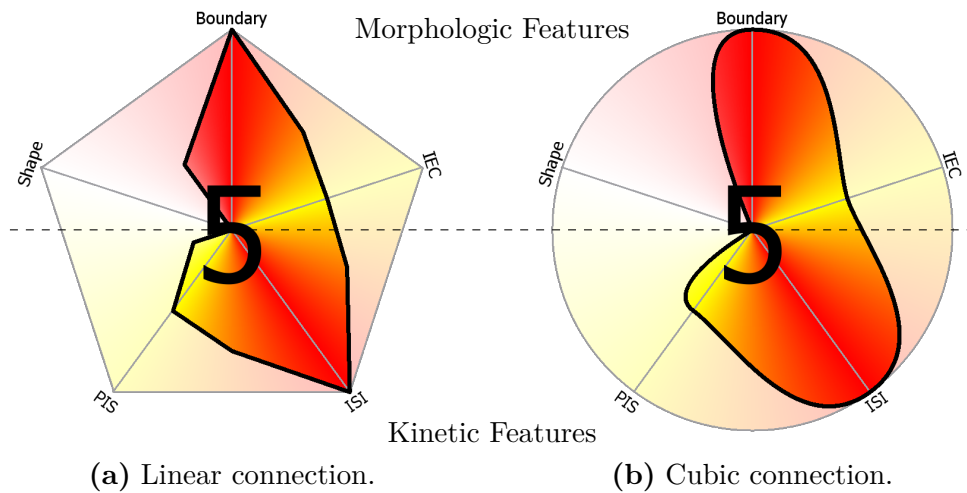


Figure 3.7: Example of the linear (a) and cubic (b) MAP. The morphologic features (shape, boundary and IEC) are positioned on the upper part of the plot. The kinetic features (ISI and PIS) are positioned at the bottom of the plot.

values in between are *yellow*. A conical color interpolation, which interpolates colors around a center point, is used to interpolate the colors between the features. This leads to a highly reddish area if many features exhibit a high value, i.e., the case corresponds to a malignant lesion.

The order of the feature's axes was chosen by us in order to group morphologic and kinetic features together. The shape, boundary and IEC features are placed at the upper half of the plot, while the kinetic features, the ISI and PIS, are placed at the lower half of the plot. Different orderings of the feature axes would result in different plots and thus in different areas. Therefore, a standardized ordering is necessary in order to quickly assess a lesion's characteristics by the shape of its area.

3.2.2 Sunburst Malignancy Area Plot

Another visual representation of the MAP is the sunburst MAP. The main motivation behind this is the visual comparison of multiple data sets within a single plot. We also did not find any usable solution to compare or show multiple data sets in a malignancy area plot. As the comparison of multiple data sets is considered useful by our domain experts we distinguish between the subsequent two types:

- **Inter lesion analysis:** Comparison of different lesions of either a single or multiple patients is evaluated. This might be useful in a statistical analysis for the evaluation in a scientific manner. The number of data sets that can be shown is however limited since a sector needs to have a minimum area in order to recognize a sector's levels.

- **Intra lesion analysis:** Comparison of the same lesion which is scanned and diagnosed several times. This might be useful to monitor a lesion during a neoadjuvant chemo, or endokriner therapy.

The layout of the sunburst MAP is split into sectors. Each feature is placed around the center in the same way the features are placed at the linear and cubic MAP. In the center of the plot, a circle is drawn which contains the overall Göttinger score. Depending on the maximum number of points a feature can get, the sectors are divided into sector levels at certain radii. Thus, features which can get a maximum of one point consist of a sector with a single sector level, while features with a maximum of two points divide the sector on the half-way radius between the inner circle and the outer boundary of the plot into two sector levels. The smaller values are located in the inner part of the plot, while the bigger values are located in the outer sector levels. Then, those sector levels of a feature which are smaller or equal to the number of points of the value are filled. Zero points do not fill a sector level. The maximum number of points fills the whole sector.

The fill color of a sector depends on the score of its feature. White (or no filling) is used when zero points are assigned. Red always represents the maximum number of points. The values between zero and the maximum number of points are interpolated from white to yellow to red. A conical gradient filling interpolates the colors of two neighboring features to reduce an abrupt change in color from one feature to its neighbor and provides smooth visual transitions. Figure 3.8 shows an example of the sunburst MAP.

As already mentioned, one of our main motivations behind this type of plot was the comparison of multiple lesions or different scans of the same lesion. To achieve this goal, a feature sector is divided conically, depending on how many data sets are given. During the development we focused on comparing multiple data sets of the same lesion. We arranged the plot in a way that the data sets are sorted in ascending order and the lower-order ones are placed clock-wise in the feature sector. Examples of multiple data sets visualized in one plot are shown in Figure 3.9.

In contrast to the linear and cubic MAP, the arrangement of the features in the sunburst MAP does not influence the area of the entire sunburst MAP. However, the arrangement of the features should be fixed beforehand to provide a standardized layout and the possibility to compare several plots. Such a standardization is especially useful in medical diagnosis.

3.2.3 Visualization Evaluation

As we provided several different designs of our proposed MAP, we evaluated them in order to determine the preferable choice of our domain experts. The primary goal was to provide a focus and context concept, which gives the radiologist a quick information about the likelihood of the malignancy of a lesion in combination with contextual information on how the score resulted. This visualization should be superior to already existing representations. However, the only representation to the best of our knowledge is a textual representation. In case of the Göttinger score, this is a table that contains all

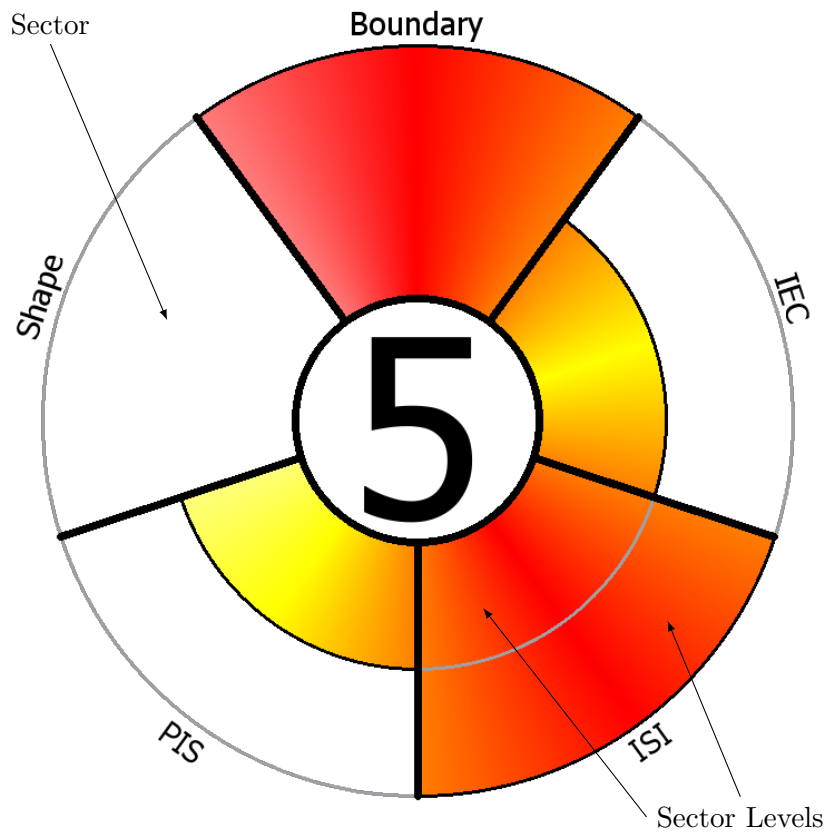


Figure 3.8: The sunburst MAP: Each feature divides the circle into sectors. Depending on the maximum value of a feature, the sectors are divided into sector levels. As shape and boundary can only have 0 or 1, they exhibit only a single sector level, whereas the IEC, ISI and PIS can have 0, 1 and 2 points, which results in two sector levels.

the scores of the single features. There is only one other visualization which is the one provided by Renz et al. [54], which visualizes the MDI as a bar in a colored box.

We used a table showing the Göttinger score as state-of-the-art for comparison. Furthermore, we compared the different designs of our MAP in order to derive the preferred one. To evaluate the visualization we developed an online survey together with two experienced radiologists. For further details regarding the survey, we refer the reader to the appendix where we will present the entire survey to convey what it looked like and what options the participants had. The survey consists of three different parts:

1. **Speed test:** The aim behind the speed test was to see which visualization helped to quickly identify whether a lesion is benign or malignant. This is an important aspect, as a quick response indicates a comprehensible and intuitive visual representation. In order to evaluate whether the shown area of the MAP on its own empowers a user to quickly classify a lesion, the overall Göttinger scores were not shown in our

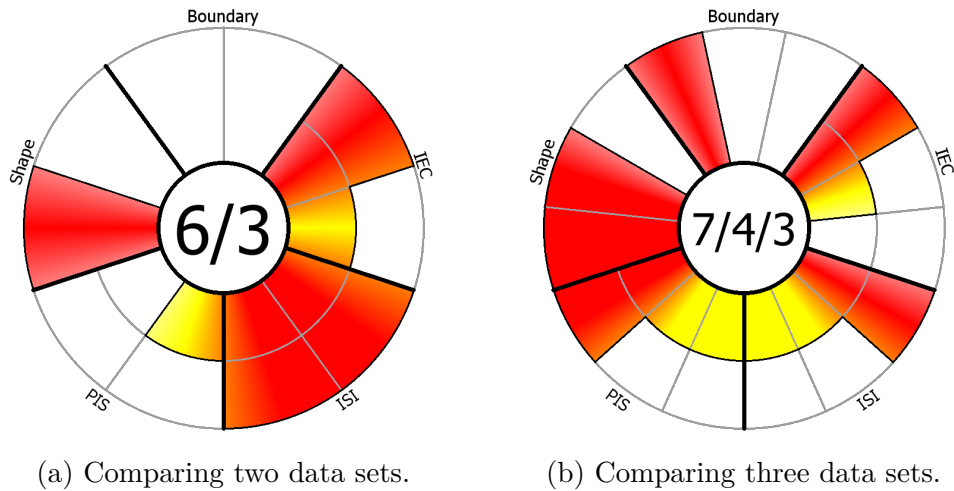


Figure 3.9: Example of the sunburst MAP where multiple data sets are compared. The plot in (a) shows two and the plot in (b) shows three different data sets which were created synthetically. The feature sectors are divided by the number of data sets the plot is showing. The overall Göttinger scores for all data sets are shown as well in the center. They are separated by a slash. The left score belongs to the data set that is shown at the counter-clockwise site of a sector, while the following scores belong to the data sets in clockwise order.

MAPs. The participants had to identify a lesion’s probability of being malignant solely by the shape or filled sectors of the visualization. To compare our MAPs with the tabular representation of the Göttinger score, the latter was shown with the numerical values of the single features. The overall Göttinger score was not shown in the tabular representation. In order to decide whether a shown data set is benign or malignant, we considered overall Göttinger scores < 4 to be benign and scores ≥ 4 to be malignant. Two buttons were provided to make a decision, one for being benign and one for being malignant. The online tool measured and stored the time how long the participant took to make her or his decision, as well as if the decision was made correctly. Each participant had to identify five tabular representations, five linear MAPs, five cubic MAPs and five sunburst MAPs. The order in which the presentations were shown was randomly shuffled, to avoid getting used to repetitive patterns. The selection of the data sets was also randomized.

2. **Style test:** To assess the visual appearance of the visualizations, all of the visualizations, including the tabular representation of the Göttinger score, were shown to the participant. This time, the overall Göttinger score was included. Each representation showed the same data set. The participants had to choose the most visually appealing representations by clicking on them. The order of the representations was again shuffled. A total of eight data sets were shown to the participants.

- 3. Questions:** In order to check whether radiologists are interested in using such visualizations in general, some questions were asked in the survey. Depending on the question, the participant had to choose one of two answers. Four questions were asked regarding the visual representations. Additionally two questions were asked to check whether a visualization of multiple data sets in a single sunburst MAP is intuitive and desired in breast cancer diagnosis.

3.3 Software Prototype

The software prototype, the *Breast DCE-MRI Analyzer*, which was implemented, is presented in Figure 3.10. All the methods and approaches described within this thesis have been implemented in this software prototype. The basic UI consists of the default interface elements of a common medical application, a 3D view (Figure 3.10a), a slice view (Figure 3.10b) and a TF UI (Figure 3.10c). All the loaded volume data sets are shown in the list view on the right side, the volume data UI (Figure 3.10d). Additionally, it is used to start the computation of the features of the Göttinger score. The mask UI (Figure 3.10e) below the volume data UI is used to create and handle masks, that are used for, e.g., creating a ROI.

3.3.1 3D View

The 3D view (Figure 3.10a) is used to show and analyze a volume in the 3D space. By clicking with the left mouse button into the view and holding the mouse button pressed, the volume can be rotated. To decrease the rendering time while the mouse button is pressed, the step size of the ray-casting algorithm is increased. This leads to less sampled images with a lower quality. Releasing the mouse button decreases the step size and the volume is rendered with the initial quality. By moving the mouse wheel it is possible to zoom in or out of the volume. By clicking onto the mouse wheel and moving the mouse, the user can adjust the minimum and maximum intensity thresholds for the rendering. Moving along the negative X axis reduces the maximum intensity value while moving along the positive X axis increases it. Keeping the mouse wheel pressed and moving the mouse along the positive Y axis decreases the minimum intensity value, moving along the negative Y axis increases it. Right clicking into the view opens a context menu. With this context menu it is possible to change some rendering options and it is possible to reset the minimum and maximum intensity thresholds. On the one hand it is possible to change the compositing method used for ray casting. The user can change between averaging (or pseudo X-ray), MIP, Minimum Intensity projection (MinIP) or DVR. The user can select pre-defined viewing directions: sagittal, coronal and transversal. It is also possible to select the projection type, perspective projection as well as orthographic projection.

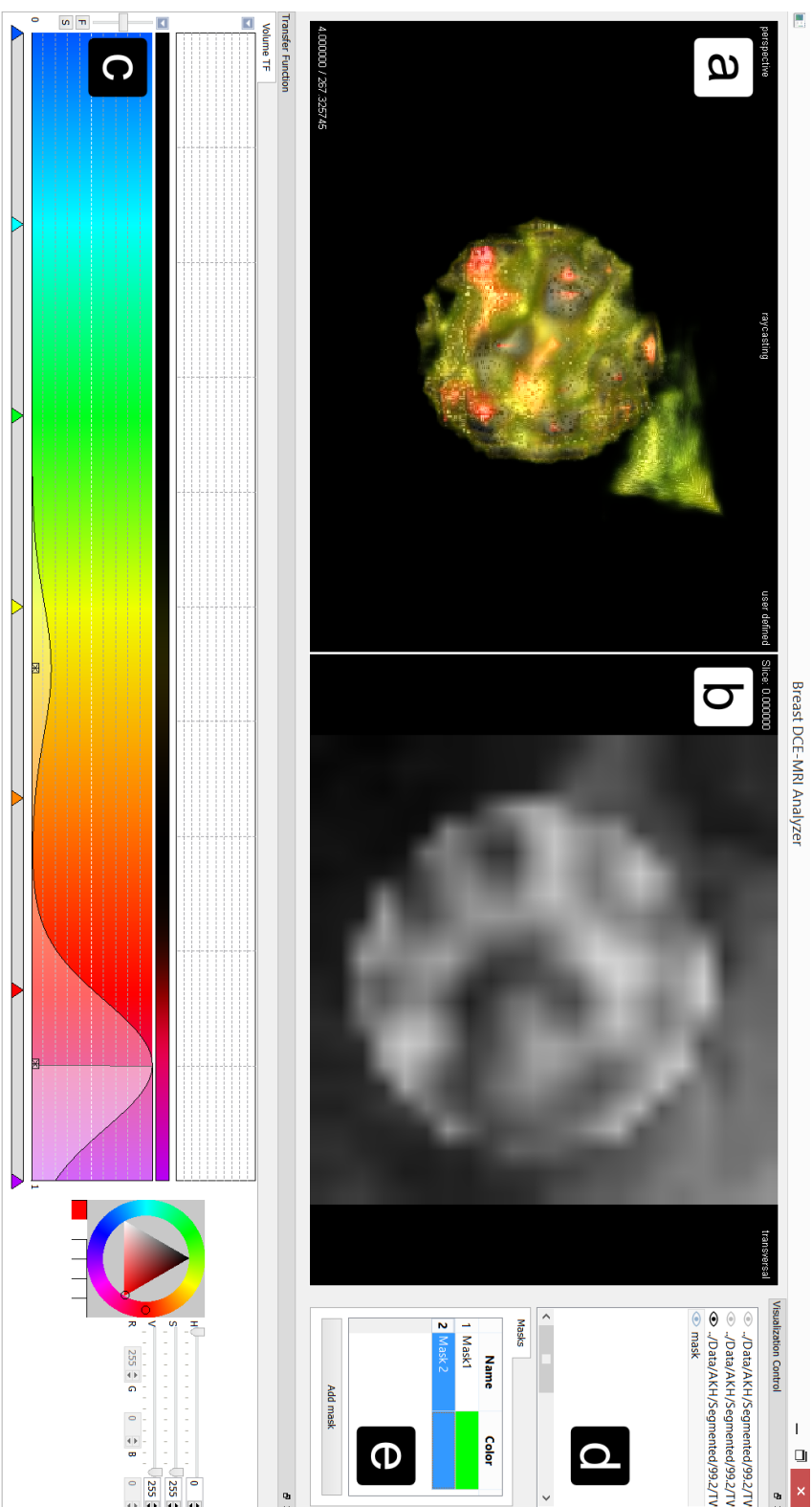


Figure 3.10: A screenshot of our software prototype, the *Breast DCE-MRI Analyzer*. (a) shows the 3D view, (b) shows the slice view. (c) shows the TF UI. (d) shows the volume data UI and (e) the mask UI.

3.3.2 Slice View

The slice view (Figure 3.10b) renders the slices of the volume. It is possible to set the slice direction, which can be *sagittal*, *coronal* and *transversal*. Per default the slice view renders the volume in the *transversal* direction. By pressing the *X*, *Y*, *Z* keys on the keyboard the user can switch between the directions. By rotating the mouse wheel, the user can set the slice position. This is also possible by clicking and holding the mouse wheel and moving the mouse.

The key feature of the slice view is the selection of a ROI, which is possible if a masking volume is available and a mask is created. Clicking the right mouse button opens a context menu, in order to choose one of three masking methods. The first masking method is the single voxel selection. The user chooses single voxels to define the ROI, which are typically the outer bounds of it. Another method is using a cuboid selection. With this method the user can choose a voxel and grow a cuboid by keeping the mouse button pressed and moving the mouse. The last voxel selection method is the spherical selection. Like the cuboid voxel selection, the user needs to select a voxel, keep the mouse button pressed and by moving the mouse, all voxels inside the sphere are selected. During the selection process all the selected voxels are also visible in the 3D view. The selected voxels represent the ROI which will result in creating a new sub-volume.

3.3.3 Transfer Function (TF) UI

Figure 3.10c shows the TF element. A TF maps a voxel's intensity value (*X* axis) to a specified color. The *X* axis ranges from an intensity value of 0.0 to 1.0, as the volumetric data sets are normalized. The *Y* axis is used to specify the opacity. The *Y* axis ranges from fully transparent (0.0) to fully opaque (1.0).

The transfer function is used to change the appearance of the volumetric rendering. The transfer function can be adjusted by clicking on the color band. Left clicking creates a mapping, whereas right clicking (swiping over) deletes the mapping. The user can specify the colors that are used for certain intensity values below the color band. Clicking with the left mouse button inserts a new color or an already created color can be changed. Right clicking onto a color point deletes the color value. The gaps between the user-specified colors are linearly interpolated and displayed in the color band.

3.3.4 Volume Data UI

The volume data UI (Figure 3.10d) widget is built up with a list that contains all opened volumes. By double clicking onto a volume its visibility can be toggled. Right clicking into the list of volumes opens a context menu for opening or saving volumes, creating mask volumes or applying different tasks to a selected volume. The most important feature is to start the lesion inspection method. To do this three volumes (because of the 3TP method) have to be selected. After the volumes are selected and the right mouse button is pressed, the user simply needs to press the *Do classification*. After some computation time a new window with the star plot visualization opens.

3.3.5 Mask UI

Figure 3.10e shows the masking UI. It is used to create, delete and adjust masks. Each mask makes it possible to mark several different parts in a volume while just using one mask volume. A different color can be assigned to each mask. A ROI is created using a single selected mask in combination with the volume selected in the volume data UI (Figure 3.10d).

Results and Discussion

In this chapter, we present results of our proposed approach as well as an evaluation. First, all data sets that were provided by our collaborating domain experts are processed and their results described and explained. We describe lesions with special characteristics or misclassifications in more detail. The last part of this chapter gives an overall evaluation of our approach.

To test our implemented methods, 22 lesions of 12 patients were analyzed. From these 22 lesions, eight are proven to be benign. The remaining 14 lesions are proven to be malignant. The lesions were scanned using a Siemens Magnetom[®] TrioTim system with a 3T magnetic field. The contrast agent for the DCE-MRI scan was a Dotarem[®] (gadoterate maglumine) or MultiHance[®] (gadobenate dimeglumine) injection. A time series with eleven timestamps was acquired using T1-weighted MRI. Additionally, but not used for our method, at each timestamp a fat suppressed data set was created as well.

In the Appendix A we present for every data set a set of figures of the breast and the lesion as well as the visual representations generated with our method for the resulting Göttinger score. The presented figures are the same for each data set to make them comparable. The results will be labeled with the notation $A.B$, where B specifies the lesion of patient A . For each lesion, a transversal MIP of the patient's whole data set at the late post-contrast phase will be shown, which gives an overview of the size and the location of the lesion. Then a MIP of the lesion in transversal direction is presented to show the lesion in more detail. We also provide a transversal slice of the lesion in order to show the inner structure of the lesion. The features calculated with our semi-automatic approach are presented with our novel visualizations, the linear Malignancy Area Plot (MAP), the cubic MAP and the sunburst MAP. The lesions of the patients 01 to 09 are proven malignant lesions. Those from the patients 10 to 12 are benign.

For each data set, the reference classification was performed manually by an experienced radiologist in breast cancer diagnosis. Table 4.1 provides an overview of all the features of the Göttinger score in pairs comparing the domain expert's results with our automatically computed results. The first value is the domain expert's result, whereas

Table 4.1: Manually classified features of the Göttinger score (first number), given by a domain expert, compared to the automatically computed ones (second number) using our method. Beside the morphologic features (shape, boundary and IEC) and the kinetic features (ISI and PIS), the overall Göttinger score is also shown. For comparison reasons, the last column indicates the difference of the overall Göttinger score between the manual and the automatic classification and the accumulated difference of the morphologic features in brackets.

Lesion	Shape	Boun.	IEC	ISI	PIS	Score	Diff.
01.1	1/1	1/1	1/1	2/2	0/2	5/7	2(0)
02.1	1/1	1/1	2/2	2/2	2/2	8/8	0(0)
03.1	1/1	1/1	0/1	2/2	0/0	4/5	1(1)
03.2	1/1	1/0	0/0	2/2	1/0	5/3	2(1)
03.3	1/1	1/1	0/0	2/2	1/0	5/4	1(0)
04.1	1/1	1/1	1/1	2/2	2/1	7/6	1(0)
05.1	1/1	1/1	1/1	2/2	2/2	7/7	0(0)
05.2	1/1	1/1	2/2	2/2	2/2	8/8	0(0)
05.3	1/1	1/1	1/1	1/2	2/2	6/7	1(0)
05.4	1/1	1/1	1/2	1/2	2/2	6/8	2(1)
06.1	1/0	1/1	1/2	2/2	2/2	7/7	0(2)
07.1	0/0	1/1	1/1	2/0	2/0	6/2	4(0)
08.1	1/1	1/0	2/1	2/2	1/0	7/4	3(2)
09.1	0/1	1/1	1/1	2/2	2/2	6/7	1(1)
10.1	0/0	1/0	1/1	2/2	0/1	4/4	0(1)
10.2	0/1	0/1	1/1	2/2	0/2	3/7	4(2)
10.3	0/0	0/0	0/0	2/2	1/2	3/4	1(0)
10.4	1/0	1/1	1/1	2/2	0/0	5/4	1(1)
11.1	1/1	1/1	1/2	0/0	0/1	3/5	2(1)
11.2	0/0	0/0	0/0	2/2	0/0	2/2	0(0)
12.1	0/0	0/0	1/1	2/2	0/1	3/4	1(0)
12.2	0/1	0/0	1/1	2/2	0/1	3/5	2(1)

the second value is the computed result. Each of these pairs is separated by a slash (“/”). The last column in Table 4.1 shows the difference of the overall Göttinger score of the domain expert’s results compared to the overall Göttinger score which was computed with our method. The value in brackets in the same column shows the accumulated difference of the morphologic features. In the following we analyze the results of our computed features compared to the domain expert’s results.

4.1 Feature Computation Evaluation

In order to evaluate the accuracy of the implemented method we compare the classification results of the radiologist with the ones obtained with our approach. Table 4.2 shows the raw values computed by our approach which were then used for the classification of the features of the Göttinger score. The first column specifies the data set, the second one shows the computed features for the shape, i.e., the quantitative value for the sphere-like feature of the mean inertia tensor and a boolean value which specifies whether the sub-volumes have planar structure or not. The third column presents the value used to classify the boundary and the last column presents the value for classifying the IEC. For each feature we calculated the accuracy, the specificity and the sensitivity. Finally, we also determined the overall accuracy, specificity and sensitivity. Subsequently, we provide a statistical evaluation of the following features:

- **Shape** The Fourier-based method for computing the shape correctly classified 17 of 22 lesions with a sensitivity of 0.857, a specificity of 0.625 and an accuracy of 0.773. We did not evaluate these results using synthetic data sets.
- **Boundary** The Fourier-based method for computing the boundary correctly classified 18 of 22 lesions. This leads to a sensitivity of 0.824, a specificity of 0.800 and an accuracy of 0.818. In addition to the values shown in the third column in Table 4.2, the synthetic data set simulating a smooth boundary (Figure 3.6a) scored a value of 0.245 which classifies it to being smooth. The synthetic data set with the blurred boundary (Figure 3.6d) scored a value of 0.085 classifying it to being blurred. Thus, all synthetic data sets were classified correctly.
- **IEC** The Fourier based method for computing the IEC correctly classified 17 out of 22 lesions. The remaining five lesions were classified with a score difference of one. There is no occurrence where a homogeneous lesion was classified as rim-enhanced or vice versa. The computation has a sensitivity of 0.875, a specificity of 0.896 and an accuracy of 0.886. In addition to the values shown in Table 4.2 we also checked the method against a synthetic data set. The data set simulating a homogeneous lesion (Figure 3.6a) scored a value of 0.147 classifying it as homogeneous. The heterogeneous one (Figure 3.6b) scored a value of 0.081 classifying it as heterogeneous. Finally, the rim-enhanced data set (Figure 3.6c) scored a value of 0.047 classifying it as rim-enhanced. So all of the synthetic data sets were classified correctly.

Table 4.2: The values computed for the morphologic feature classification using our Fourier-based approach. The first column shows the lesion. The second one the numeric and binary values used to classify the shape feature. The third column shows the values which are used to classify the boundary feature. The fourth column shows the values used to classify the IEC feature.

Lesion	Shape	Boun.	IEC
01.1	0.618 / true	0.086	0.051
02.1	0.679 / false	0.057	0.034
03.1	0.678 / false	0.134	0.088
03.2	0.868 / false	0.197	0.128
03.3	0.801 / false	0.153	0.101
04.1	0.752 / false	0.108	0.063
05.1	0.675 / false	0.139	0.082
05.2	0.656 / false	0.067	0.030
05.3	0.814 / false	0.123	0.067
05.4	0.737 / false	0.080	0.045
06.1	0.826 / true	0.054	0.021
07.1	0.687 / true	0.156	0.057
08.1	0.835 / false	0.175	0.071
09.1	0.813 / false	0.130	0.056
10.1	0.810 / true	0.188	0.084
10.2	0.803 / false	0.139	0.083
10.3	0.789 / true	0.290	0.122
10.4	0.836 / true	0.151	0.086
11.1	0.824 / false	0.062	0.037
11.2	0.776 / true	0.263	0.163
12.1	0.760 / true	0.169	0.098
12.2	0.735 / false	0.167	0.064

To compute the overall sensitivity, specificity and accuracy we assume that an overall Göttinger score < 4 is considered as being benign, while a Göttinger score ≥ 4 is considered being malignant which are common thresholds used by other authors. The overall sensitivity is 0.875, the specificity 0.167 and the accuracy 0.682.

We also computed the overall sensitivity, specificity and accuracy just for the morphologic features. We assumed an overall score of < 2 as being benign and an overall score of ≥ 2 as being malignant. This leads to an overall sensitivity of 0.929, a specificity of 0.5 and an accuracy of 0.772.

Figure 4.1 shows the performance of the algorithm. On average the algorithm needed 12.2 μs per voxel with a standard deviation of 12.1 μs per voxel to compute the features on a computer with an Intel Core i7 860 CPU (2.80 GHz) and 8 GB of RAM. As shown in the figure, the time the algorithm needs to compute the Göttinger score depends linearly on the number of voxels of the ROI that is computed.

4.1.1 Discussion

The results show that the presented method to compute the morphologic features defined by the Göttinger score with the Fourier-based approach coincides to the radiologists defined features up to a high degree. As indicated by the right-most column of Table 4.1 our approach computes the same morphologic Göttinger scores in eleven out of 22 cases, compared to the radiologist's classification. In eight cases the difference is one and in three cases the difference is two.

A major misclassification was done in case 07.1 (Figure A.12), but according to Table 4.1 this is due to the kinetic features which differ by four from the radiologist's classification. This is especially important because a malignant lesion was classified as being benign.

Another misclassification occurred in lesion 08.1 (Figure A.13) which differs by three in the overall Göttinger score and by two by the morphologic features compared to the radiologist's classification. In this case however, the lesion was classified as being malignant, as it was defined by the radiologist. The MIP of lesion 08.1 (Figure A.13b) as well as the slice (Figure A.13c) makes it plausible to classify the boundary as being smooth and the IEC as being heterogeneous as it was done by the automatic approach.

Misclassified was also the lesion 10.2 (Figure A.16), which differs by four from the radiologist's classification. Despite a round/oval shape with smooth boundary the automatic approach classified the shape being irregular and the boundary being blurred. Additionally the kinetics differ also by two which results in the very high difference of four. Further analysis together with a radiologist is necessary to evaluate the validity of this result.

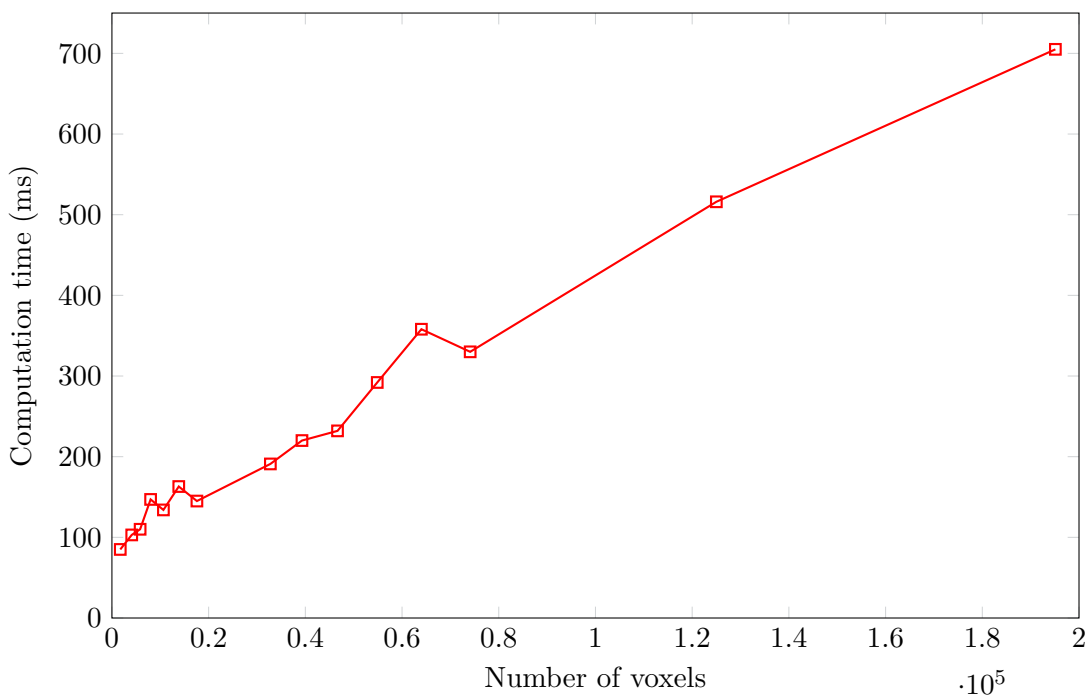


Figure 4.1: Performance of the feature computation. The plot shows the time used to compute the Göttinger score with respect to the number of voxels on an Intel Core i7 860 CPU (2.80 GHz) with 8 GB RAM.

4.2 Visualization Evaluation

In order to evaluate our proposed visualizations we prepared an online survey as described in the previous chapter. We asked radiologists to participate in this survey in order to assess the need of providing a visual representation for breast cancer diagnosis. A total of five radiologists participated in this survey. The results are presented in the following.

4.2.1 Speed Test

The first test in the survey was a speed test. With this test we wanted to check whether it is possible to quickly assess a lesion’s probability of malignancy solely by looking at its representation to draw conclusions to the quality of the MAP.

Table 4.3 shows the accuracy and the average time the radiologists needed to classify the data sets based on the shown representation. The results are shown for all data sets, as well as for the malignant and benign data sets separately.

The first part of Table 4.3 shows the result of the cubic MAP representation. It took a radiologist 4.43 s on average to make a decision with an accuracy of 0.92. Malignant data sets were classified in 4.23 s whereas it took 4.84 s to decide whether it was a benign data set. The malignant data sets were classified with an accuracy of 0.94, the benign data sets were classified correctly with an accuracy of 0.88.

Table 4.3: The results of the speed test of our various Göttinger score representations. The accuracy and average speed was evaluated for all data sets as well as for benign and malignant data sets separately. The results are grouped, based on their visual representation.

Plot	Lesion	# Samples	Accuracy	Avg. Speed (s)
Cubic MAP	All	25	0.92	4.43
	Malignant	17	0.94	4.23
	Benign	8	0.88	4.84
Linear MAP	All	25	0.92	4.32
	Malignant	17	0.94	5.09
	Benign	8	0.88	2.68
Sunburst MAP	All	25	0.96	3.75
	Malignant	17	1.00	3.54
	Benign	8	0.88	4.19
Table	All	25	1.00	3.29
	Malignant	17	1.00	3.66
	Benign	8	1.00	2.50

The second row in Table 4.3 shows the result of the linear MAP representation. It took a radiologist 4.32 s on average to decide with an accuracy of 0.92. Malignant data sets were classified in 5.09 s whereas benign ones in 2.68 s. The malignant data sets were classified with an accuracy of 0.94, the benign data sets with an accuracy of 0.88.

The third row in Table 4.3 shows the result of the sunburst MAP. It took a radiologist 3.75 s on average to decide with an accuracy of 0.96. Malignant data sets were classified in 3.54 s whereas benign ones in 4.19 s. The malignant data sets were classified with an accuracy of 1.00, the benign data sets with an accuracy of 0.88.

The last row in Table 4.3 shows the result of the tabular representation. It took a radiologist 3.29 s on average to decide with an accuracy of 1.00. Malignant data sets were classified in 3.66 s whereas benign ones in 2.50 s. The malignant data sets were classified with an accuracy of 1.00, the benign data sets with an accuracy of 1.00.

4.2.2 Style Test

In order to check which of the presented plots appeal to the radiologists the most, we showed them all the different plots of the same data set at once. Then, the radiologists had to choose the plot which they liked best by clicking on it. Figure 4.2 shows the results of the five radiologists where each radiologist chose his favorite representation in each of eight data sets. The sunburst MAP was chosen as the best representation of the Göttinger score. The radiologists chose it in 73% of the shown data sets as their preferred

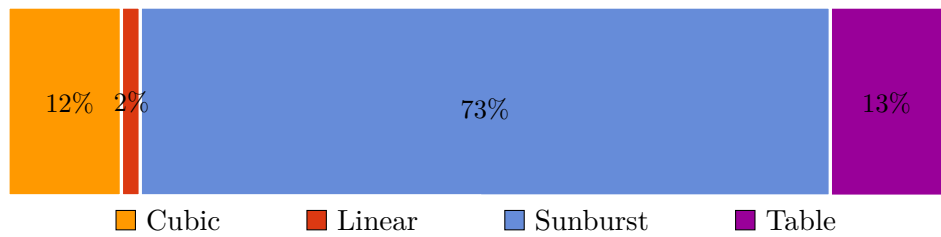


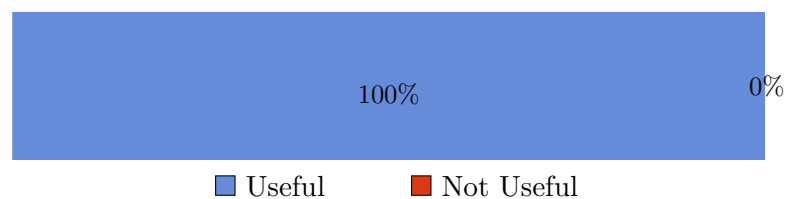
Figure 4.2: The results of the style test shown in a bar chart. The sunburst MAP was chosen as the best representation of the Göttinger score. The cubic MAP as well as the tabular representation are similar representative. The linear MAP did only satisfy the radiologists in 2% of the data sets.

visual representation. The tabular representation, as well as the cubic Malignancy Area Plot (MAP), did satisfy the radiologists in 13% and 12% of the data sets respectively. The linear MAP was chosen in 2% of the shown data sets as the favorite representation. This result shows that there is the wish of the radiologists to provide a visual representation for breast cancer diagnosis.

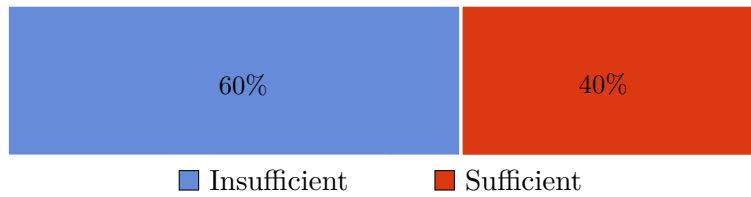
4.2.3 Questions

Finally the radiologists had to answer some questions with one of two answer possibilities. In the following we are showing the results of the questions.

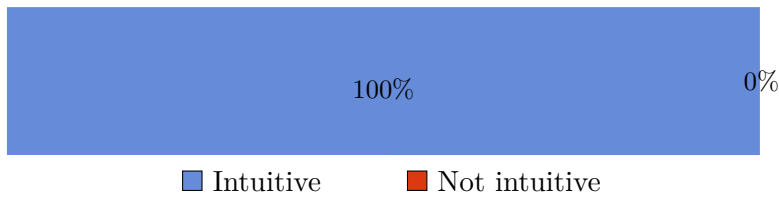
The visual representation of the Göttinger score is ... Participants had to choose whether the visual representation of the Göttinger score is *useful* or *not useful*. All radiologists answered that a visual representation of the Göttinger score is useful.



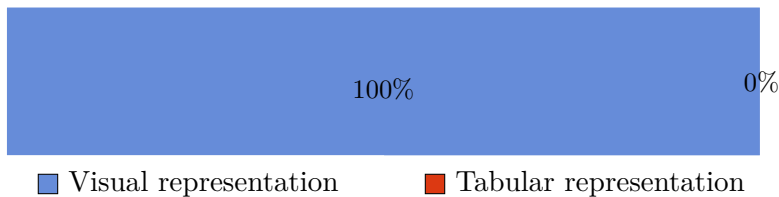
The overall score of the Goettinger score on its own would be ... Participants had to choose whether the overall Göttinger score on its own would be *sufficient* or *insufficient*. Three out of five radiologists answered that the overall Göttinger score on its own is insufficient for breast cancer diagnosis. This shows that a single quantitative value alone is not enough. Contextual information is also vital to assess a lesion's possibility of being malignant.



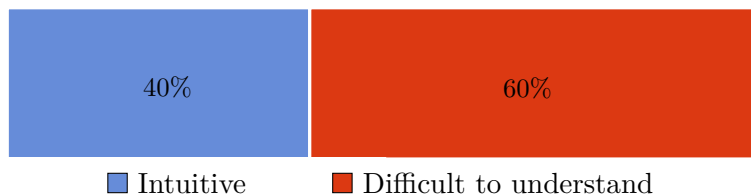
The details in the visualizations presented are ... Participants had to choose whether the detail in the visualizations presented are *intuitive* or *not intuitive*. All the radiologists answered that the presented details in the visualizations are intuitive.



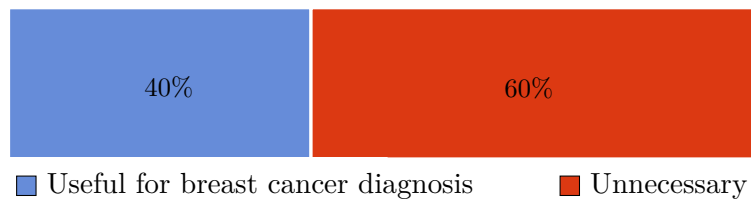
For breast cancer diagnosis I would prefer to use ... Participants had to choose whether they would use a *tabular* or a *visual representation* for breast cancer diagnosis. All radiologists answered that they would prefer to use the visual representation.



Such a visual comparison of multiple data sets is ... For this question two images of sunburst MAPs where one contained two data sets and the second one contained three data sets, were shown to the user (see Figure 3.9). Participants had to choose whether such a visual comparison of multiple data sets is *intuitive* or *difficult to understand*. Three out of five radiologists answered that such a visual comparison of multiple data sets is difficult to understand.



Such a visual comparison of multiple data sets is ... For this question two images of sunburst MAPs where one contained two data sets and the second one contained three data sets, were shown to the user (see Figure 3.9). Participants had to choose whether such a visual comparison of multiple data sets is *useful for breast cancer diagnosis* or *unnecessary*. Three out of five radiologist answered that such a visual comparison of multiple data sets is unnecessary.



4.2.4 Discussion

The results obtained from the survey shows that a visual representation is certainly desired by the radiologists. The speed test showed that, among the visual representations of the Göttinger score, the radiologists did the classification task the fastest and the most accurate with the sunburst MAP. However, none of the visual representations surpassed the speed and the accuracy of the tabular representation. But we also need to notice, that with the tabular representation it was easy to do the classification task, because participants simply had to sum up the values, which is not that easy using the visual representations. However, the results of the style test shows that the participating radiologists liked the sunburst MAP as representation for the Göttinger score the most. The questions asked, also show that the visual representations are designed to be understood easily, and that the contextual information is of course wanted by the radiologists. Despite the excellent result of the table, none of the participants would prefer the tabular representation over a graphical representation. This lets us assume that the acceptance rate for such a visual representation among radiologists is high.

The final questions regarding the presentation of multiple data sets in a sunburst MAP showed two aspects: First, the presentation of the data is too complicated and more work has to be done to create a proper solution. But the two questions regarding multiple data sets in the sunburst MAP also showed, that the majority of the radiologists is skeptic whether such a presentation is useful. Working towards a better representation should be considered carefully if there is already such a high skepticism because there might not be an acceptance for such a plot.

Conclusion and Future Work

This chapter summarizes the work of this thesis. First, a short summary recaps the methods of our work combined with the ideas and the aims we achieved. Then, the results are concluded and problems are mentioned. The summary is followed by an outlook on future work. The problems motivate future directions and further ideas for improvements are presented.

5.1 Conclusion

During this work a software prototype, the *Breast DCE-MRI Analyzer*, was created with a semi-automatic method for analyzing breast lesions. This method takes volumes of a lesion at different timestamps as input and computes morphologic and kinetic features that are used for state-of-the-art breast cancer analysis based on the Göttinger score. The morphologic features are the shape, the boundary and the Internal Enhancement Characteristics (IEC), the kinetic ones are the Initial Signal Increase (ISI) and the Post Initial Signal (PIS). For the computation of the kinetic features, we employed the well-established 3TP method by Degani et al. [16]. Motivated by the goal to avoid segmentation and to simplify the user input, we focused on using the Fourier transform in combination with defining a ROI to compute morphologic features. This is a major advantage over other methods that need a segmentation as segmentation is a process known for being time consuming and prone to errors. Defining a ROI, however, is a well-known established interaction in medical imaging.

The results of the computed features are presented in novel, normalized, visualizations, called Malignancy Area Plot (MAP). In order to evaluate a proper visual representations we created three different kinds of the MAP: the linear one, based on a pentagon, a cubic one based on a circle and a the sunburst MAP. Basically, the MAPs show the features in a compact way to provide a quick overview of the lesion's likelihood of malignancy in combination with its characteristics. The area that is spanned by the features' values

in the plot increases with the likelihood of the lesion's malignancy. Additionally color coding emphasizes a single feature as well as the whole visualization. The shape of the area is meant to give a visual indication of the lesion's characteristics which can be used to quickly identify the type of lesion. The fact that the MAP is normalized helps to compare lesions across different studies.

An evaluation based on an online survey showed that radiologists would prefer a visual representation over a tabular one. Especially the sunburst MAP satisfied the radiologists. Compared to the cubic and linear MAP, the sunburst MAP empowered the radiologists to make the most accurate and fastest decisions for whether the area shows a malignant or benign Göttinger score.

Comparing the results of our morphologic feature computation with the features created by a domain expert, we observed an accuracy of 0.864 for the shape and the boundary and an accuracy of 0.886 for the IEC. Even though the results are not exactly the same in some of the tested cases, there is a high accordance with the domain expert's results. Only in a few cases we observed major misclassifications, which could be traced back to the composition of the lesion in the volume. As already mentioned, the computation of the kinetic features was not the focus of this work.

We also observed, that if results of the lesions are combined with each other, the developed method delivers reproducible and stable results which means that similar looking lesions have similar results. Moreover, we achieve a high conformance with the radiologist's results. How the surrounding volume of the lesion affects the results was not analyzed during this work.

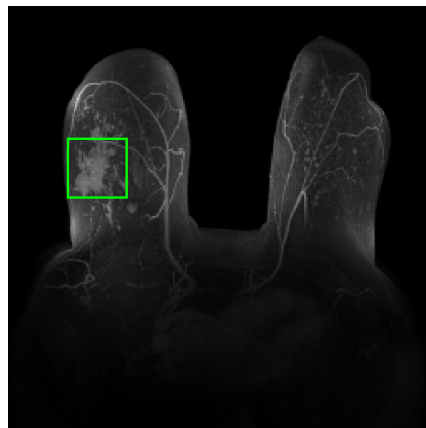
5.2 Future Work

Further evaluation on a data base with many more data sets is recommended. A training data set in combination with an algorithm (e.g., neural networks) should be applied to determine the optimum threshold values for differentiating the morphologic features (shape, boundary and IEC). An export function that creates a DICOM file out of the resulting visualization should be provided to produce a result that can be stored in a clinically CAD environment. So far only a few of the Fourier information is used to compute morphologic features. Additional information of the Fourier phase needs to be investigated and evaluated whether it can also be used for improving the feature computation.

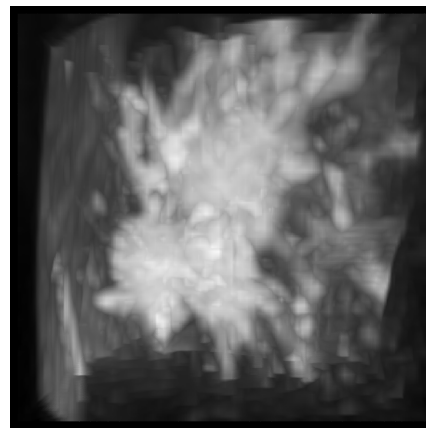
APPENDIX **A**

Results

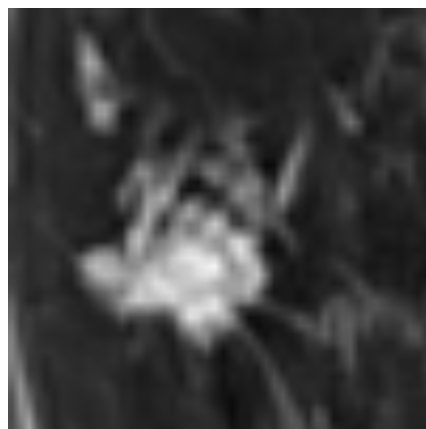
Subsequently we present for every analyzed patient a set of visualizations of the breast and the lesion as well as the visual representations generated for their resulting Göttinger score. These visualizations are the same for each data set to make them comparable.



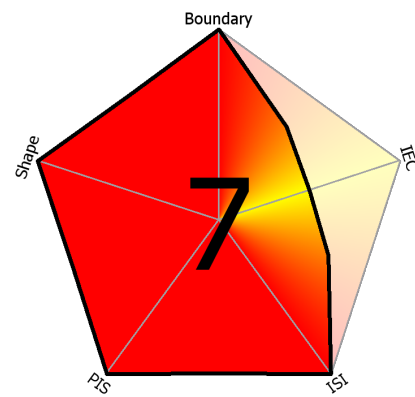
(a) MIP of the entire data set



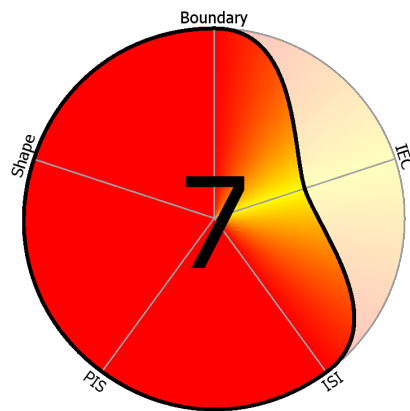
(b) MIP of the lesion



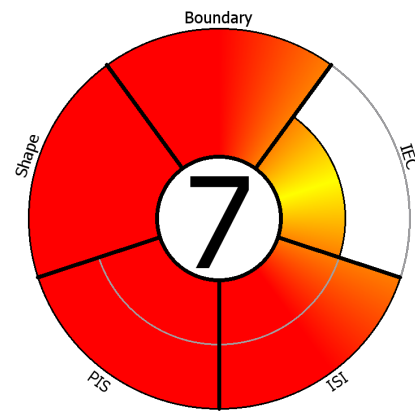
(c) Slice of the lesion



(d) Linear MAP

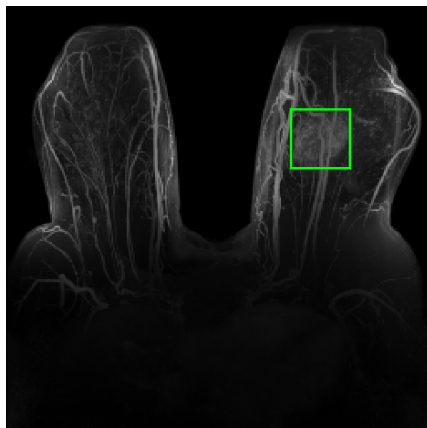


(e) Cubic MAP

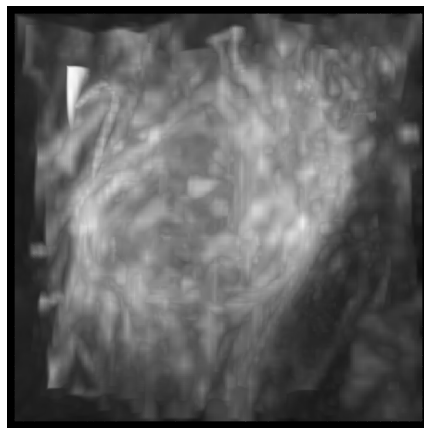


(f) Sunburst MAP

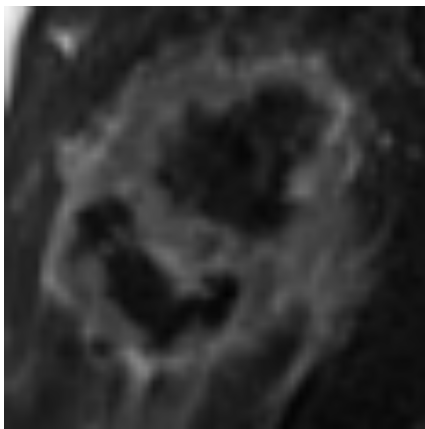
Figure A.1: Lesion 01.1. **(a)** Transversal MIP of the entire data set. **(b)** Lesion at early post-contrast phase. **(c)** Slice of the lesion. Finally, the representations of the Göttinger score visualized by the linear MAP **(d)**, the cubic MAP **(e)** and the sunburst MAP **(f)**.



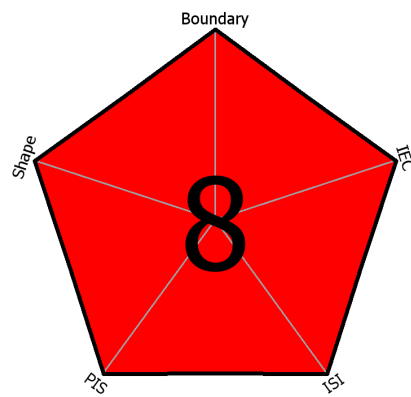
(a) MIP of the entire data set



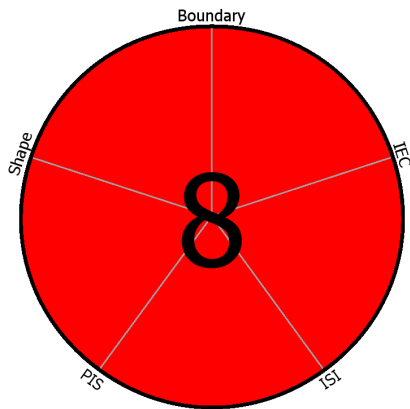
(b) MIP of the lesion



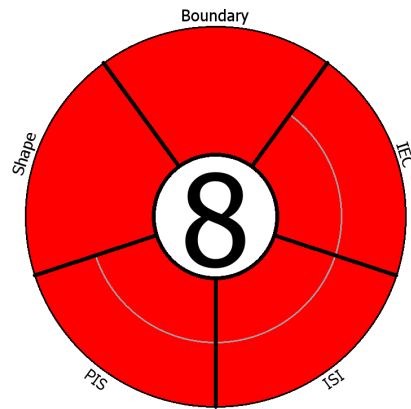
(c) Slice of the lesion



(d) Linear MAP

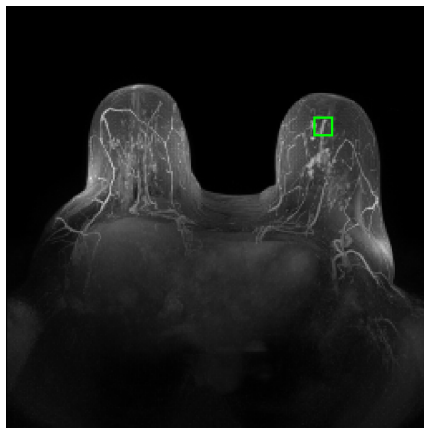


(e) Cubic MAP

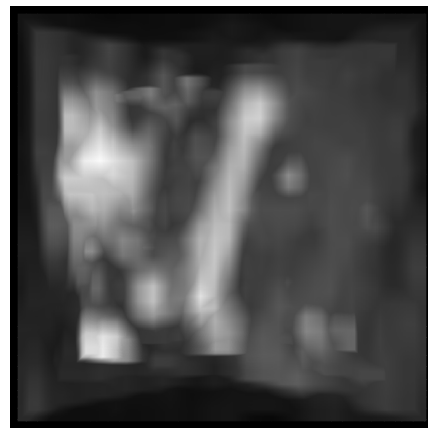


(f) Sunburst MAP

Figure A.2: Lesion 02.1. **(a)** Transversal MIP of the entire data set. **(b)** Lesion at early post-contrast phase. **(c)** Slice of the lesion. Finally, the representations of the Göttinger score visualized by the linear MAP **(d)**, the cubic MAP **(e)** and the sunburst MAP **(f)**.



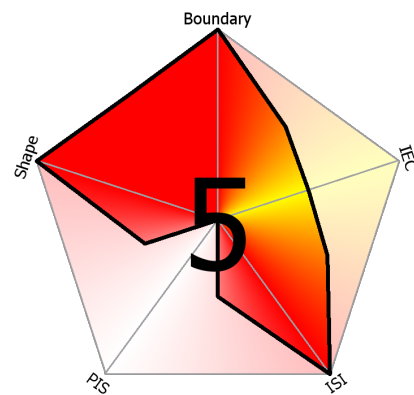
(a) MIP of the entire data set



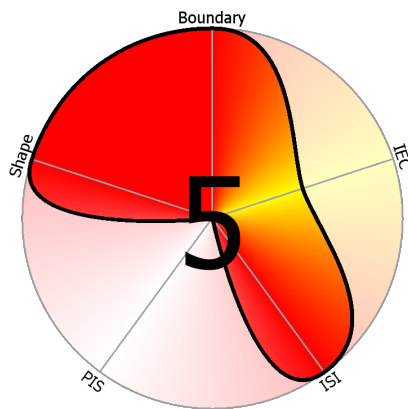
(b) MIP of the lesion



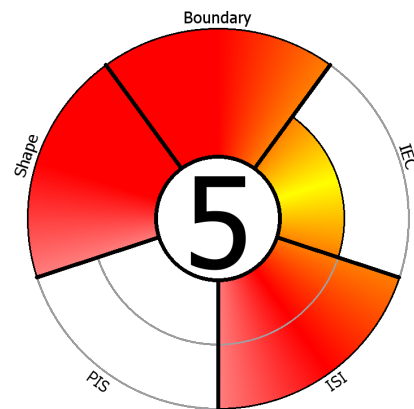
(c) Slice of the lesion



(d) Linear MAP

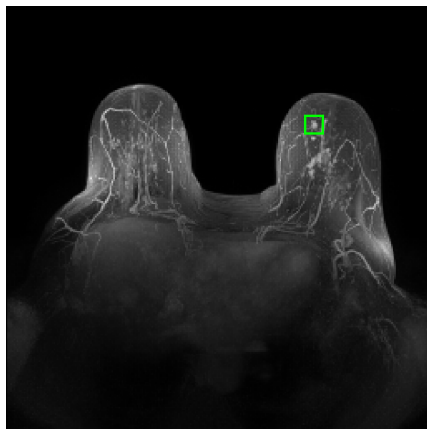


(e) Cubic MAP



(f) Sunburst MAP

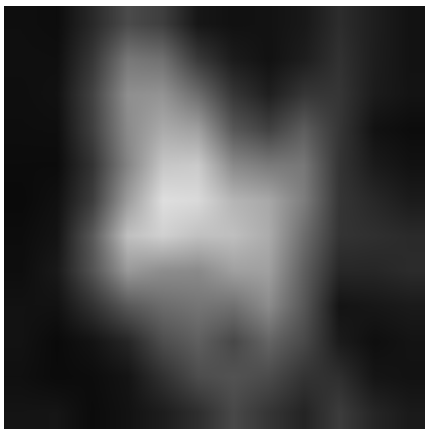
Figure A.3: Lesion 03.1. **(a)** Transversal MIP of the entire data set. **(b)** Lesion at early post-contrast phase. **(c)** Slice of the lesion. Finally, the representations of the Göttinger score visualized by the linear MAP **(d)**, the cubic MAP **(e)** and the sunburst MAP **(f)**.



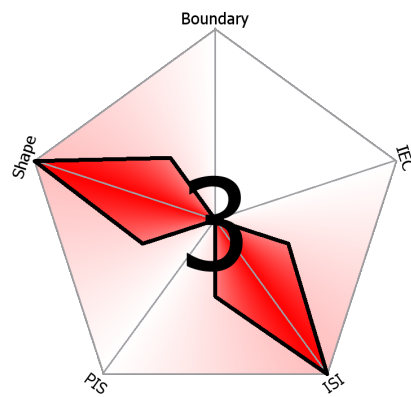
(a) MIP of the entire data set



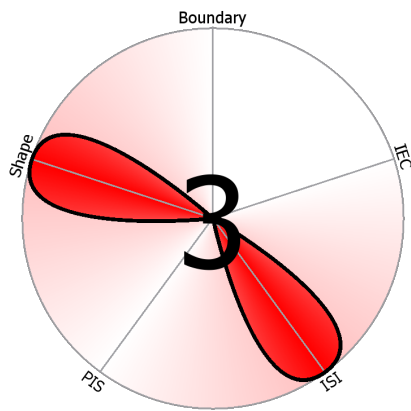
(b) MIP of the lesion



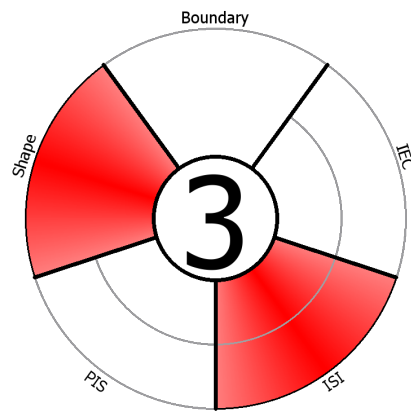
(c) Slice of the lesion



(d) Linear MAP

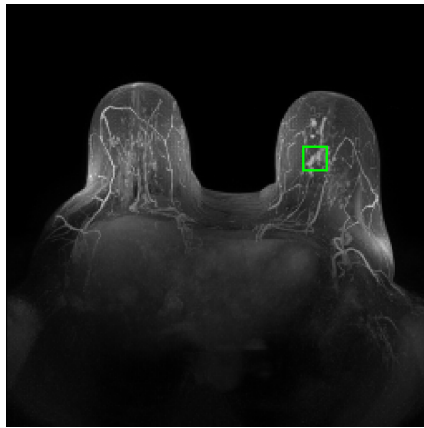


(e) Cubic MAP

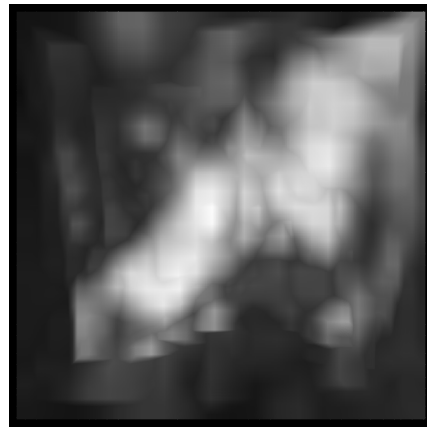


(f) Sunburst MAP

Figure A.4: Lesion 03.2. **(a)** Transversal MIP of the entire data set. **(b)** Lesion at early post-contrast phase. **(c)** Slice of the lesion. Finally, the representations of the Göttinger score visualized by the linear MAP **(d)**, the cubic MAP **(e)** and the sunburst MAP **(f)**.



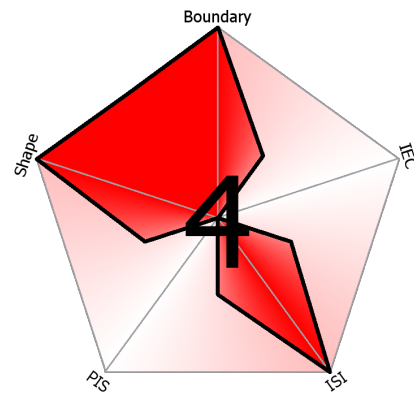
(a) MIP of the entire data set



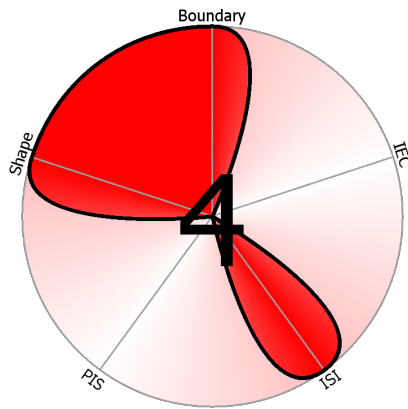
(b) MIP of the lesion



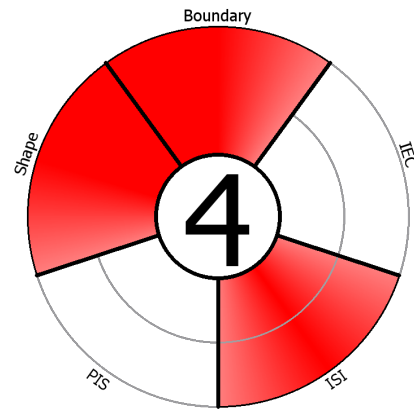
(c) Slice of the lesion



(d) Linear MAP

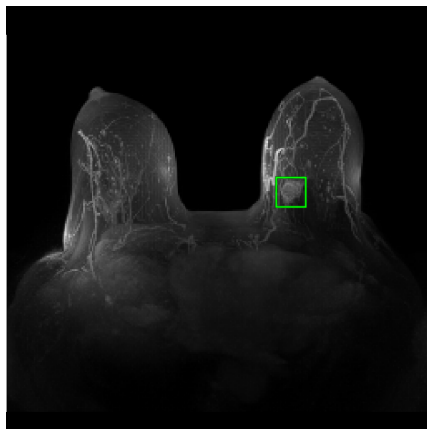


(e) Cubic MAP



(f) Sunburst MAP

Figure A.5: Lesion 03.3. **(a)** Transversal MIP of the entire data set. **(b)** Lesion at early post-contrast phase. **(c)** Slice of the lesion. Finally, the representations of the Göttinger score visualized by the linear MAP **(d)**, the cubic MAP **(e)** and the sunburst MAP **(f)**.



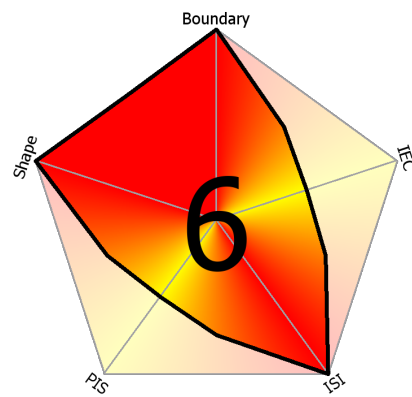
(a) MIP of the entire data set



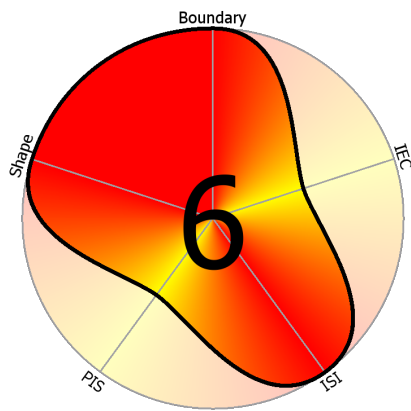
(b) MIP of the lesion



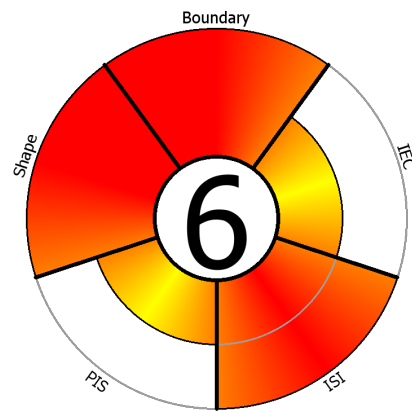
(c) Slice of the lesion



(d) Linear MAP

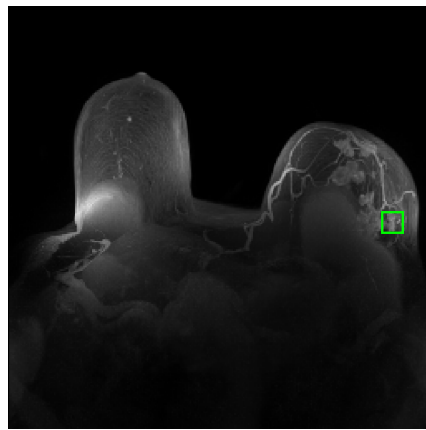


(e) Cubic MAP

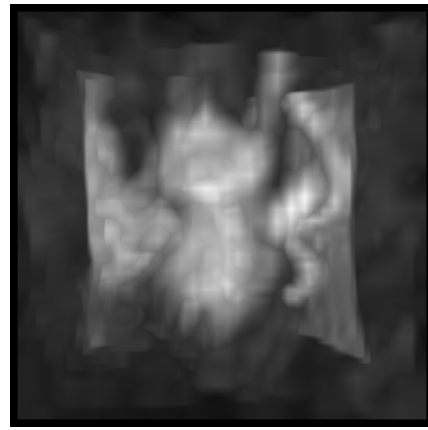


(f) Sunburst MAP

Figure A.6: Lesion 04.1. **(a)** Transversal MIP of the entire data set. **(b)** Lesion at early post-contrast phase. **(c)** Slice of the lesion. Finally, the representations of the Göttinger score visualized by the linear MAP **(d)**, the cubic MAP **(e)** and the sunburst MAP **(f)**.



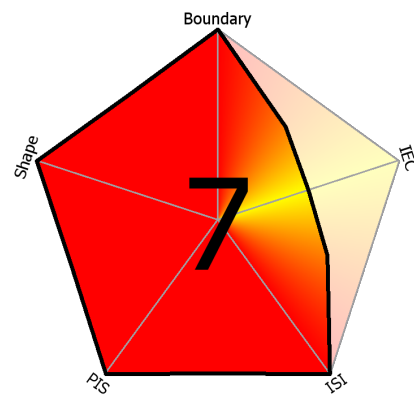
(a) MIP of the entire data set



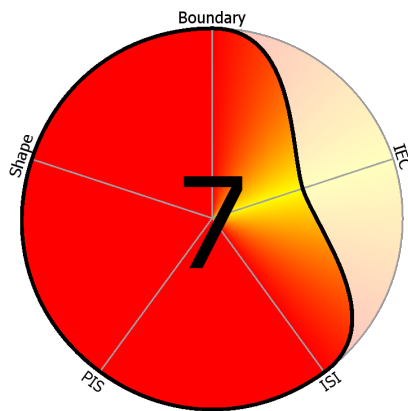
(b) MIP of the lesion



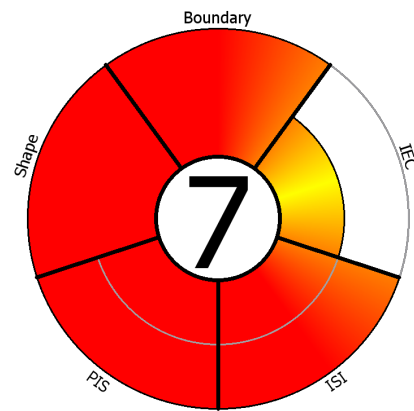
(c) Slice of the lesion



(d) Linear MAP

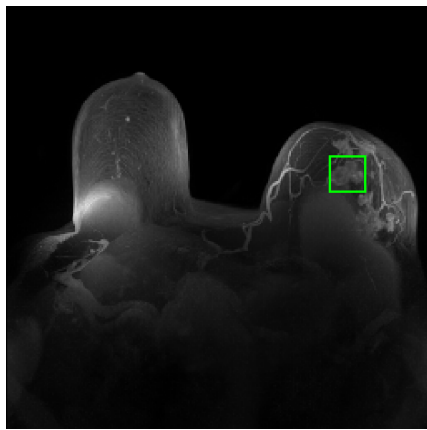


(e) Cubic MAP

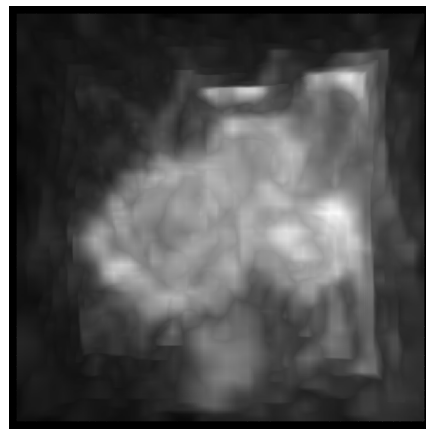


(f) Sunburst MAP

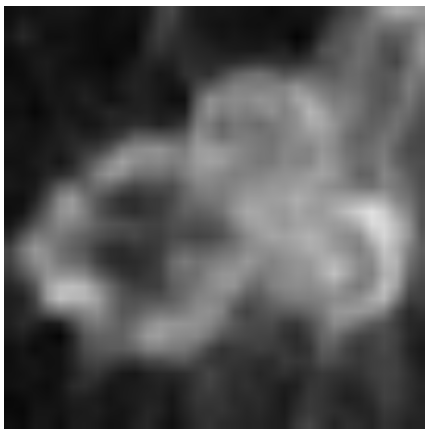
Figure A.7: Lesion 05.1. **(a)** Transversal MIP of the entire data set. **(b)** Lesion at early post-contrast phase. **(c)** Slice of the lesion. Finally, the representations of the Göttinger score visualized by the linear MAP **(d)**, the cubic MAP **(e)** and the sunburst MAP **(f)**.



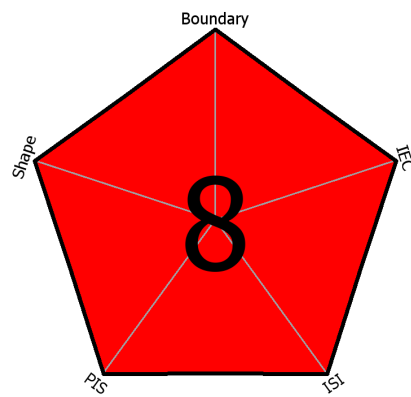
(a) MIP of the entire data set



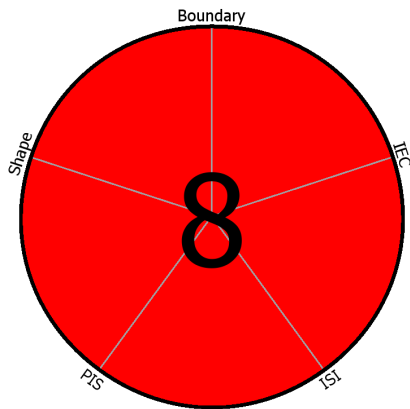
(b) MIP of the lesion



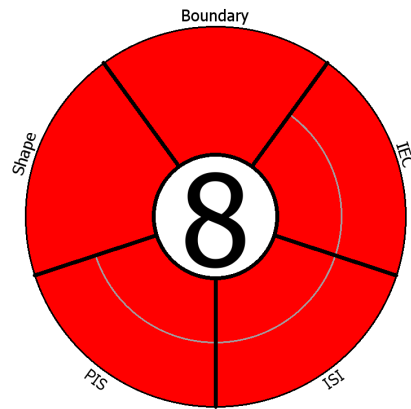
(c) Slice of the lesion



(d) Linear MAP

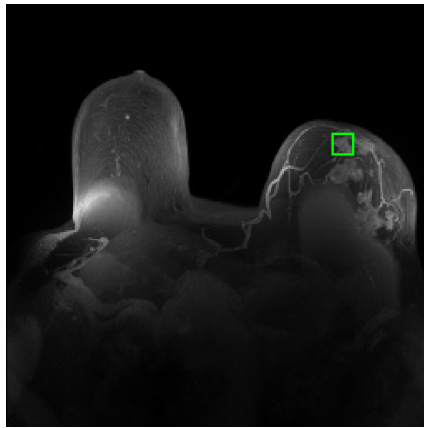


(e) Cubic MAP

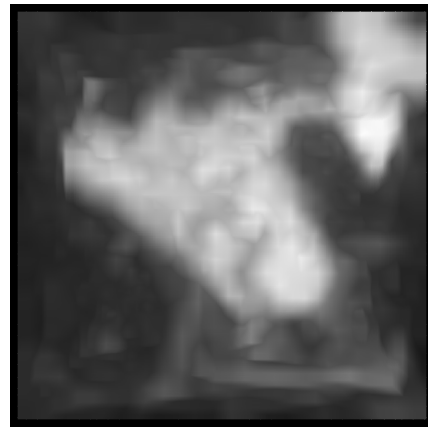


(f) Sunburst MAP

Figure A.8: Lesion 05.2. **(a)** Transversal MIP of the entire data set. **(b)** Lesion at early post-contrast phase. **(c)** Slice of the lesion. Finally, the representations of the Göttinger score visualized by the linear MAP **(d)**, the cubic MAP **(e)** and the sunburst MAP **(f)**.



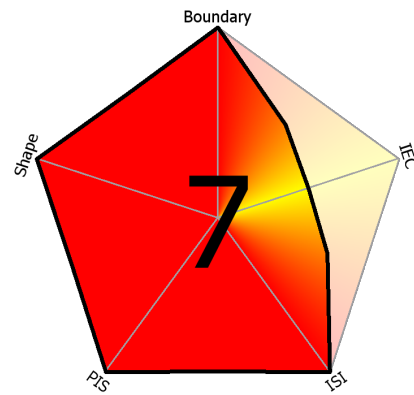
(a) MIP of the entire data set



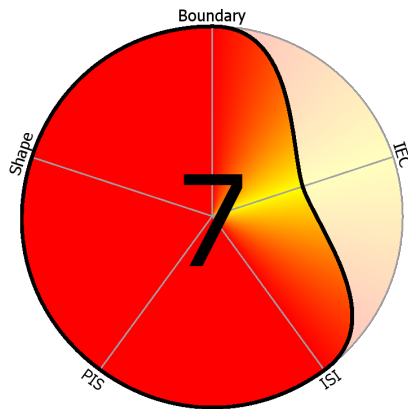
(b) MIP of the lesion



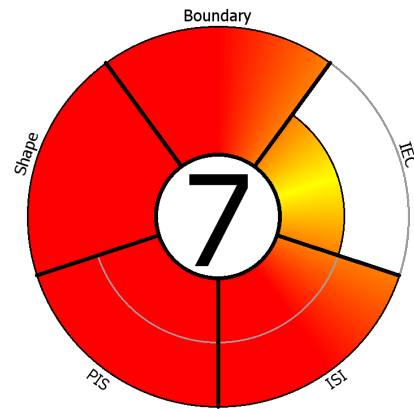
(c) Slice of the lesion



(d) Linear MAP

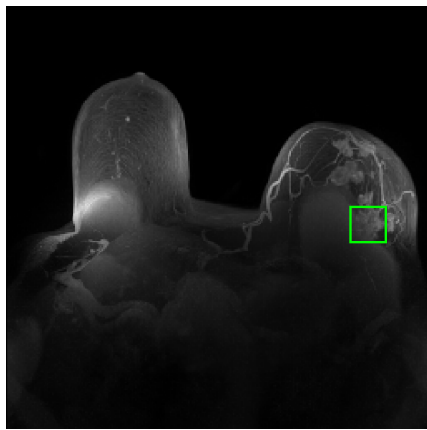


(e) Cubic MAP



(f) Sunburst MAP

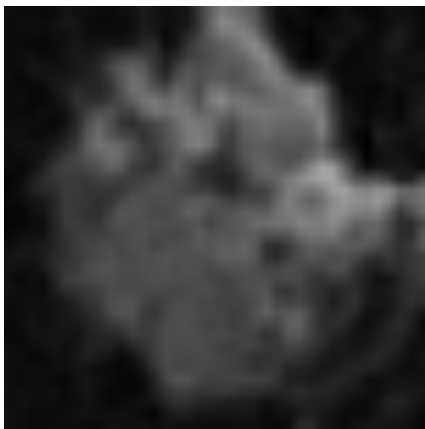
Figure A.9: Lesion 05.3. **(a)** Transversal MIP of the entire data set. **(b)** Lesion at early post-contrast phase. **(c)** Slice of the lesion. Finally, the representations of the Göttinger score visualized by the linear MAP **(d)**, the cubic MAP **(e)** and the sunburst MAP **(f)**.



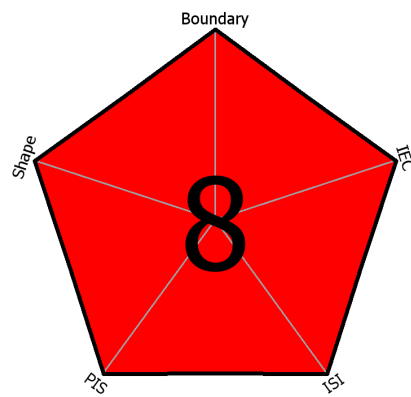
(a) MIP of the entire data set



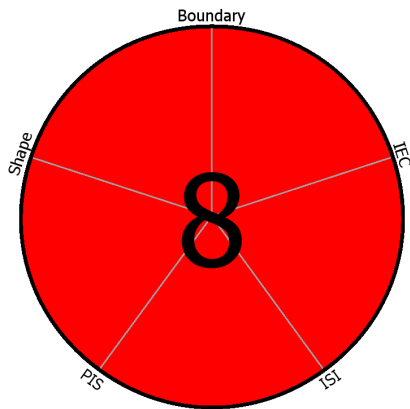
(b) MIP of the lesion



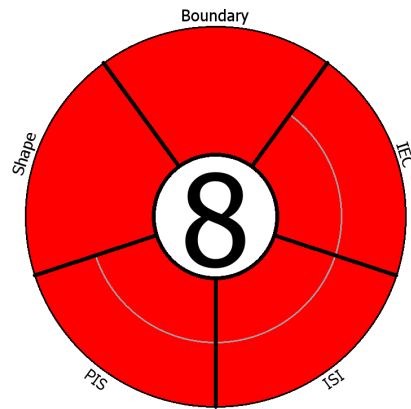
(c) Slice of the lesion



(d) Linear MAP

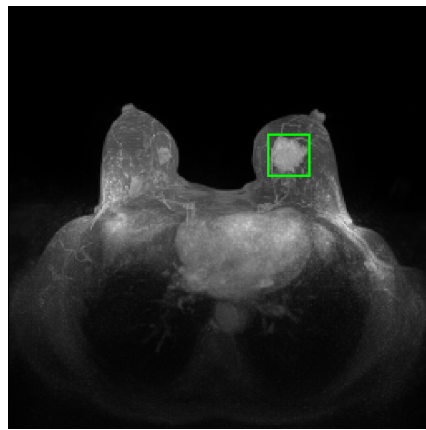


(e) Cubic MAP

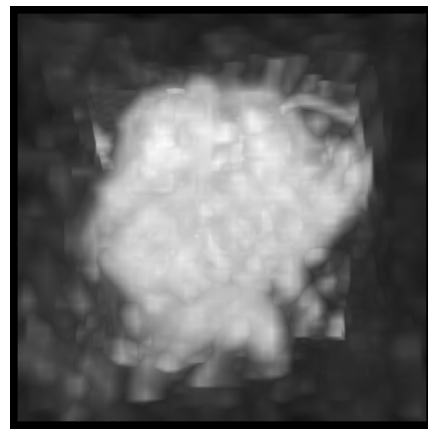


(f) Sunburst MAP

Figure A.10: Lesion 05.4. **(a)** Transversal MIP of the entire data set. **(b)** Lesion at early post-contrast phase. **(c)** Slice of the lesion. Finally, the representations of the Göttinger score visualized by the linear MAP **(d)**, the cubic MAP **(e)** and the sunburst MAP **(f)**.



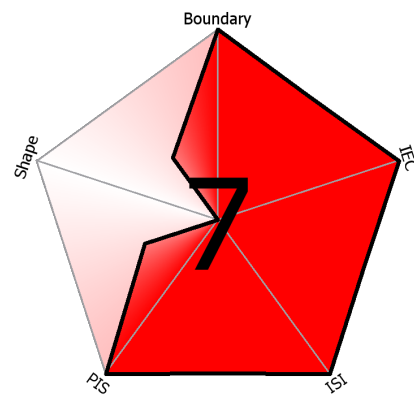
(a) MIP of the entire data set



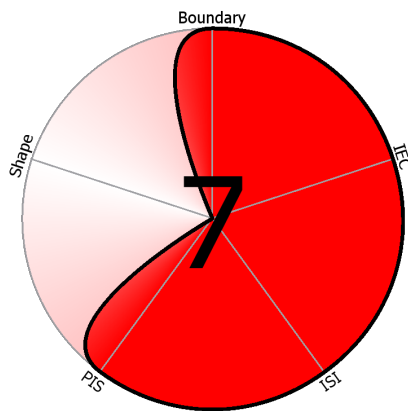
(b) MIP of the lesion



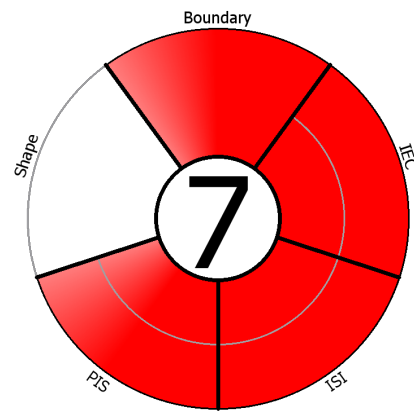
(c) Slice of the lesion



(d) Linear MAP

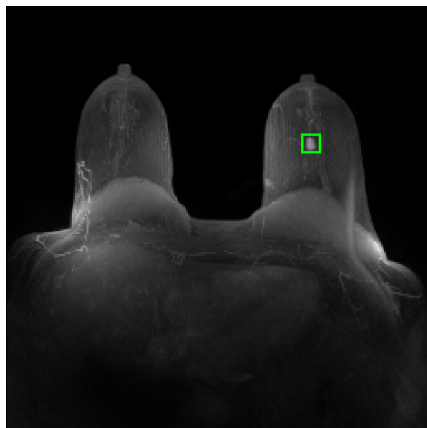


(e) Cubic MAP

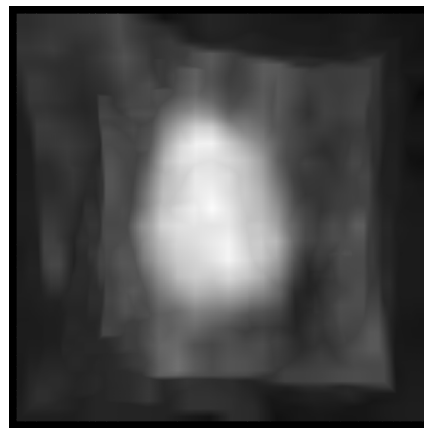


(f) Sunburst MAP

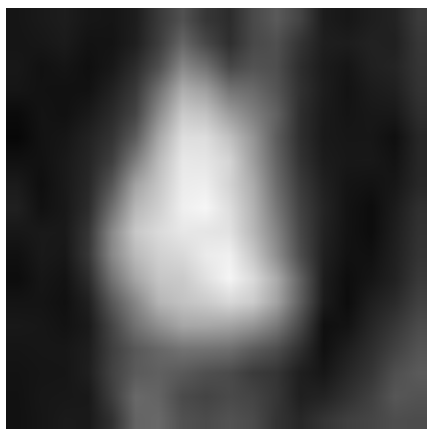
Figure A.11: Lesion 06.1. **(a)** Transversal MIP of the entire data set. **(b)** Lesion at early post-contrast phase. **(c)** Slice of the lesion. Finally, the representations of the Göttinger score visualized by the linear MAP **(d)**, the cubic MAP **(e)** and the sunburst MAP **(f)**.



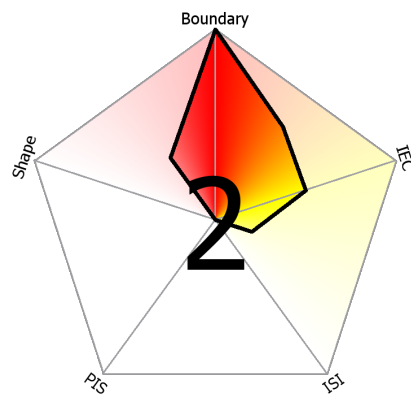
(a) MIP of the entire data set



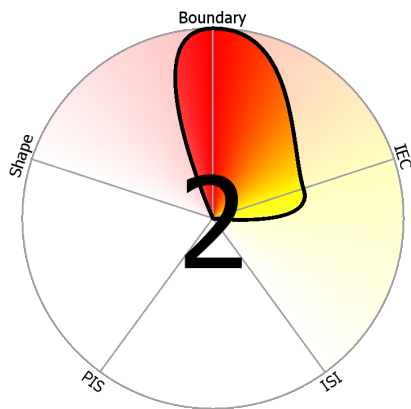
(b) MIP of the lesion



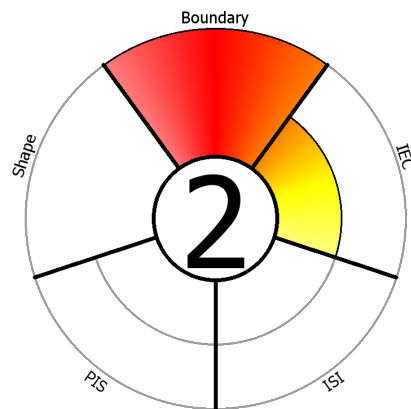
(c) Slice of the lesion



(d) Linear MAP

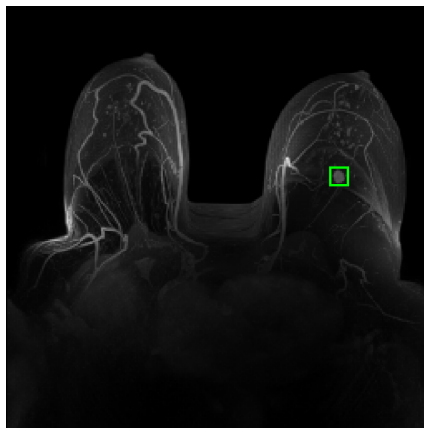


(e) Cubic MAP

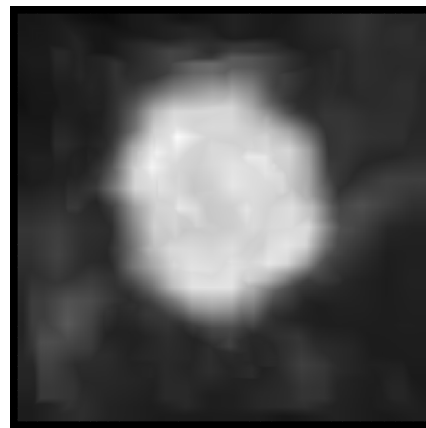


(f) Sunburst MAP

Figure A.12: Lesion 07.1. (a) Transversal MIP of the entire data set. (b) Lesion at early post-contrast phase. (c) Slice of the lesion. Finally, the representations of the Göttinger score visualized by the linear MAP (d), the cubic MAP (e) and the sunburst MAP (f).



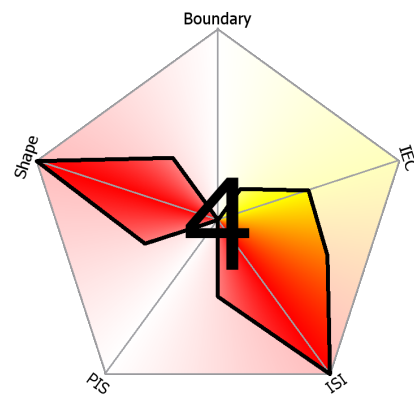
(a) MIP of the entire data set



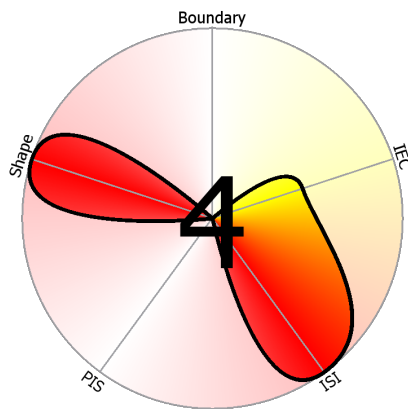
(b) MIP of the lesion



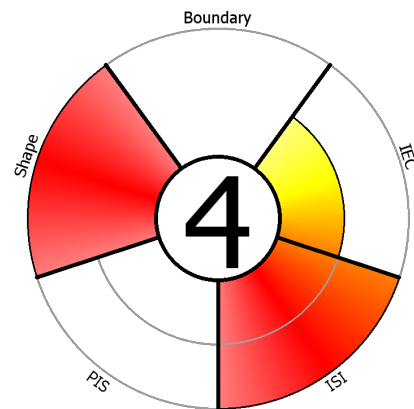
(c) Slice of the lesion



(d) Linear MAP

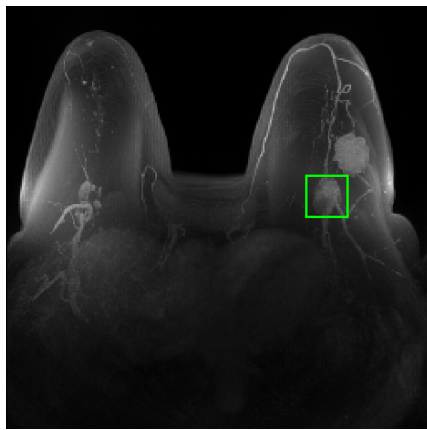


(e) Cubic MAP

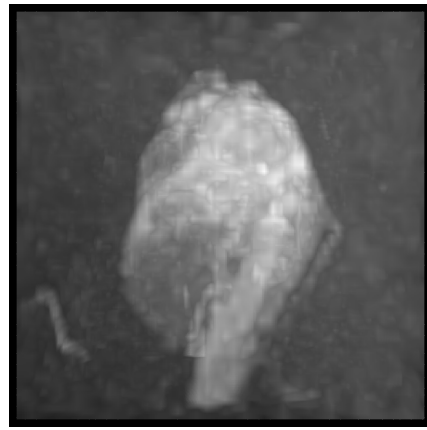


(f) Sunburst MAP

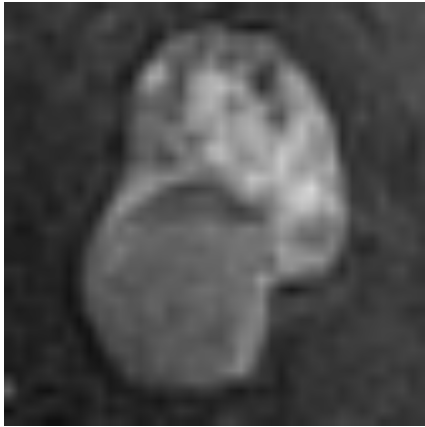
Figure A.13: Lesion 08.1. **(a)** Transversal MIP of the entire data set. **(b)** Lesion at early post-contrast phase. **(c)** Slice of the lesion. Finally, the representations of the Göttinger score visualized by the linear MAP **(d)**, the cubic MAP **(e)** and the sunburst MAP **(f)**.



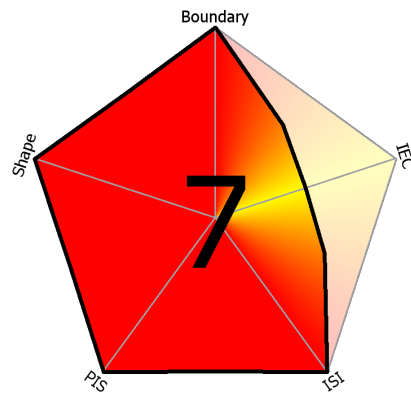
(a) MIP of the entire data set



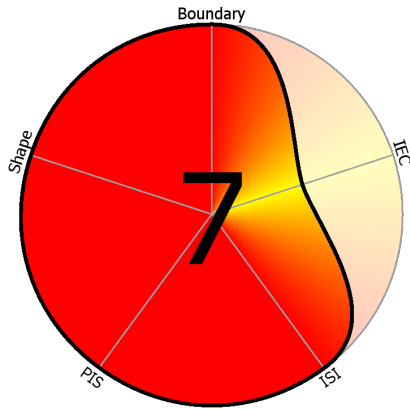
(b) MIP of the lesion



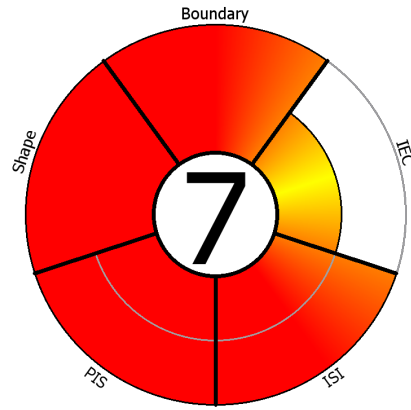
(c) Slice of the lesion



(d) Linear MAP

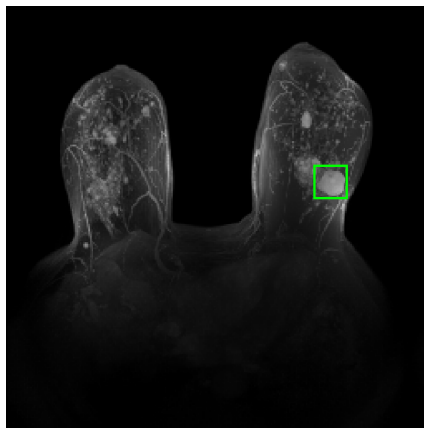


(e) Cubic MAP

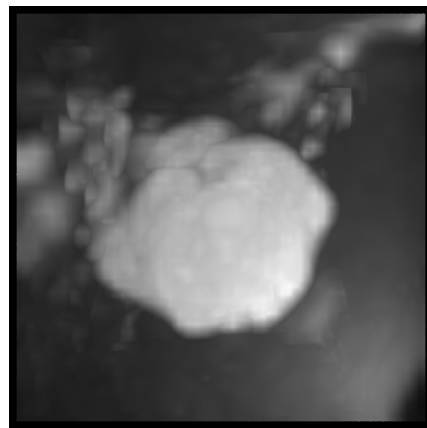


(f) Sunburst MAP

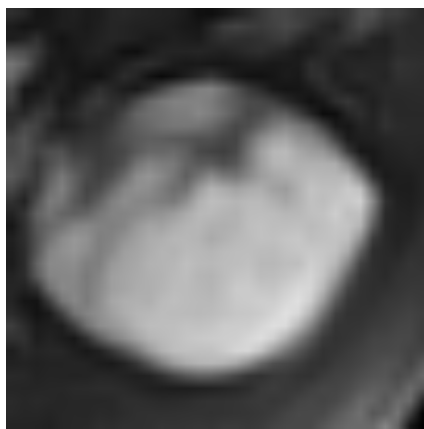
Figure A.14: Lesion 09.1. **(a)** Transversal MIP of the entire data set. **(b)** Lesion at early post-contrast phase. **(c)** Slice of the lesion. Finally, the representations of the Göttinger score visualized by the linear MAP **(d)**, the cubic MAP **(e)** and the sunburst MAP **(f)**.



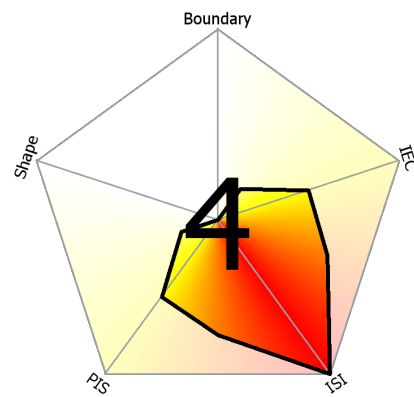
(a) MIP of the entire data set



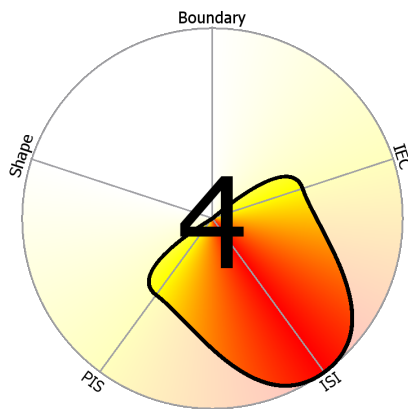
(b) MIP of the lesion



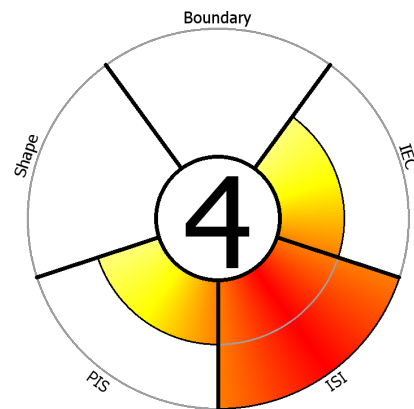
(c) Slice of the lesion



(d) Linear MAP

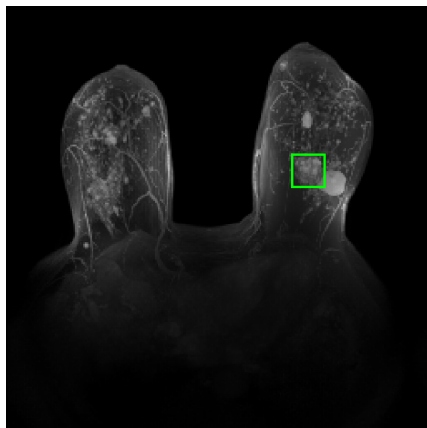


(e) Cubic MAP

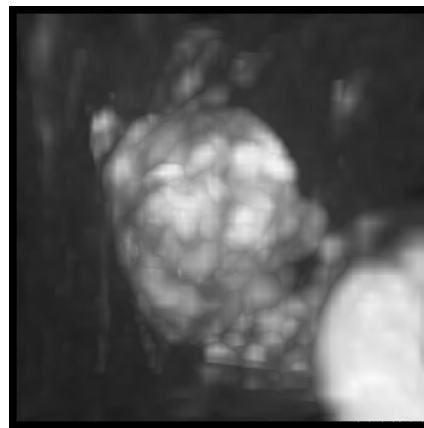


(f) Sunburst MAP

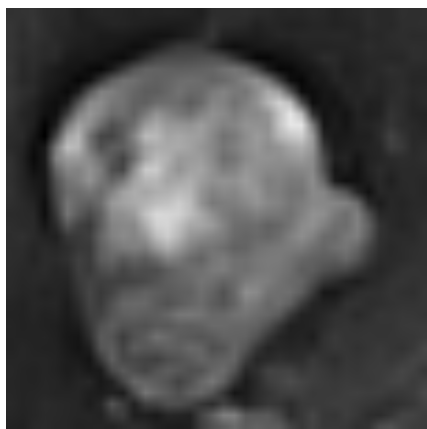
Figure A.15: Lesion 10.1. **(a)** Transversal MIP of the entire data set. **(b)** Lesion at early post-contrast phase. **(c)** Slice of the lesion. Finally, the representations of the Göttinger score visualized by the linear MAP **(d)**, the cubic MAP **(e)** and the sunburst MAP **(f)**.



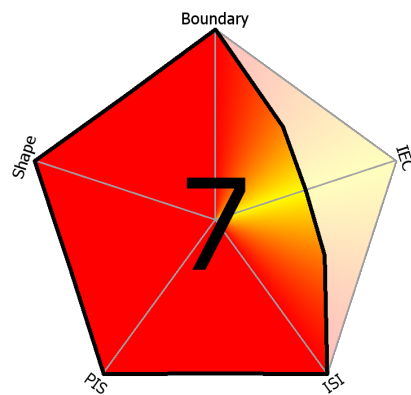
(a) MIP of the entire data set



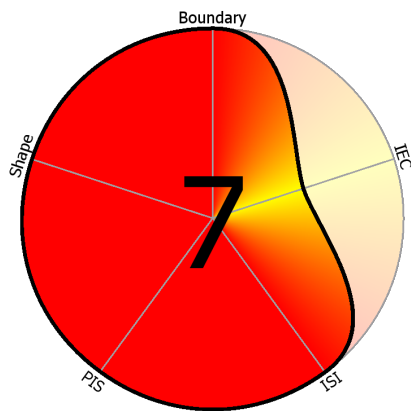
(b) MIP of the lesion



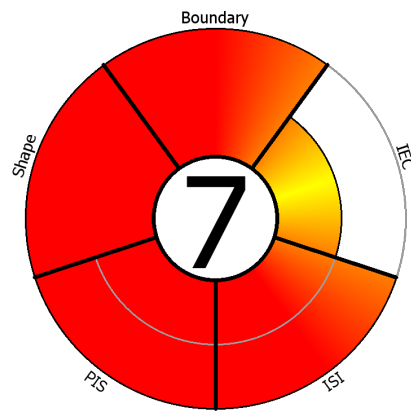
(c) Slice of the lesion



(d) Linear MAP

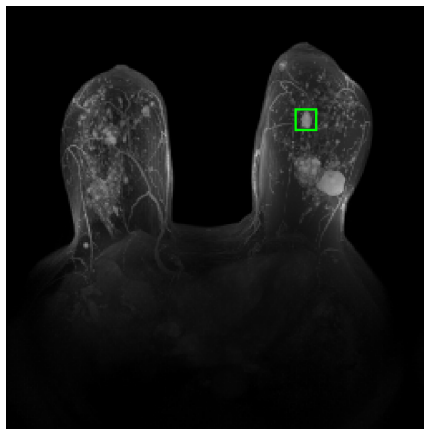


(e) Cubic MAP

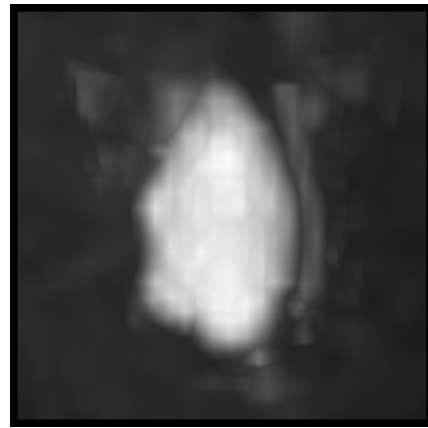


(f) Sunburst MAP

Figure A.16: Lesion 10.2. **(a)** Transversal MIP of the entire data set. **(b)** Lesion at early post-contrast phase. **(c)** Slice of the lesion. Finally, the representations of the Göttinger score visualized by the linear MAP **(d)**, the cubic MAP **(e)** and the sunburst MAP **(f)**.



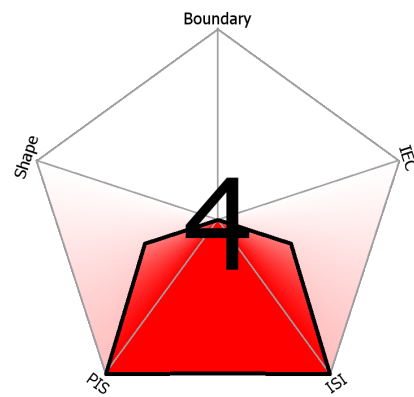
(a) MIP of the entire data set



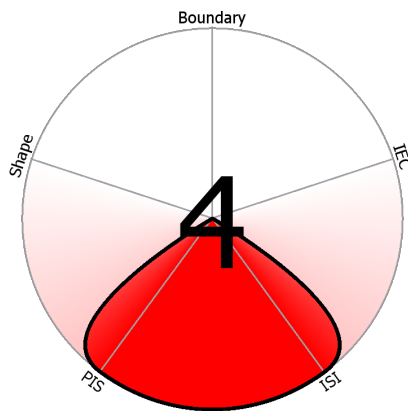
(b) MIP of the lesion



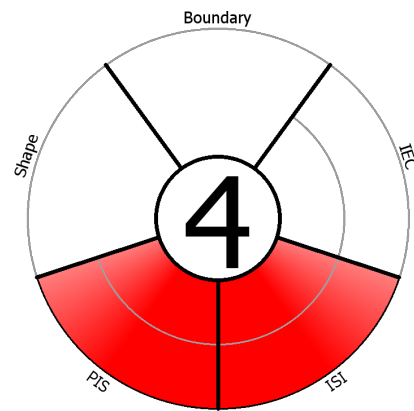
(c) Slice of the lesion



(d) Linear MAP

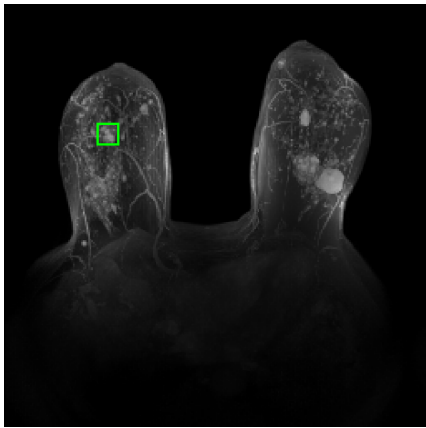


(e) Cubic MAP

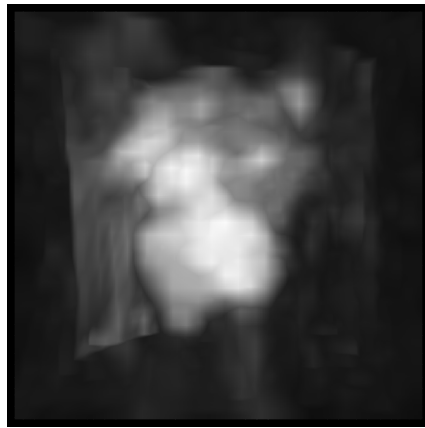


(f) Sunburst MAP

Figure A.17: Lesion 10.3. **(a)** Transversal MIP of the entire data set. **(b)** Lesion at early post-contrast phase. **(c)** Slice of the lesion. Finally, the representations of the Göttinger score visualized by the linear MAP **(d)**, the cubic MAP **(e)** and the sunburst MAP **(f)**.



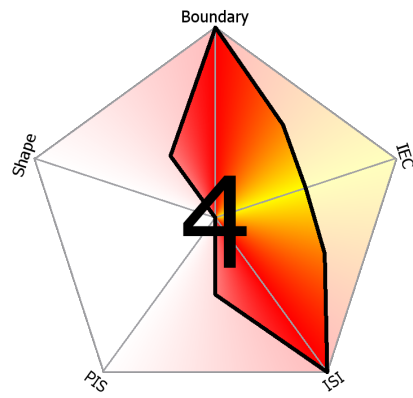
(a) MIP of the entire data set



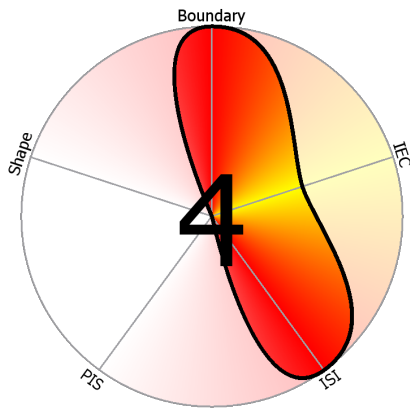
(b) MIP of the lesion



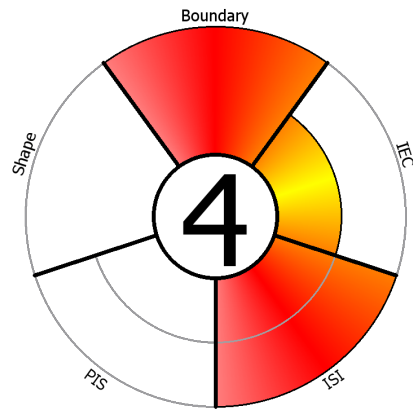
(c) Slice of the lesion



(d) Linear MAP

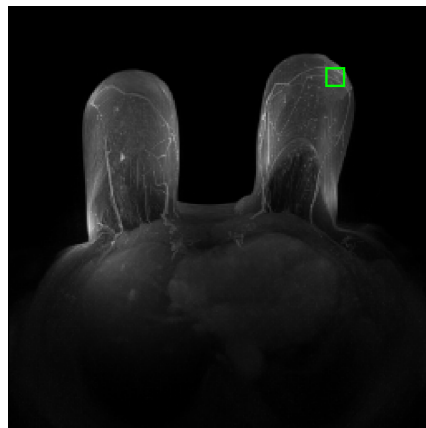


(e) Cubic MAP

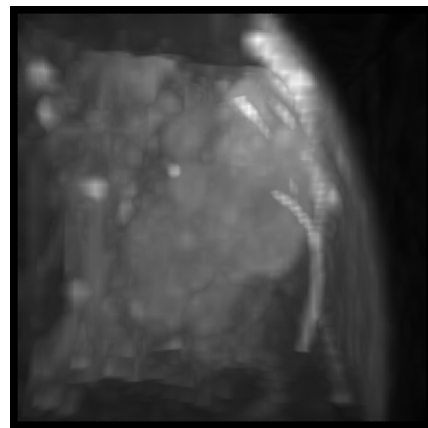


(f) Sunburst MAP

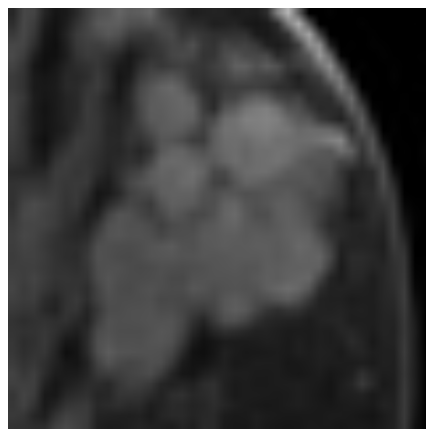
Figure A.18: Lesion 10.4. **(a)** Transversal MIP of the entire data set. **(b)** Lesion at early post-contrast phase. **(c)** Slice of the lesion. Finally, the representations of the Göttinger score visualized by the linear MAP **(d)**, the cubic MAP **(e)** and the sunburst MAP **(f)**.



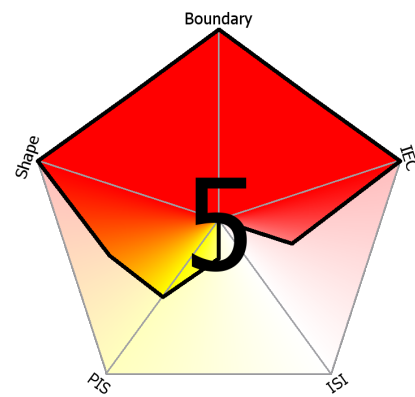
(a) MIP of the entire data set



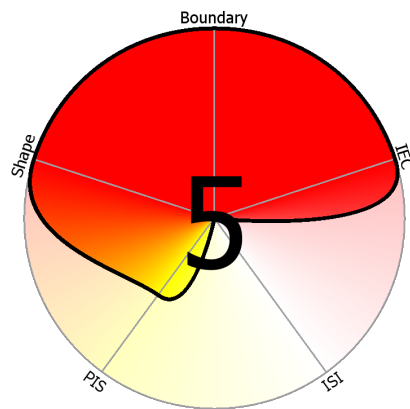
(b) MIP of the lesion



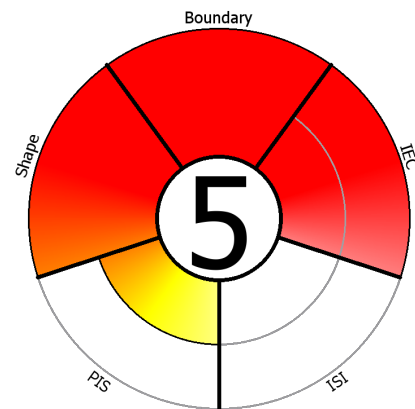
(c) Slice of the lesion



(d) Linear MAP

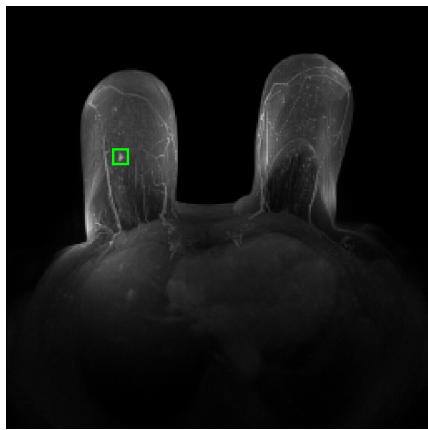


(e) Cubic MAP

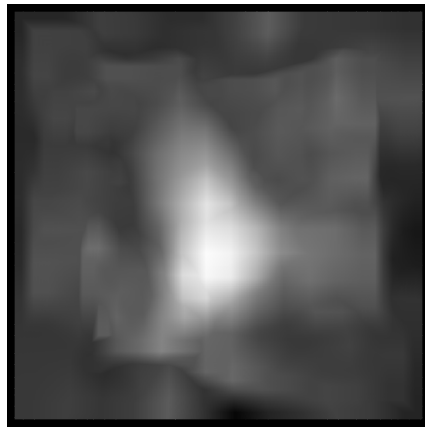


(f) Sunburst MAP

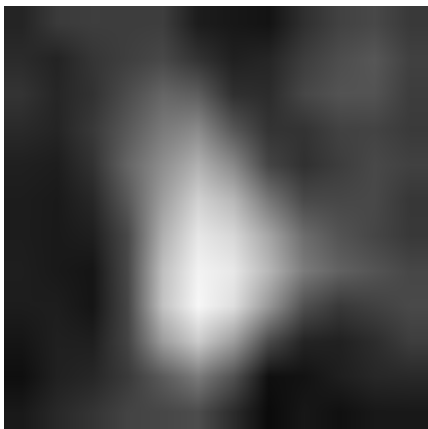
Figure A.19: Lesion 11.1. **(a)** Transversal MIP of the entire data set. **(b)** Lesion at early post-contrast phase. **(c)** Slice of the lesion. Finally, the representations of the Göttinger score visualized by the linear MAP **(d)**, the cubic MAP **(e)** and the sunburst MAP **(f)**.



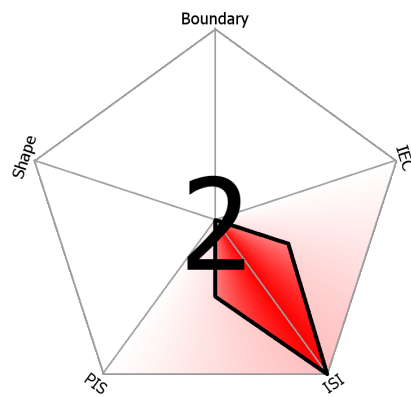
(a) MIP of the entire data set



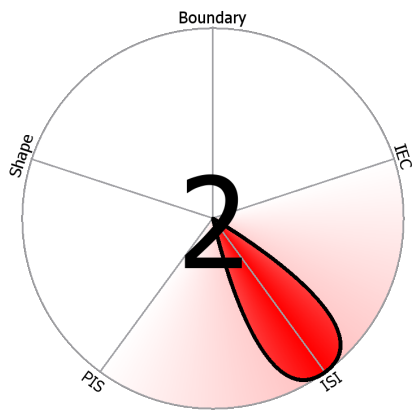
(b) MIP of the lesion



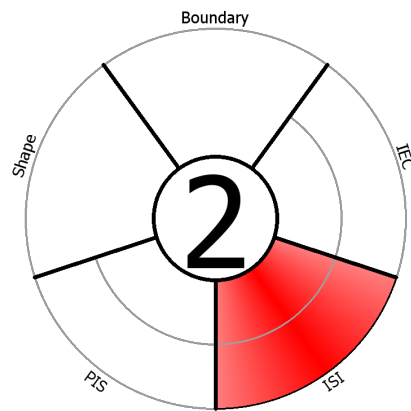
(c) Slice of the lesion



(d) Linear MAP

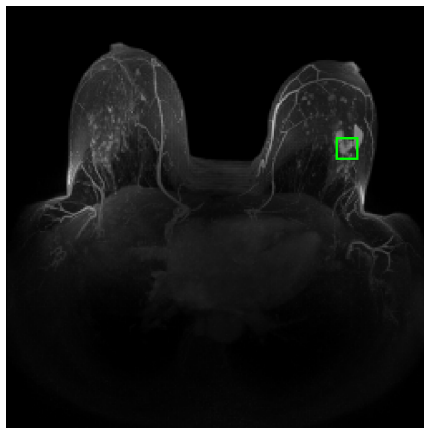


(e) Cubic MAP

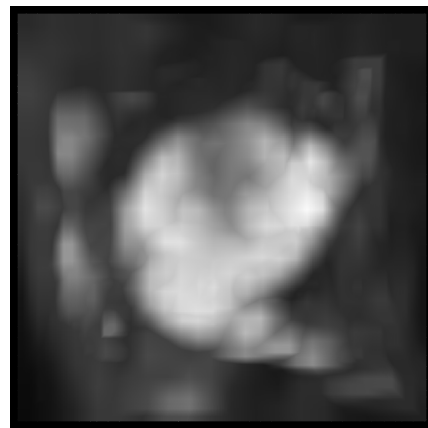


(f) Sunburst MAP

Figure A.20: Lesion 11.2. **(a)** Transversal MIP of the entire data set. **(b)** Lesion at early post-contrast phase. **(c)** Slice of the lesion. Finally, the representations of the Göttinger score visualized by the linear MAP **(d)**, the cubic MAP **(e)** and the sunburst MAP **(f)**.



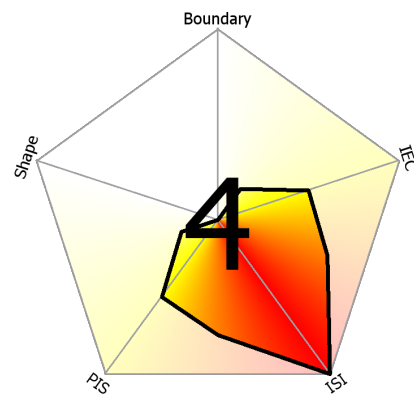
(a) MIP of the entire data set



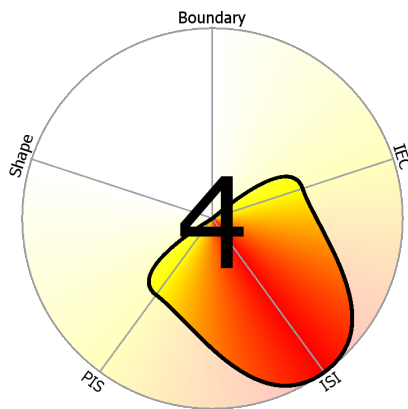
(b) MIP of the lesion



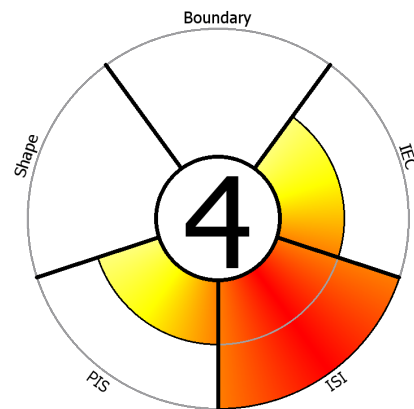
(c) Slice of the lesion



(d) Linear MAP

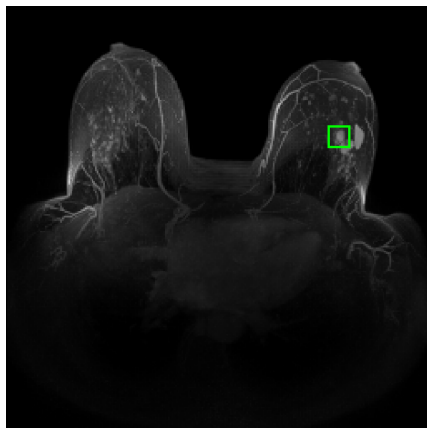


(e) Cubic MAP

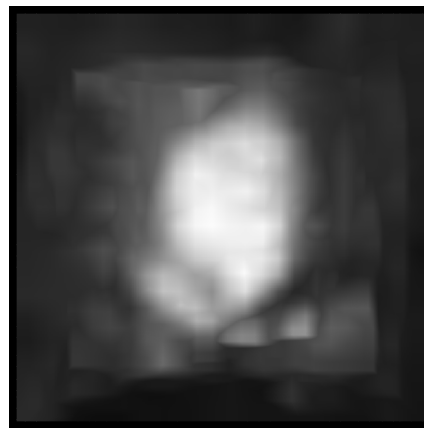


(f) Sunburst MAP

Figure A.21: Lesion 12.1. (a) Transversal MIP of the entire data set. (b) Lesion at early post-contrast phase. (c) Slice of the lesion. Finally, the representations of the Göttinger score visualized by the linear MAP (d), the cubic MAP (e) and the sunburst MAP (f).



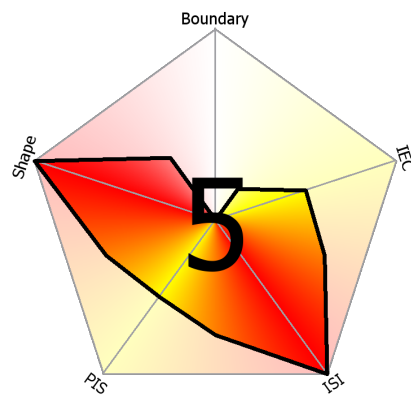
(a) MIP of the entire data set



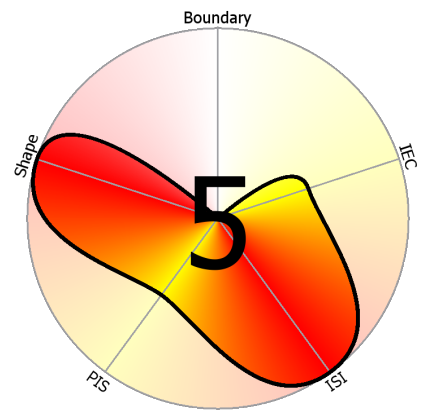
(b) MIP of the lesion



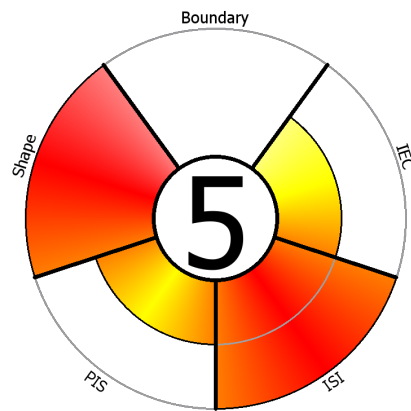
(c) Slice of the lesion



(d) Linear MAP



(e) Cubic MAP



(f) Sunburst MAP

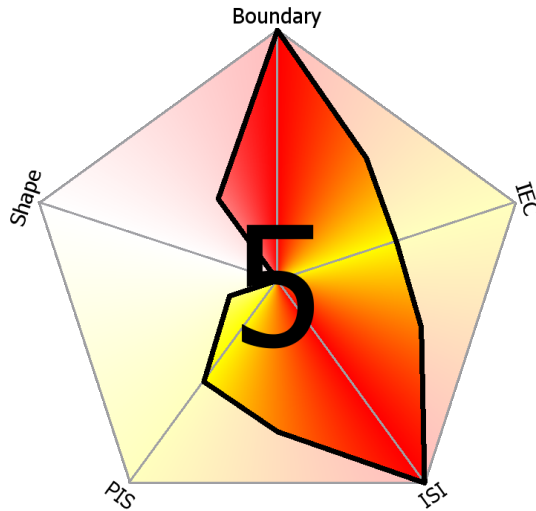
Figure A.22: Lesion 12.2. (a) Transversal MIP of the entire data set. (b) Lesion at early post-contrast phase. (c) Slice of the lesion. Finally, the representations of the Göttinger score visualized by the linear MAP (d), the cubic MAP (e) and the sunburst MAP (f).

Malignancy Area Plot Survey

This survey is used to evaluate plots for visualizing the Göttinger score used in breast cancer diagnosis. The plots were developed during my Master's thesis at the Vienna University of Technology. Based on a star plot and the sunburst chart, the five features **Shape**, **Boundary**, **Internal Enhancement Characteristics (IEC)**, **Initial Signal Increase (ISI)** and **Post-Initial Signal (PIS)** are arranged around a center. The middle of the plot represents the score that can be assigned to the features. In our case these are **zero** points. The outer part of the circle represents the feature's maximum score that can be assigned to it. In case of shape and boundary this is **one** point. In case of the other features this is **two** points.

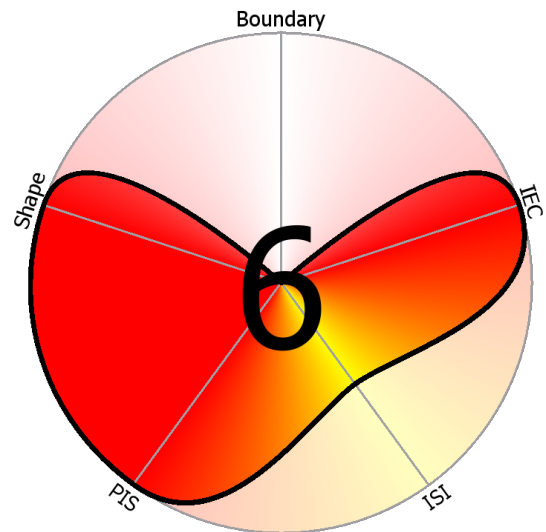
B.1 Linear and Cubic Malignancy Area Plots

The Malignancy Area Plot (MAP) is based on the star plot. An area is drawn depending on the values of the features. Two possible area plottings were implemented: a cubic (circular) and a linear (pentagon) area plot.



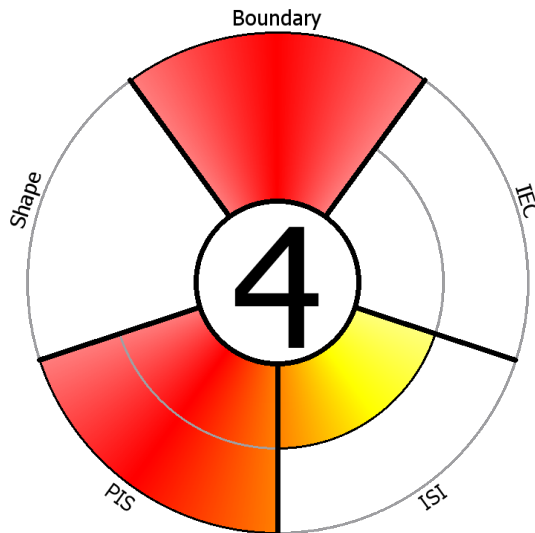
Feature	Points
Shape	0 / 1
Boundary	1 / 1
POE	1 / 2
ISI	2 / 2
PIS	1 / 2

Feature	Points
Shape	1 / 1
Boundary	0 / 1
POE	2 / 2
ISI	1 / 2
PIS	2 / 2



B.2 Sunburst Malignancy Area Plot

The sunburst MAP is divided up into sectors. The different sectors are filled with color depending on the individual feature scores. The inner sector is not colored if the minimum score (0) is assigned. A sector is filled red for when the maximum score is assigned to a feature. Yellow is used for features with maximum two points if one point is assigned to it.



Feature	Points
Shape	0 / 1
Boundary	1 / 1
POE	0 / 2
ISI	1 / 2
PIS	2 / 2

B.3 Speed Test

The following test shows you either a tabular representation of randomly generated Göttinger score features, or a visual representation by either a linear or cubic MAP or the suburst based plot. The task is to do a simple **benign versus malignant classification**. Göttinger scores less or equal to **three (3)** are considered being **benign** while Göttinger scores bigger than **three** are considered being **malignant**. Press the button **benign** or **malignant** depending on the visually presented Göttinger score. The overall score is not shown in the images. The time is measured how long you need to classify a representation as well as if the classification was done correctly.

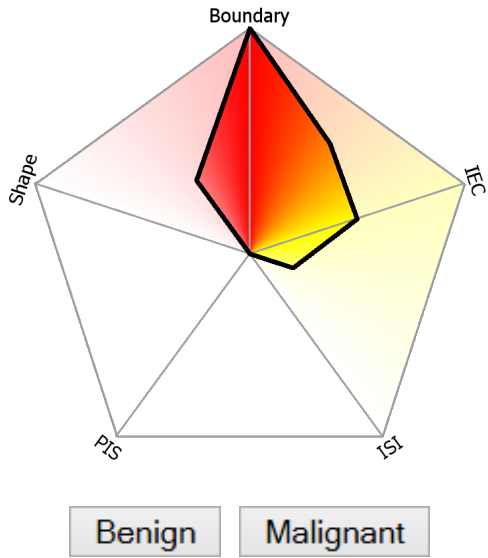


Figure B.1: Speed Test 01.

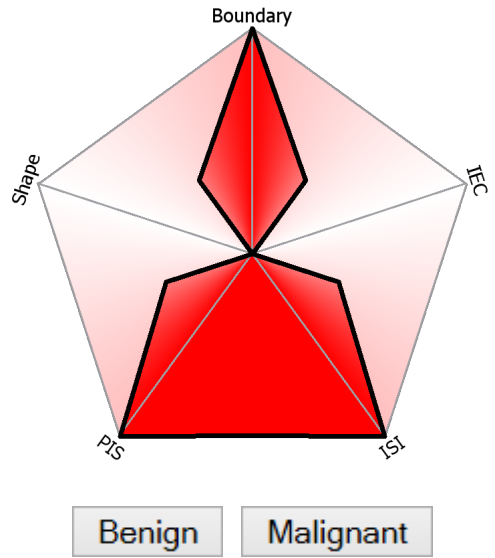


Figure B.2: Speed Test 02.

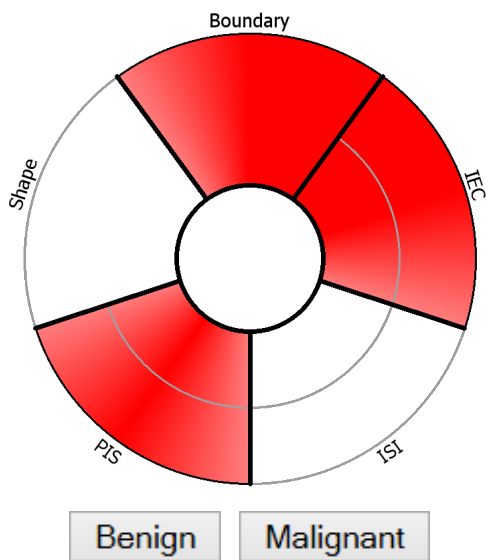


Figure B.3: Speed Test 03.

Feature	Points
Shape	0
Boundary	1
POE	0
ISI	0
PIS	2

Benign Malignant

Figure B.4: Speed Test 04.

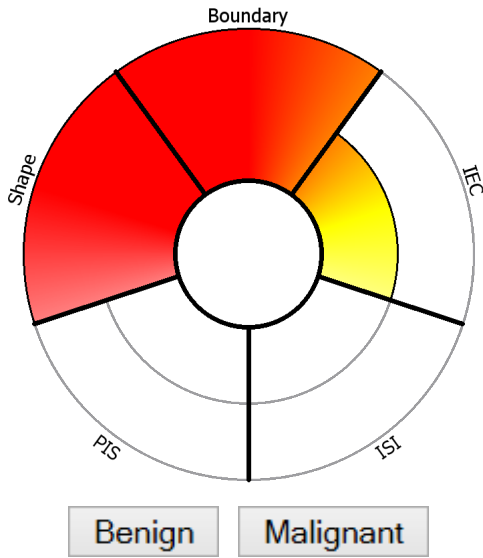


Figure B.5: Speed Test 05.

Feature	Points
Shape	0
Boundary	1
POE	0
ISI	0
PIS	2

Benign Malignant

Figure B.6: Speed Test 06.

Feature	Points
Shape	0
Boundary	1
POE	0
ISI	0
PIS	2

Benign Malignant

Figure B.7: Speed Test 07.

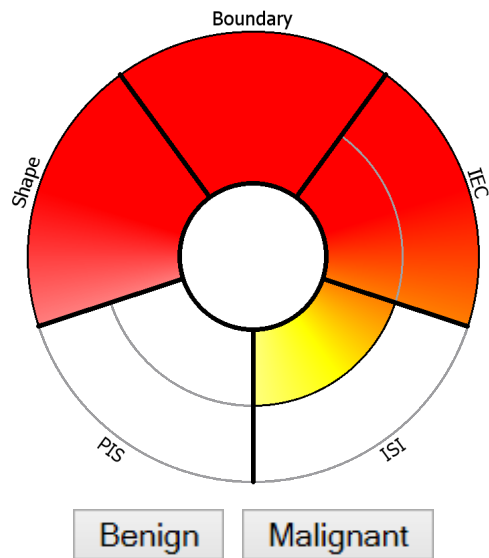


Figure B.8: Speed Test 08.

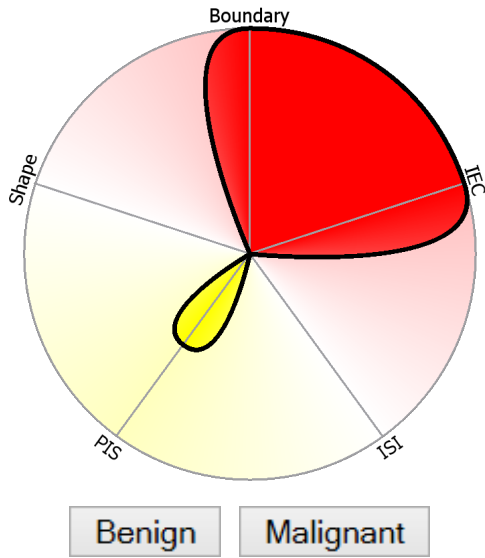


Figure B.9: Speed Test 09.

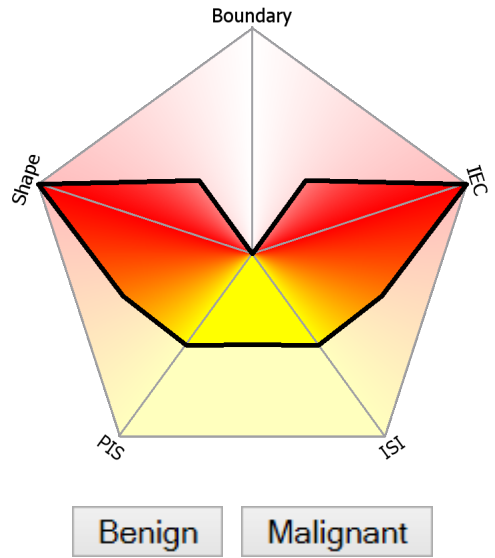


Figure B.10: Speed Test 10.

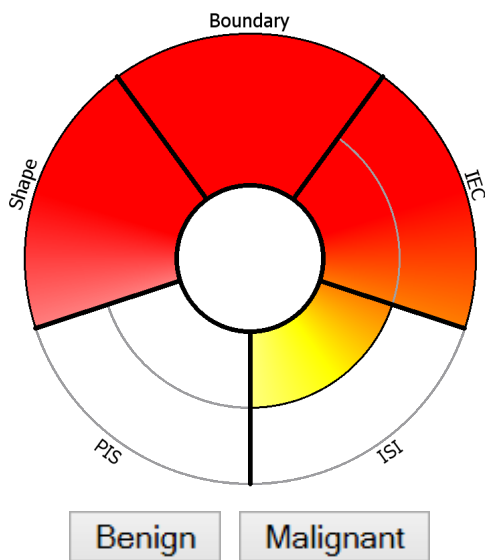


Figure B.11: Speed Test 11.

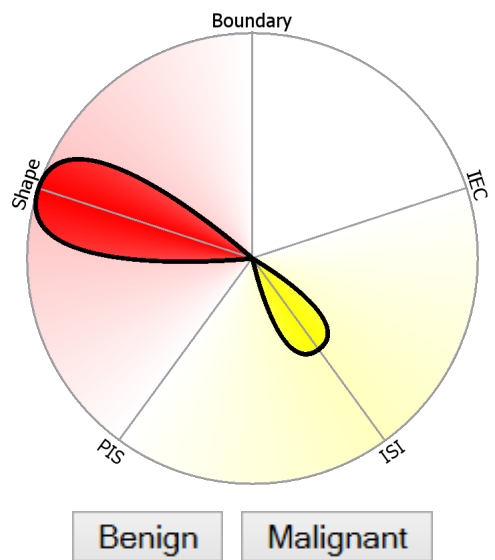


Figure B.12: Speed Test 12.

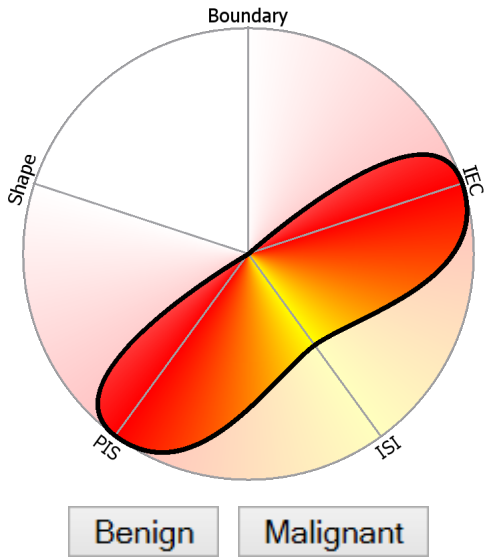


Figure B.13: Speed Test 13.

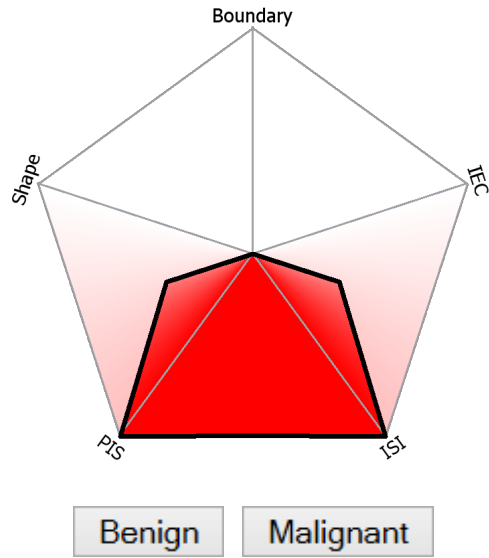


Figure B.14: Speed Test 14.

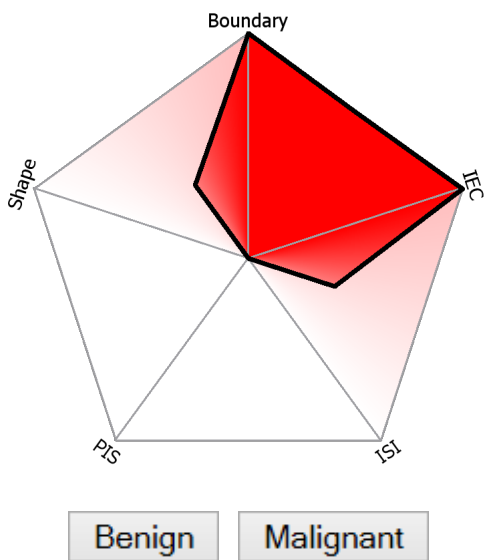


Figure B.15: Speed Test 15.

Feature	Points
Shape	1
Boundary	1
POE	0
ISI	1
PIS	0

Figure B.16: Speed Test 16.

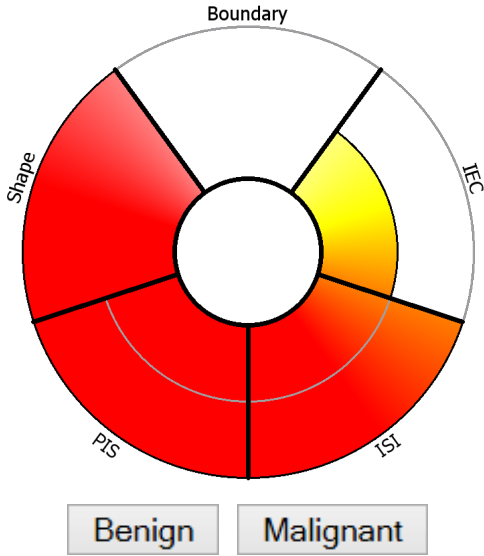


Figure B.17: Speed Test 17.

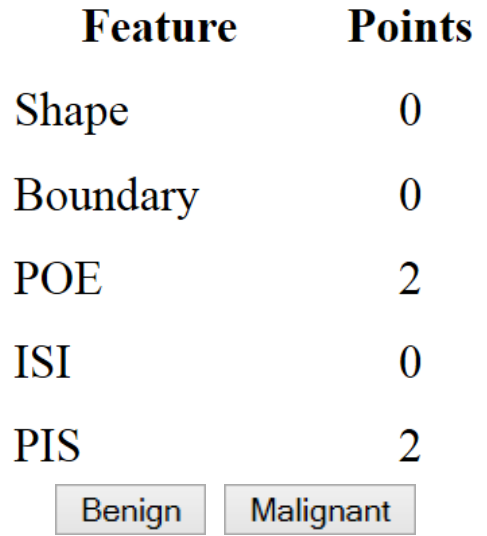


Figure B.18: Speed Test 18.

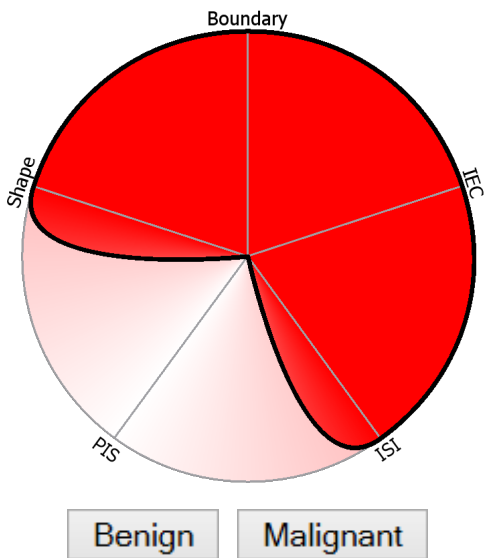


Figure B.19: Speed Test 19.

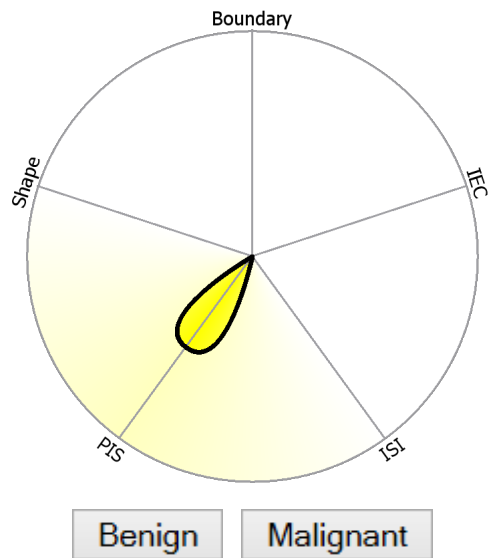


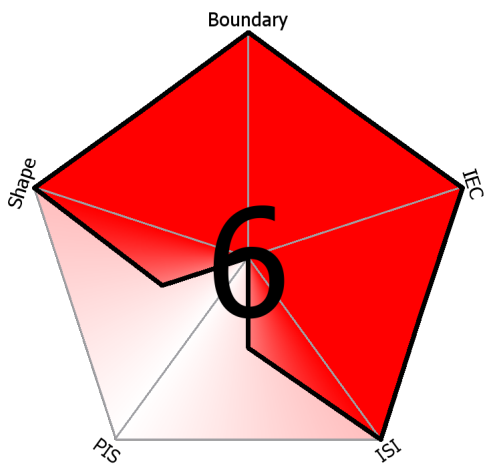
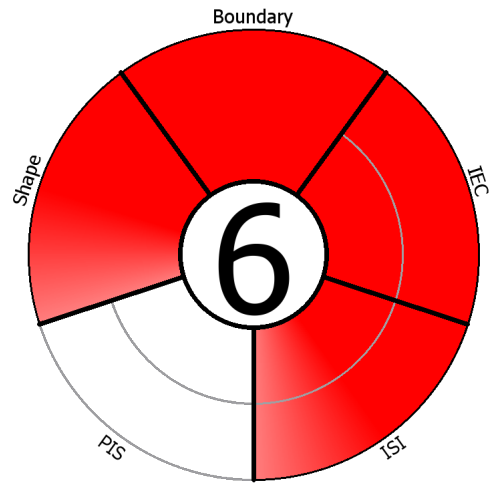
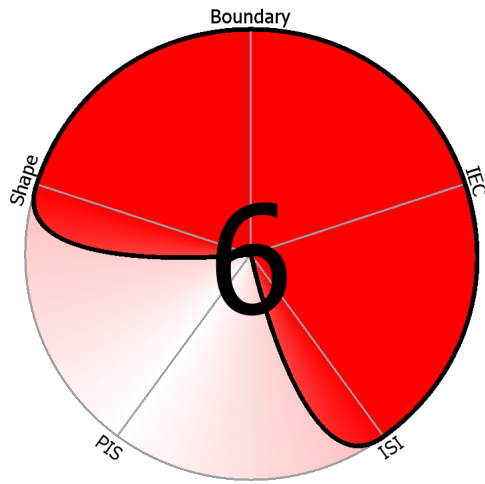
Figure B.20: Speed Test 20.

B.4 Style Test

You finished the first part!

We are now showing you some (randomly generated) data visualized with a linear, a cubic MAP, a sunburst MAP and a table. Please, click on the image that appeals to you the most.

We are not measuring time now, so take your time!



Feature	Points
Shape	1
Boundary	1
POE	2
ISI	2
PIS	0

Figure B.21: Style Test 01.

Feature	Points
Shape	0
Boundary	0
POE	2
ISI	0
PIS	0

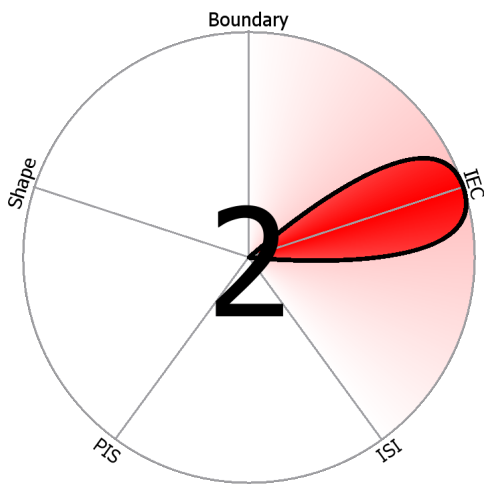
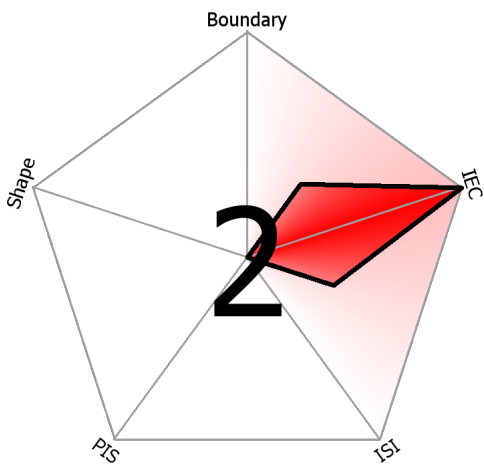
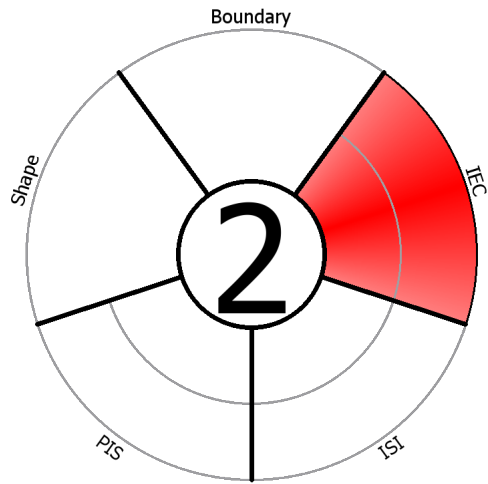


Figure B.22: Style Test 02.

Feature	Points
Shape	0
Boundary	0
POE	1
ISI	2
PIS	2

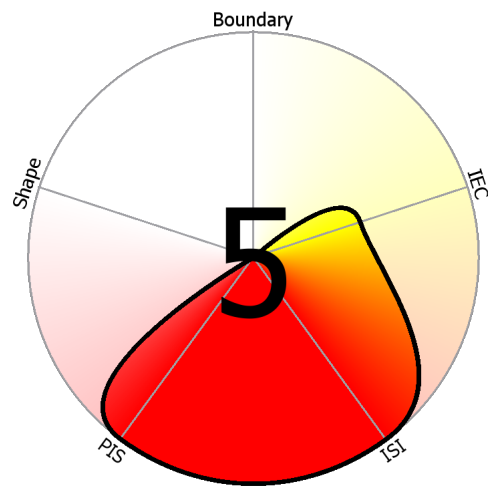
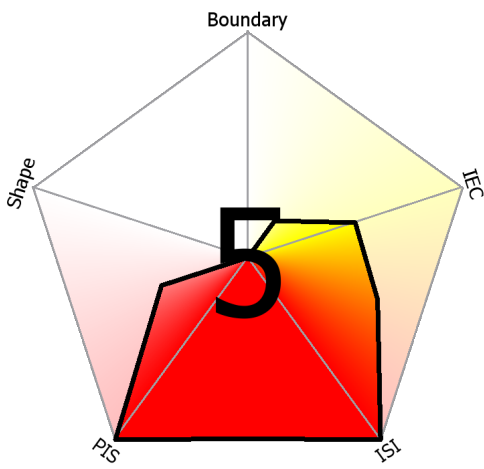
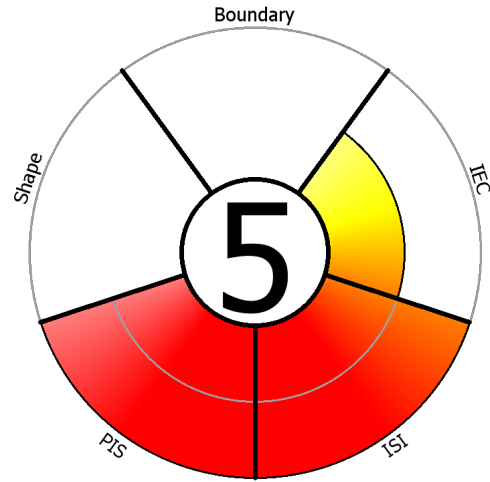
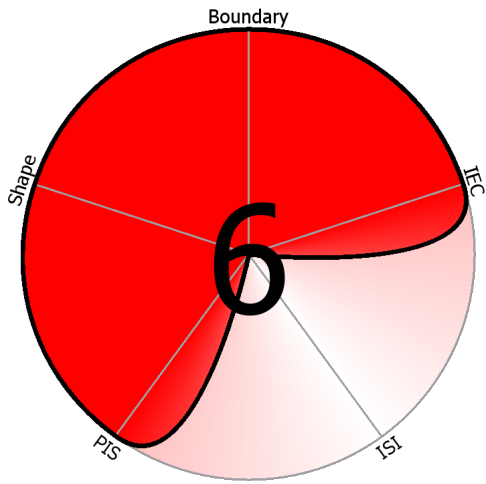


Figure B.23: Style Test 03.



Feature	Points
Shape	1
Boundary	1
POE	2
ISI	0
PIS	2

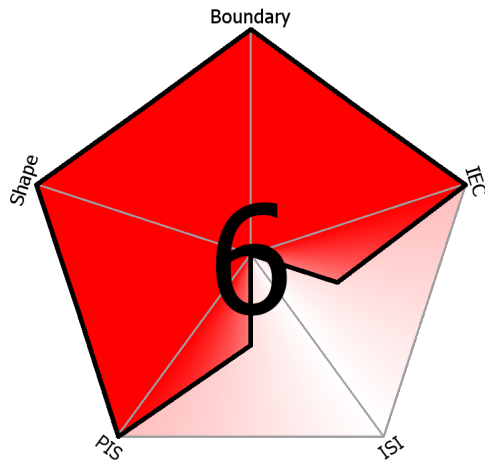
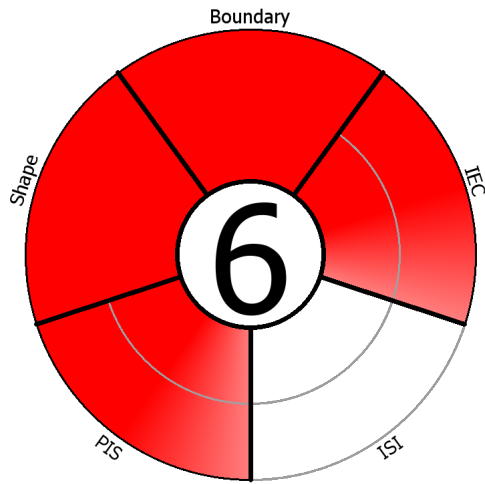
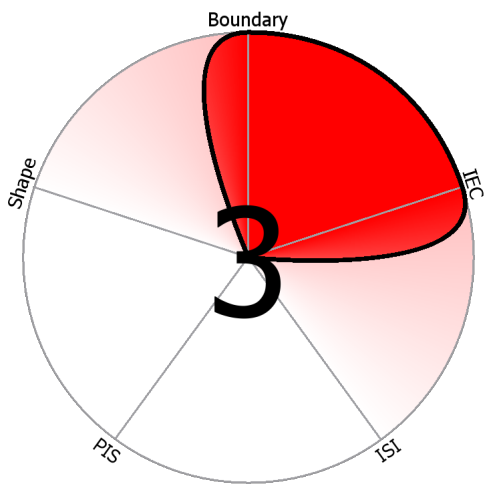
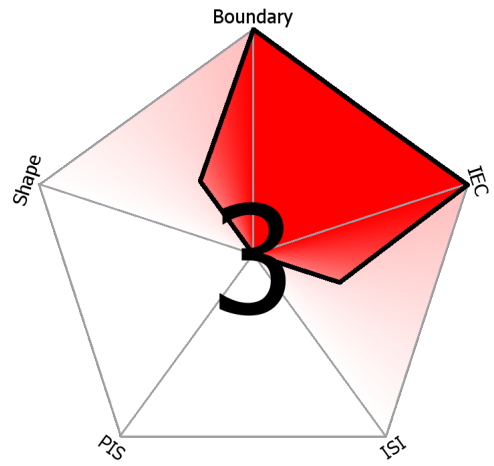
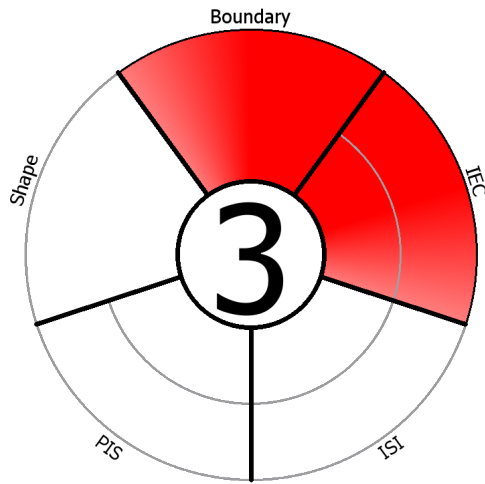
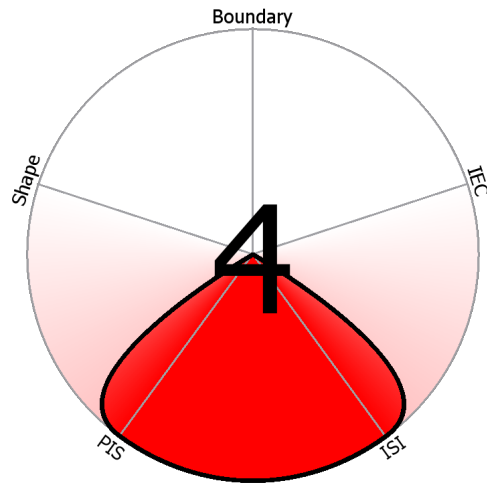
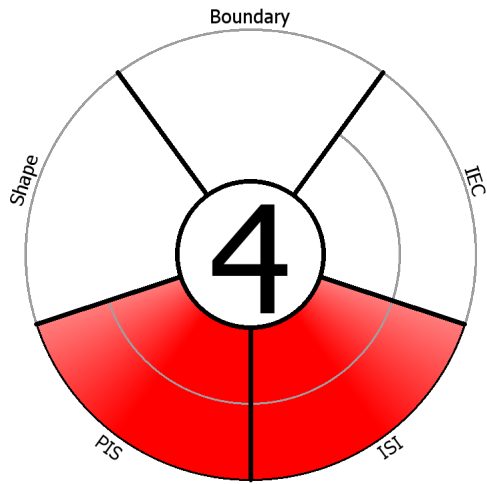


Figure B.24: Style Test 04.



Feature	Points
Shape	0
Boundary	1
POE	2
ISI	0
PIS	0

Figure B.25: Style Test 05.



Feature	Points
Shape	0
Boundary	0
POE	0
ISI	2
PIS	2

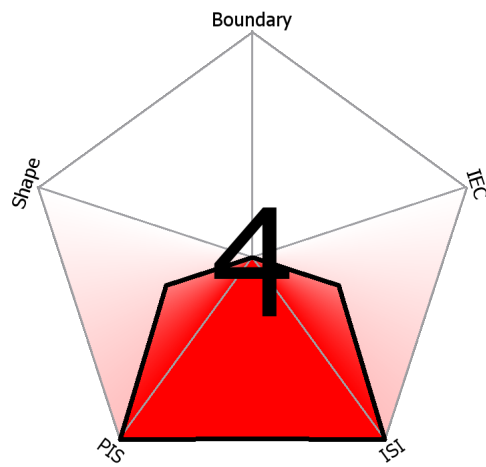
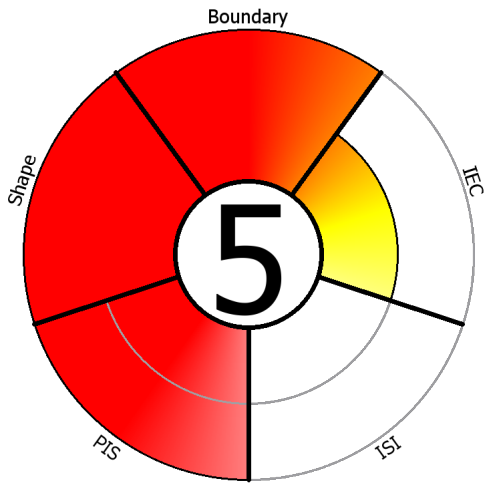


Figure B.26: Style Test 06.



Feature	Points
Shape	1
Boundary	1
POE	1
ISI	0
PIS	2

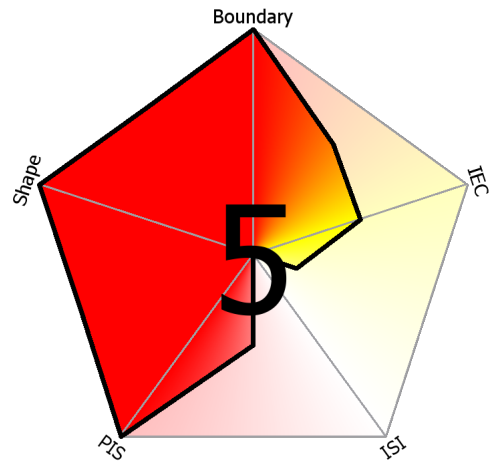
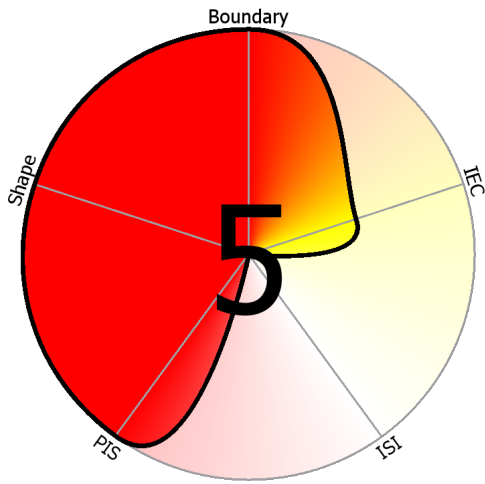
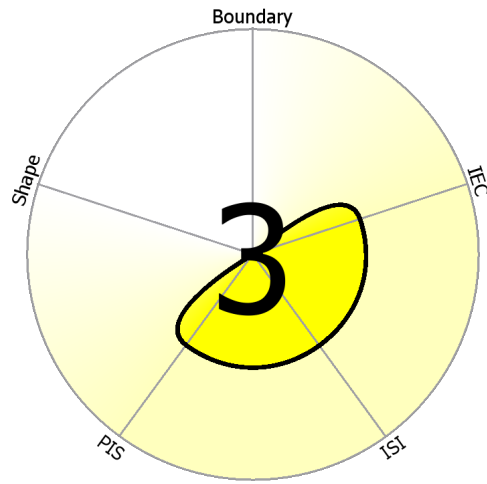
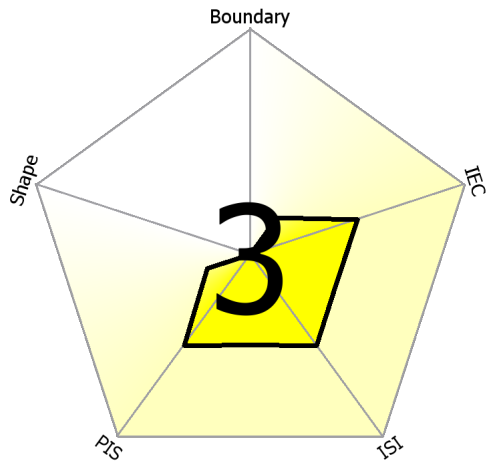


Figure B.27: Style Test 07.



Feature	Points
Shape	0
Boundary	0
POE	1
ISI	1
PIS	1

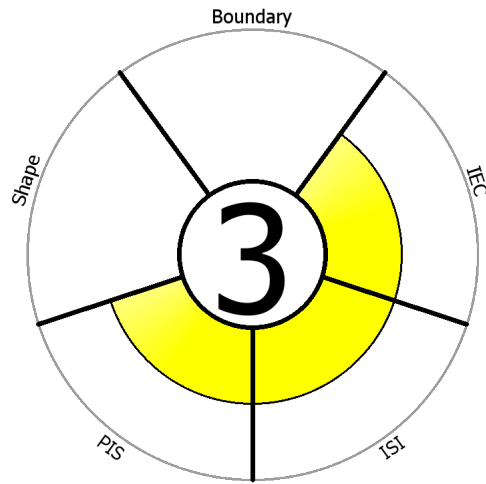


Figure B.28: Style Test 08.

B.5 Questions

You finished the second part!

We will now ask you some questions. Please, answer the questions by pressing the provided buttons.

B.5.1 Question 01

The visual representation of the Göttinger score is ...

- Useful
- Not Useful

B.5.2 Question 02

The overall score of the Göttinger score on its own would be ...

- Sufficient
- Insufficient

B.5.3 Question 03

The details in the visualizations presented are ...

- Intuitive
- Not Intuitive

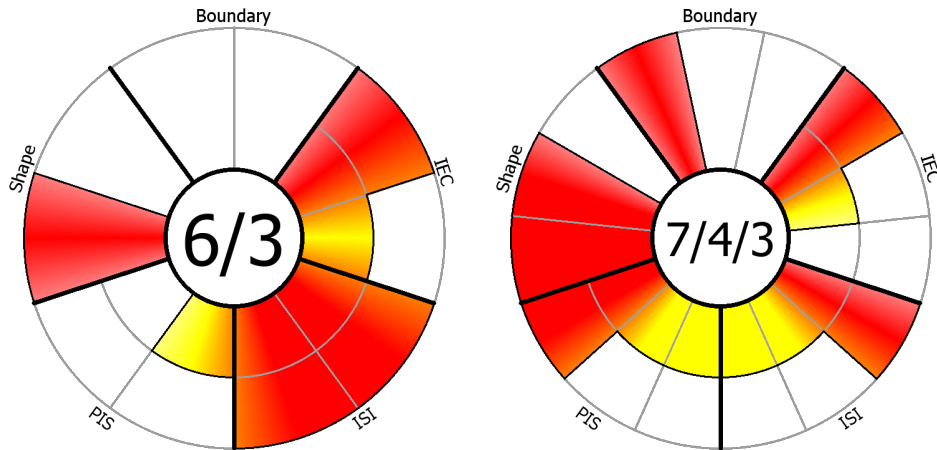
B.5.4 Question 04

For breast cancer diagnosis I would prefer to use a ...

- Visual Representation
- Tabular Representation

B.5.5 Question 05

We are now showing you a sunburst MAP for comparing more than one data set.

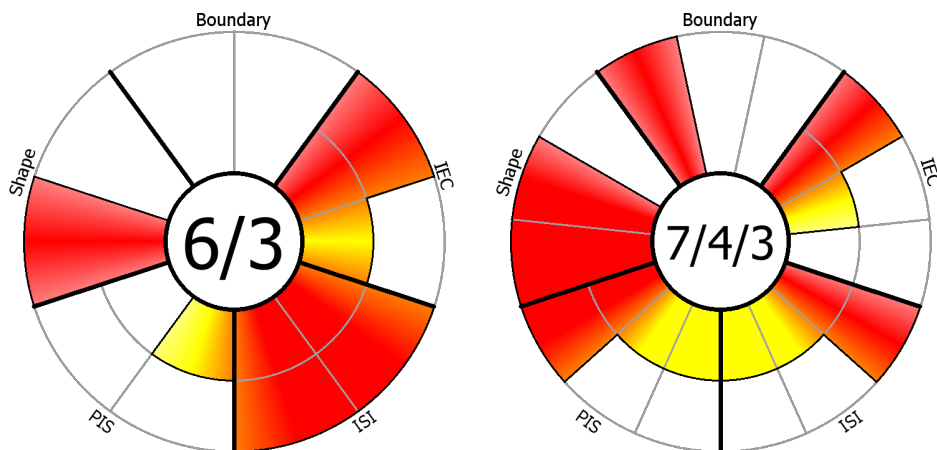


Such a visual comparison of multiple data sets is ...

- Intuitive
- Difficult to understand

B.5.6 Question 06

We are now showing you the sunburst MAP for comparing more than one data set.



Such a visual comparison of multiple data sets is ...

- Useful for breast cancer diagnosis comparison
- Unnecessary

B.5.7 Finish

You are almost done!

If you have some final comments, ideas or anything else you would like to tell us, please use the text box provided here:

Bibliography

- [1] Insight Segmentation and Registration Toolkit. Available from <http://www.itk.org/>. Last accessed: 2015-04-18.
- [2] Medical Imaging Toolkit. Available from <http://mitk.org/>. Last accessed: 2015-04-18.
- [3] National Comprehensive Cancer Network. Available from <http://www.nccn.org/>. Last accessed: 2015-04-18.
- [4] Visualization Toolkit. Available from <http://www.vtk.org/>. Last accessed: 2015-04-18.
- [5] S. C. Agner, S. Soman, E. Libfeld, M. McDonald, K. Thomas, S. Englander, M. A. Rosen, D. Chin, J. Noshier, and A. Madabhushi. Textural Kinetics: A Novel Dynamic Contrast-Enhanced (DCE)MRI Feature for Breast Lesion Classification. *Journal of Digital Imaging*, 24(3):446–463, 2011.
- [6] P. A. T. Baltzer, D. M. Renz, P. E. Kullnig, M. Gajda, O. Camara, and W. A. Kaiser. Application of Computer-aided Diagnosis (CAD) in MR-Mammography (MRM). *Academic Radiology*, 16(4):435–442, 2009.
- [7] L. Bax, N. Ikeda, N. Fukui, Y. Yaju, H. Tsuruta, and K. G. Moons. More than Numbers: The Power of Graphs in Meta-Analysis. *American Journal of Epidemiology*, 169(2):249–255, 2009.
- [8] A. Bhalerao and R. Wilson. A Fourier Approach to 3D Local Feature Estimation from Volume Data. In *BMVC*, pages 1–10, 2001.
- [9] J. Bigün. Optimal Orientation Detection of Linear Symmetry. In *Proceedings of the IEEE First International Conference on Computer Vision, (ICCV'87, London)*, pages 433–438. IEEE, 1987.
- [10] S. Bruckner and M. E. Gröller. Instant Volume Visualization Using Maximum Intensity Difference Accumulation. In *Computer Graphics Forum*, volume 28, pages 775–782. Wiley Online Library, 2009.

- [11] S. K. Card, J. D. Mackinlay, and B. Shneiderman. *Readings in Information Visualization - Using Vision to Think*. Morgan Kaufmann, 1999.
- [12] W. Y. Chen. *Breast Cancer Therapy*. Mosby Elsevier, 2007.
- [13] J. W. Cooley and J. W. Tukey. An Algorithm for the Machine Calculation of Complex Fourier Series. *Mathematics of Computation*, 19(90):297–301, 1965.
- [14] E. Coto, S. Grimm, S. Bruckner, M. E. Gröller, A. Kanitsar, and O. Rodriguez. MammoExplorer: An Advanced CAD Application for Breast DCE-MRI. In G. Greiner, J. Hornegger, H. Niemann, and M. Stamminger, editors, *Proceedings of Vision, Modelling, and Visualization 2005*, pages 91–98, nov 2005.
- [15] B. L. Daniel and D. M. Ikeda. *Breast Imaging: The Requisites*, chapter Magnetic Resonance Imaging of Breast Cancer and MRI-Guided Breast Biopsy. Elsevier Health Sciences, 2004.
- [16] H. Degani, V. Gusic, D. Weinstein, S. Fields, and S. Strano. Mapping Pathophysiological Features of Breast Tumors by MRI at High Spatial Resolution. *Nature Medicine*, 3(7):780–782, 1997.
- [17] H. Digabel and C. Lantuéjoul. Iterative Algorithms. In *Proc. 2nd European Symp. Quantitative Analysis of Microstructures in Material Science, Biology and Medicine*, volume 19, page 8. Stuttgart, West Germany: Riederer Verlag, 1978.
- [18] C. J. D’Orsi, E. A. Sickles, E. B. Mendelson, E. A. Morris, et al. *ACR BI-RADS[®] Atlas, Breast Imaging Reporting and Data System*. Reston, VA, 2013.
- [19] R. A. Drebin, L. C. Carpenter, and P. Hanrahan. Volume Rendering. *ACM Siggraph Computer Graphics*, 22(4):65–74, 1988.
- [20] P. Duhamel and M. Vetterli. Fast Fourier Transforms: A Tutorial Review and a State of the Art. *Signal Processing*, 19(4):259–299, 1990.
- [21] J. Ferlay, I. Soerjomataram, M. Ervik, R. Dikshit, S. Eser, C. Mathers, M. Rebelo, D. Parkin, D. Forman, and F. Bray. GLOBOCAN 2012 v1.0, Cancer Incidence and Mortality Worldwide: IARC CancerBase No. 11. Lyon, France: International Agency for Research on Cancer. Available from http://globocan.iarc.fr/Pages/fact_sheets_cancer.aspx, 2013. Last accessed: 2015-02-02.
- [22] U. Fischer and F. Baum. *Moderne Mammadiagnostik*. ABW Wissenschaftsverlag, 2010.
- [23] U. Fischer, L. Kopka, and E. Grabbe. Breast Carcinoma: Effect of Preoperative Contrast-Enhanced MR Imaging on the Therapeutic Approach. *Radiology*, 213(3):881–888, 1999.

- [24] R. Fitzpatrick. Newtonian Dynamics. Available from <http://farside.ph.utexas.edu/teaching/336k/Newton.pdf>, 2010. Last accessed: 2015-09-02.
- [25] G. Frieder, D. Gordon, and R. A. Reynolds. Back-to-Front Display of Voxel Based Objects. *IEEE Computer Graphics and Applications*, 5(1):52–60, 1985.
- [26] M. Frigo and S. G. Johnson. The Design and Implementation of FFTW3. *Proceedings of the IEEE*, 93(2):216–231, 2005. Special issue on “Program Generation, Optimization, and Platform Adaptation”.
- [27] C. Frouge and R. di Paola. Correlation Between Contrast Enhancement in Dynamic Magnetic Resonance Imaging of the Breast and Tumor Angiogenesis. *Investigative Radiology*, 29(12):1043–1049, 1994.
- [28] H. Fuchs, M. Levoy, and S. M. Pizer. Interactive Visualization of 3D Medical Data. *IEEE Computer*, 22(8):46–51, 1989.
- [29] E. Furman-Haran, D. Grobgeld, F. Kelcz, and H. Degani. Critical Role of Spatial Resolution in Dynamic Contrast-Enhanced Breast MRI. *Journal of Magnetic Resonance Imaging*, 13(6):862–867, 2001.
- [30] Y. Gal, A. Mehnert, A. P. Bradley, D. Kennedy, and S. Crozier. Feature and Classifier Selection for Automatic Classification of Lesions in Dynamic Contrast-Enhanced MRI of the Breast. In *Digital Image Computing: Techniques and Applications*, pages 132–139, 2009.
- [31] S. Glaßer, S. Schäfer, S. Oeltze, U. Preim, K. D. Tönnies, and B. Preim. A Visual Analytics Approach to Diagnosis of Breast DCE-MRI Data. *Computers & Graphics*, 34(5):602 – 611, 2010. CAD/GRAPHICS 2009 Extended papers from the 2009 Sketch-Based Interfaces and Modeling Conference Vision, Modeling & Visualization.
- [32] S. Gruber. *Gynäkologie und Geburtshilfe*. Elsevier Urban & Fischer, 2009.
- [33] H. Hauser, L. Mroz, G. I. Bisch, and M. E. Gröller. Two-Level Volume Rendering. *IEEE Transactions on Visualization and Computer Graphics*, 7(3):242–252, 2001.
- [34] E. A. M. Hauth, H. Jaeger, S. Maderwald, C. Stockamp, A. Mühler, R. Kimmig, and M. Forsting. Evaluation of Quantitative Parametric Analysis for Characterization of Breast Lesions in Contrast-Enhanced MR Mammography. *European Radiology*, 16(12):2834–2841, 2006.
- [35] S. H. Heywang-Kobrunner, I. Schreer, and D. D. Dershaw. Diagnostic Breast Imaging. *Acta Obstetrica et Gynecologica Scandinavica*, 77(1):134, 2001.
- [36] D. M. Ikeda. *Breast Imaging: The Requisites*. Elsevier Health Sciences, 2004.
- [37] B. Jähne. *Digital Image Processing*, volume 5. Springer, 2002.

- [38] A. Karahaliou, K. Vassiou, N. S. Arikidis, S. Skiadopoulos, T. Kanavou, and L. Costaridou. Assessing Heterogeneity of Lesion Enhancement Kinetics in Dynamic Contrast-Enhanced MRI for Breast Cancer Diagnosis. *British Journal of Radiology*, 83(988):296–309, 2010.
- [39] F. Kelcz, G. E. Santyr, G. O. Cron, and S. J. Mongin. Application of a Quantitative Model to Differentiate Benign from Malignant Breast Lesions Detected by Dynamic, Gadolinium-Enhanced MRI. *Journal of Magnetic Resonance Imaging*, 6(5):743–752, 1996.
- [40] J. Krüger and R. Westermann. Acceleration Techniques for GPU-Based Volume Rendering. In *Proceedings of the 14th IEEE Visualization 2003 (VIS'03)*, page 38. IEEE Computer Society, 2003.
- [41] M. Levoy. Display of Surfaces from Volume Data. *IEEE Computer Graphics and Applications*, 8(3):29–37, 1988.
- [42] M. Levoy. Design for a Real-Time High-Quality Volume Rendering Workstation. In *Volume Visualization and Graphics*, pages 85–92, 1989.
- [43] W. E. Lorensen and H. E. Cline. Marching Cubes: A High Resolution 3D Surface Construction Algorithm. *ACM Siggraph Computer Graphics*, 21(4):163–169, 1987.
- [44] N. Max. Optical Models for Direct Volume Rendering. *Visualization and Computer Graphics, IEEE Transactions on*, 1(2):99–108, 1995.
- [45] D. Mayer, T. Vomweg, H. Faber, O. Weinheimer, M. Mattiuzzi, M. Buscema, and C. Düber. Fully Automatic Breast Cancer Diagnosis in Contrast Enhanced MRI. *International Journal Of Computer Assisted Radiology And Surgery*, 1:325–327, 2006.
- [46] F. Montemurro, L. Martincich, I. Sarotto, I. Bertotto, R. Ponzzone, L. Cellini, S. Redana, P. Sismondi, M. Aglietta, and D. Regge. Relationship Between DCE-MRI Morphological and Functional Features and Histopathological Characteristics of Breast Cancer. *European Radiology*, 17(6):1490–1497, 2007.
- [47] P. H. Morgan, L. P. Mercer, and N. W. Flodin. General Model for Nutritional Responses of Higher Organisms. *Proceedings of the National Academy of Sciences*, 72:4327–4331, 1975.
- [48] NEMA. Digital Imaging and Communications in Medicine (DICOM) Standard. NEMA PS3 / ISO 12052, National Electrical Manufacturers Association, Rosslyn, VA, USA, 2014.
- [49] K. Nie, J.-H. Chen, H. J. Yu, Y. Chu, O. Nalcioglu, and M.-Y. Su. Quantitative Analysis of Lesion Morphology and Texture Features for Diagnostic Prediction in Breast MRI. *Academic Radiology*, 15(12):1513–1525, 2008.

- [50] T. Okafuji, H. Yabuuchi, H. Soeda, Y. Matsuo, T. Kamitani, S. Sakai, M. Hatakenaka, S. Kuroki, E. Tokunaga, H. Yamamoto, and H. Honda. Circumscribed Mass Lesions on Mammography: Dynamic Contrast-Enhanced MR Imaging to Differentiate Malignancy and Benignancy. *Magnetic Resonance in Medical Sciences*, 7(4):195–204, 2008.
- [51] B. T. Phong. Illumination for Computer Generated Pictures. *Communications of the ACM*, 18(6):311–317, 1975.
- [52] B. Preim and C. Botha. *Visual Computing for Medicine: Theory, Algorithms and Applications*. Morgan Kaufmann, 2014.
- [53] U. Preim, S. Glaßer, B. Preim, F. Fischbach, and J. Ricke. Computer-Aided Diagnosis in Breast DCE-MRI-Quantification of the Heterogeneity of Breast Lesions. *European Journal of Radiology*, 81(7):1532–1538, 2012.
- [54] D. M. Renz, J. Böttcher, F. Diekmann, A. Poellinger, M. H. Maurer, A. Pfeil, F. Streitparth, F. Colletini, U. Bick, B. Hamm, et al. Detection and Classification of Contrast-Enhancing Masses by a Fully Automatic Computer-Assisted Diagnosis System for Breast MRI. *Journal of Magnetic Resonance Imaging*, 35(5):1077–1088, 2012.
- [55] F. Sardanelli, A. Iozzelli, A. Fausto, A. Carriero, and M. A. Kirchin. Gadobenate Dimeglumine-enhanced MR Imaging Breast Vascular Maps: Association between Invasive Cancer and Ipsilateral Increased Vascularity. *Radiology*, 235(3):791–797, 2005.
- [56] A. C. Schmitz, N. H. G. M. Peters, W. B. Veldhuis, A. M. F. Gallardo, P. J. van Diest, G. Stapper, R. van Hillegersberg, W. P. T. M. Mali, and M. A. A. J. van den Bosch. Contrast-Enhanced 3.0-T Breast MRI for Characterization of Breast Lesions: Increased Specificity by Using Vascular Maps. *European Radiology*, 18(2):355–364, 2008.
- [57] W. J. Schroeder, B. Lorensen, and K. Martin. *The Visualization Toolkit*, volume 3. Kitware, 2004.
- [58] B. Shneiderman. The Eyes Have It: A Task by Data Type Taxonomy for Information Visualizations. In *Visual Languages/Human-Centric Computing Languages and Environments*, pages 336–343, 1996.
- [59] E. Sickles, C. D’Orsi, L. Bassett, et al. *ACR BI-RADS[®] Atlas, Breast Imaging Reporting and Data System*, chapter ACR BI-RADS[®] Mammography. Reston, VA, 2013.
- [60] K. S. Sim, F. K. Chia, M. E. Nia, C. P. Tso, A. K. Chong, S. F. Abbas, and S. S. Chong. Breast Cancer Detection from MR Images Through an Auto-Probing Discrete Fourier Transform System. *Computers in Biology and Medicine*, 49:46–59, 2014.

- [61] W. Van Aalst, T. Twellmann, H. Buurman, F. A. Gerritsen, and B. M. T. H. Romeny. Computer-Aided Diagnosis in Breast MRI: Do Adjunct Features Derived from T2-Weighted Images Improve Classification of Breast Masses? In *Bildverarbeitung für die Medizin*, pages 11–15, 2008.
- [62] I. Viola, A. Kanitsar, and M. E. Gröller. Importance-Driven Volume Rendering. In *IEEE Visualization*, pages 139–146, 2004.
- [63] D. Weishaupt, J. M. Fröhlich, D. Nanz, V. Köchli, K. Prüssmann, and B. Marincek. *How does MRI Work?: An Introduction to the Physics and Function of Magnetic Resonance Imaging*. Lecture Notes in Mathematics. Springer, 2008.
- [64] L. Westover. Interactive Volume Rendering. In *Volume Visualization and Graphics*, pages 9–16, 1989.
- [65] J. I. Wiener, K. J. Schilling, C. Adami, and N. A. Obuchowski. Assessment of Suspected Breast Cancer by MRI: A Prospective Clinical Trial using a Combined Kinetic and Morphologic Analysis. *American Journal of Roentgenology*, 184(3):878–886, 2005.
- [66] T. C. Williams, W. B. DeMartini, S. C. Partridge, S. Peacock, and C. D. Lehman. Breast MR Imaging: Computer-Aided Evaluation Program for Discriminating Benign from Malignant Lesions. *Radiology*, 244(1):94–103, 2007.
- [67] R. G. Wilson, A. D. Calway, and E. R. S. Pearson. A Generalized Wavelet Transform for Fourier Analysis: The Multiresolution Fourier Transform and Its Application to Image and Audio Signal Analysis. *IEEE Transactions on Information Theory*, 38(2):674–690, 1992.
- [68] I. Wolf, M. Vetter, I. Wegner, T. Böttger, M. Nolden, M. Schöbinger, M. Hastenteufel, T. Kunert, and H.-P. Meinzer. The Medical Imaging Interaction Toolkit. *Medical Image Analysis*, 9(6):594–604, 2005.
- [69] T. S. Yoo, M. J. Ackerman, W. E. Lorensen, W. Schroeder, V. Chalana, S. Aylward, D. Metaxas, and R. Whitaker. Engineering and Algorithm Design for an Image Processing API: A Technical Report on ITK - The Insight Toolkit. *Studies in Health Technology and Informatics*, pages 586–592, 2002.